A multiscale framework for the chemomechanical characterization of ancient heterogeneous materials

by

Janille Maria Maragh

S.B., Massachusetts Institute of Technology (2013)
S.M., Massachusetts Institute of Technology (2016)

Submitted to the Department of Civil and Environmental Engineering
in partial fulfillment of the requirements for the degree of

Doctor of Philosophy

at the

MASSACHUSETTS INSTITUTE OF TECHNOLOGY

February 2021

© Massachusetts Institute of Technology 2021. All rights reserved.

Author .....
Department of Civil and Environmental Engineering
January 15, 2020

Certified by .....
Admir Masic
Assistant Professor
Thesis Supervisor

Accepted by .....
Colette L. Heald
Professor of Civil and Environmental Engineering
Chair, Graduate Program Committee

A multiscale framework for the chemomechanical characterization of ancient heterogeneous materials

by

Janille Maria Maragh

Submitted to the Department of Civil and Environmental Engineering
on January 15, 2020, in partial fulfillment of the
requirements for the degree of
Doctor of Philosophy

Abstract

Over the course of hundreds—or sometimes even thousands—of years, ancient building materials have survived environmental exposure, modifications, and restorations, often to an extreme degree. These processes, which have occurred from antiquity all the way to the present, have resulted in materials that are poorly understood both chemically and mechanically. This increases the difficulty of designing conservation, preservation, and restoration strategies to ensure that future generations have access to the same ancient marvels that are accessible today. This is further complicated by the inherent value of cultural heritage materials, which makes it challenging and impractical to obtain this information using large samples. In this work, a minimally invasive multiscale chemomechanical framework for the study and homogenization of heterogeneous composite materials of unknown composition is presented, with the ultimate goal being the chemomechanical characterization of ancient Roman mortar.

First, advanced chemical characterization methods are used with computational techniques to better understand the phases present in a sample, and the application of these techniques to the study of ancient Roman mortar is presented. It is then demonstrated how the techniques developed for this study may be used for other applications, for example in the determination of ancient production technologies and in the understanding of the underlying mechanisms responsible for the durability and time resilience of ancient materials. In a chemical characterization study of a fragment of the Temple Scroll, the longest and most visually striking of the Dead Sea Scrolls, evaporitic sulfate salts that point to a unique production process are identified.

The second half of this thesis demonstrates how chemistry is interfaced with mechanics in the chemomechanical homogenization framework. Instead of directly using ancient Roman concrete, which is of immense cultural value, the homogenization framework is tested on a series of modern mortars produced using ordinary Portland cement, which bear numerous similarities to ancient Roman mortars but are more readily accessible and more easily produced. First, scanning electron microscopy energy dispersive X-ray spectroscopy (SEM-EDS) is used with data clustering algo-

rithms to identify the distribution of phases in each sample. Next, microindentation is used to assign mechanical properties to each of the chemically distinct phases identified, allowing for the generation of large-area high-resolution maps of mechanical properties. In the final stage of the framework, computational homogenization is performed: the chemomechanical maps are converted to finite element models, which are subjected to uniaxial compression and pure shear simulations to obtain estimates of the effective elastic properties of the samples, which are validated using laboratory compression testing data. Finally, the framework is applied to an ancient mortar sample using phase properties from the literature to estimate its effective elastic properties.

Thesis Supervisor: Admir Masic
Title: Assistant Professor

Acknowledgments

To my friends, family, and mentors, thank you for shaping my experience at MIT. Thank you to my PhD advisor, Professor Admir Masic, for giving me the opportunity to enter the world of cultural heritage and for teaching me to be a curious and independent researcher. Thank you to my committee members, Professor Oral Büyüköztürk, Professor Tal Cohen, Professor Elsa Olivetti, and Professor John Williams for showing me how to tell the story of my research, for shaping the direction of my thesis, for making committee meetings something to look forward to, and for pushing me to enter new realms of research along the way. Thank you to Dr. Steven Palkovic for providing technical and philosophical mentorship, for laying the groundwork for the modeling portion of my thesis, and for being a great co-teaching assistant.

Thank you to my undergraduate advisors, Professor Peter Fisher, Dr. Stephen Steadman, and Professor Ian Hunter, for being supportive and for guiding me academically. Thank you to my first UROP advisor, Professor Samuel Allen, for introducing me to the exciting world of materials science research. Thank you to my second UROP advisor and my Master's degree advisor, Professor John Leonard, for teaching me how to do a deep dive into solving challenging research problems and for being supportive throughout the years. Thank you to my first labmates in and adjacent to the MIT Marine Robotics Group, Liam Paull, Alon Yaari, Thomas Sayre-Kaynia, Michael Benjamin, David Rosen, Ted Steiner, Dehann Fourie, Sudeep Pillai, Nicholas Rypkema, Pedro Vaz Teixeira, and Ross Finman, for being role models, mentors, and friends. To the teachers at Campion College, thank you for building the foundation for the rest of my academic career.

Thank you to Dr. Gordana Herning, Professor Caitlin Mueller, and Professor John Ochesendorf for being excellent mentors in research, in the classroom, and in the field of civil engineering. Thank you to our collaborators in Italy, Gianfranco Quaranta, Roberto Scalesse, Marco Nicola, Guy Devreux, Gilberto Quarneti, the Nicola family, the team at La Venaria Reale, the team at the Privernum archaeological area, and countless others who participated in the ONE-MA3 summer fieldwork experience,

for providing the context for this work and for the practical experience in ancient technologies and conservation. Thank you to my peers in cultural heritage research, particularly Teresa Duncan and Marc Vermeulen, for our research discussions and your work in improving the accessibility of the field. Thank you to my direct collaborators, James Weaver, Roman Schuetz, Ira Rabin, Thibaut Divoux, Sam Raymond, Asheesh Shukla, and Kunal Kupwade-Patil for providing the necessary complementary expertise to this work over the years. Thank you to my UROP, Eric Wong, for your commitment to the Pompeii project. Thank you to Hao Kang for your logistical efforts in helping me to finish my thesis remotely.

Thank you to my labmates Chad Loh, Linda Seymour, and Rachel Kim, for always being willing to talk about research, for sitting through countless practice talks, for providing mentorship, for being excellent travel buddies, and for being kind and supportive friends. Chad, thank you for being the best partner for font discussions, spin class, and dim sum, and for all the practical lessons in graphic design. Linda, thank you for being the best Roman concrete expert, summer roommate, and co-TA. Rachel, thank you for being a wonderful concrete coach and a kind and cheerful friend.

Thank you to Lillie Paquette, Dr. Daniel Debowy, Dr. Karen Singleton, and Dr. Sejal Patel for being honest, kind, and supportive over the years and for always being there to help me navigate difficult situations. To everyone in the CEE academic programs office, Kiley Clapper, Sarah Smith, Max Martelli, Kathy Briana, Bori Stoyanova, Marygrace Aboudou, Allison Dougherty, and Taylor Deleon, thank you for consistently providing logistical support, fun distractions, and unrelenting kindness since my first day in the department. To the MechE graduate administrators, Leslie Regan, Una Sheehan, and Joan Kravit, thank you for our kindness and support, both during and long after the time I was in department. To our lab administrator Jeanette Marchocki, thank you for supporting us grad students, for the wonderful coffee conversations, and for always making sure we have exactly what we need.

It would not have been possible to successfully make it through graduate school without the support of my friends and family. Thank you to my peers in the de-

partment, particularly Murat Uzun, James Long, Cecilia Viggiano, Steven Palkovic, Isabelle Su, Elise Ledieu, Benjamin Cameron, Tiziana Smith Mercado, Angi Acocella, and Justin Montgomery, for all the honest discussions about grad school and the research-independent camaraderie. To my first friends in the MechE department all those years ago, Tommaso Taddei, Andrew Houck, Mustafa Mohamad, Connor Mulcahy, Robert Katzschmann (and the rest of the clan, Grace, Colin, and Lena), Colin Bonatti, Claudio Hail, Victor Lesniewski, Katie Taylor, Phillip Daniel, and João Ramos, thank you for literally every single fun memory from the first two years of grad school and many more since then. To my day-one-of-grad-school friends Danielle Pace, Marek Hempel, Twan Koolen, Eva Golos, Colm O'Rourke, and Alin Tomescu, thank you for the outings, picnics, and chats—especially those that made 2020 bearable. To Kit Kennedy, the Kennedy family, and everyone else at the ranch, thank you for the providing the much-appreciated escape from grad school. Narges Sayre-Kaynia, Thomas Sayre-Kaynia, and Levi Lentz, thank you for somehow being both protective friends and encouraging mentors throughout this experience.

To my fellow officers of the Graduate Student Council, Michael McClellan, Kyle Kotowick, and Eva Golos, the rest of the GSC Executive Committee, our administrators Betsy Granese, Lauren McLean, and Imani Ivery, and the German American Conference team, particularly Philipp Simons, Angela Wittmann, Tim Menke, Kathi Höbel, Johannes von Billerbeck, Jens Marchewski, Eesha Khare, Peter Marquardt, Jonas Lehmann, and Chris Kranzinger, thank you for being kind, loyal friends and for being equally committed to academia and world outside of it.

Thank you to Conner 3, particularly Lindsay Stone, Liz Morant, Ester Lomeli, and Katie Inman, to my roommates Bakari Hassan, Thao Phan, Simon Batzner, and Greg Puzsko, to Alex Mijailovic, Jan Tiepelt, Benjamin Miller, Andi Leber, Shaiyan Keshvari, Neta Batscha, and Noa Ghersin for the supportive chats and countless wonderful memories. To Raspberry Simpson, Tia Vice, Ashley Hartwell, Candace Ross, Corshai Williams, Zanele Munyikwa, and Kenyatta McLean, thank you for always being there for deep discussions, support, and celebrations. Thank you to Casandra Ceri, Steph Cooke, Krista Westenfeld, Sarah Rogge, Caroline Wiklund,

and Haley Williams for making Monday nights something to look forward to. Thank you to Xiaoyu Wu, Daniel Duane, Sarah Walker, Sarah Fay, Quantum Wei, Hugo Uvegi, PJ Santos, Jackie Kim, Bitzy Flamholz, and everyone else in the potluck group for making Sunday nights the best start to the week. Rachel Fernandes and Alex Brown, thank you for consistently bringing the warmth of home to Boston. To Mary Anderson and Sebastian Castro, thank you for all the unforgettable Saturdays that started with 10AM brunch. Thank you to Kristen Railey for being a present and supportive friend and an exceptional role model. Thank you to Jean Sack for the heart-to-hearts over monthly pedicures. Thank you to Uyanga Tsedev and Sara Nagelberg for always being on my team, for being there to get me through the most challenging parts of the past several years, and for the countless days and nights baking, doing crafts, and planning galas. Thank you to Pavel Shcherban for making the choice to adopt this role over the years. Thank you to CJ Enloe for always being there for weeknight dinners, weekend adventures, and on days where I needed a friend, no where matter where in the world you are.

Finally, I am incredibly grateful for my amazing family. To my grandparents, aunts, uncles, and cousins, thank you for your unwavering support. Thank you to Shakira Banhan, who has remained the most steady friend for decades. To my father, Dr. Paul Maragh, thank you for instilling in us a love for science, for giving us our excitement for cooking, and for always being there to advise me on topics in chemistry and navigating grad school. To my mother, Margaret Maragh, thank you for being the perfect example of kindness, for always taking care of us no matter how old we get, and for always offering to book a flight to visit me during tough times, which always reminded me that I'm never on my own. To my sister, Alecia Maragh, thank you for taking care of me during stressful days in undergrad, for all those dinners in the student center over comedies before diving into the homework of the evening, and for cheering me on at every milestone. The last several years would not have been possible without you all.

Contents

List of Figures

List of Tables

Chapter 1

Introduction

1.1 Motivation

Cultural heritage researchers study ancient materials with the primary goals of preservation, conservation, and restoration. Although we may have access to records that describe how an ancient material or structure was made hundreds or sometimes even thousands of years ago, there are many processes that have occurred since the moment of their production that have resulted in materials that are poorly understood today. Environmental exposure and aging processes cause alterations in material chemistry and material structure that are difficult to fully realize without investigation. As an example, a known degradation pathway for ancient Roman concrete is the displacement of carbonate (CO_3^{2-}) ions in insoluble calcium carbonate with sulfate ions (SO_4^{2-}) from acid rain, resulting in the formation of soluble calcium sulfate and therefore material loss in the presence of water, but the extent of such degradation cannot be fully understood without the collection of spatially resolved chemical characterization data. Ancient materials have survived through the ages with histories of production and degradation that are for the most part unknown by present day researchers. Because of these unknowns, we do not really understand how they will behave under various chemical conditions and loading conditions. Knowing their chemical and mechanical properties would go a long way in developing strategies to protect these invaluable structures.

Chemical characterization of ancient materials helps us to better understand which phases are present in ancient composites, and the resulting data is useful in making decisions regarding how artifacts are cared for. Spatially resolved chemical data can help us to distinguish which phases originated from production versus which phases are a result of degradation processes, and by studying the phases along and near exposed surfaces, we can know how the material will react to cleaning substrates, protective substrates, and different environmental conditions. This can also inform decisions regarding interventions, for example, if it is necessary to add a sacrificial layer to protect the original material or alter the environmental conditions in order to slow down material degradation and loss.

Alterations in the chemical phases present and in the porosity of ancient materials via degradation or other aging processes directly affect their mechanical properties as well, and understanding these mechanical properties helps us to understand how ancient structures will behave under various loading conditions. In a study of the stability of three free-standing multi-drum columns in the Temple of Apollo of Pompeii (details of study in Appendix A), it was determined that they were indeed at risk of collapse. The material point method (MPM) was then used to determine the risk of damage by predicting the fracture behavior of the drums upon impact with both soft soil and solid ground. However, the possibility exists that the MPM simulation results may not be entirely accurate since assumed material properties were used in lieu of the true but unknown material properties.

Historically, it is known that two of the columns were carved from tuff, but they were produced over 2000 years ago. Since then, the columns have survived millennia of changing environmental conditions, interactions with researchers and tourists, and degradation processes that are difficult to quantify. These factors have led to the development of a material that is now of unknown composition and therefore possesses unknown material properties. This is the case for not only the columns of Pompeii, but for numerous ancient and historic materials that are currently poorly understood by researchers due to their complex histories.

Bulk mechanical testing techniques, such as compression testing or microdrilling

[3, 4], may be used to obtain the mechanical properties of ancient building materials, but such techniques are relatively invasive and not desirable when sampling materials of considerable cultural value. Computational techniques are advantageous in this case, since they tend to require relatively small samples, provided they are large enough to capture the heterogeneity at a representative scale, and can account for the sometimes highly irregular geometries present in ancient composites [5], such as ancient Roman concrete. Mechanical characterization helps cultural heritage researchers to understand how elements of ancient structures may deform or deflect under various loading conditions, such as fixed loads, forces from support structures, or live loads from tourist traffic. Numerical methods may also help us to understand how elements will perform—for example, through the prediction of fracture—in the event of catastrophic events, such as structural collapse.

The study of composite materials of unknown composition is not just important for reasons concerning the preservation, conservation, and restoration of ancient materials; materials of unknown composition that need to be characterized span fields far beyond cultural heritage. In fact, such materials exist wherever the constituents were not intentionally included by design. Manufactured materials may fall into this category if, for example, flaws are introduced during production. Features like porosity and warped phase geometries could cause the properties of a manufactured material to differ from what was intended. Similar to ancient materials, modern-age degraded materials, such as concrete structures that were produced 50 to 100 years ago, may also be poorly understood. Concrete, being a dynamically evolving system, consists of phases that are present in different amounts depending on production conditions, and the phases tend to evolve unpredictably with time through various processes, including the damaging alkali silica reaction.

Another broad group of materials that are also of unknown composition is biological materials, for which the chemistries and geometric arrangements of the constituent phases are typically only understood through characterization. As ancient materials have been optimized through generations of human experience, biological materials have been produced by nature using processes that have been optimized

through evolution. Materials that have been optimized though processes outside the scope of those possible in modern research and industry tend to be used as sources of inspiration in the design of new materials due to their favorable properties. The structure-function relationships of biological materials define these favorable properties, and both chemical and mechanical characterization are necessary to define them.

This thesis is therefore divided into two parts: the first focuses on spatially resolved chemical characterization, and the second focuses on interfacing chemistry with mechanics and performing computational mechanical characterization.

1.2 Thesis Overview

1.2.1 Research Objective

The objective of this research is to perform the chemomechanical characterization of complex composite materials using small and representative samples. In many fields, particularly in the study of ancient and other historic materials, it tends to be infeasible to use large samples of materials to understand how they will behave under various chemical conditions and loading states. This thesis explores the use of advanced chemical characterization techniques to understand the constituent phases present in such composites and proposes a way to interface the resulting chemical data with mechanics to estimate their effective elastic properties. Using the characterization and preservation of ancient Roman concrete as the driving motivation for the thesis, the following chapters describe a chemomechanical characterization framework that calls for samples that are only a few millimeters in width.

1.2.2 Research Approach

First, chemical characterization is conducted using spectroscopic methods that are able to resolve phases at high spatial resolution, namely confocal Raman microscopy and scanning electron microscopy energy dispersive X-ray spectroscopy (SEM-EDS).

The data obtained using the latter is then used with a set of computational techniques that were developed to better interpret the rich datasets and draw conclusions regarding the phases present in various samples. Finally, these datasets are converted to high resolution phase maps, which when combined with micron-scale mechanical properties, are then converted to high resolution maps of mechanical properties. These maps may then be used with a range of modeling techniques; in this thesis, it is shown that when they are converted to finite element models, they may be used to estimate the effective elastic properties of cementitious materials, as well as composite materials in general.

1.2.3 Thesis Organization

Chapter 1—Introduction: Motivation & Thesis Overview

Part I—Chemical Characterization: Spectroscopic Methods & Computational Tools

Chapter 2—Background: Chemical characterization of ancient and modern cementitious materials

Chapter 3—3D SEM-EDS and Raman chemical imaging of ancient Roman mortar

Scanning electron microscopy energy dispersive X-ray spectroscopy (SEM-EDS) and confocal Raman microscopy are used to determine the identities and spatial distributions of the phases present in ancient Roman mortar, both in polished cross-sections and on the fracture surface.

Chapter 4—Computational tools for the analysis of chemical characterization data

Techniques are presented for the correlation of 3D data collected using different characterization systems, and ternary diagrams are introduced as tools for the interpretation of large SEM-EDS datasets. A procedure is presented for the use of unsupervised learning with SEM-EDS datasets to generate phase maps that reflect the microstructural arrangement of constituent phases in composite materials.

Chapter 5—The Temple Scroll: Reconstructing an ancient manufacturing process

Co-authored with Dr. Roman Schuetz

A demonstration of how the techniques presented in Chapters 3 and 4 may be applied to another type of material, ancient parchment, is presented in this chapter. The results of a characterization study of the Dead Sea Scrolls are presented, and the results indicate the use of a previously unidentified parchment production method.

Part II—Interfacing chemical characterization data with mechanical modeling techniques

Chapter 6—Background: Mechanical modeling of composites and cementitious materials

Chapter 7—A chemomechanical framework for the computational homogenization of cementitious materials

The techniques presented in Chapters 3 & 4 are applied to a series of ordinary Portland cement mortars to generate phase maps, which are then used with finite element modeling to estimate their effective elastic properties. The results are validated using laboratory compression testing data. The framework is then applied to a sample of ancient Roman mortar to estimate its elastic properties.

Chapter 8—Summary of thesis contributions & pathways for future work

Appendix

Appendix A—Case study in cultural heritage: the freestanding multi-drum columns of Pompeii

A stability study is conducted for three free-standing columns from the Temple of Apollo in Pompeii using both numerical methods and scale model collapse experiments. The material point method is used to observe what would happen to the drums in the event of structural collapse.

Appendix B—K-means clustering of kidney stone SEM-EDS data

Part I

Chemical Characterization: Spectroscopic Methods & Computational Tools

Chapter 2

Background: Chemical characterization of ancient and modern cementitious materials

Throughout human history, the development of materials processing technologies, supported by the existence of biological and geological materials with favorable mechanical properties, has played a key role in the cultural evolution of our species. Bones have been cut and polished in the production of ancient cutting and grinding tools since at least the Upper Paleolithic [6], animal skins have been used for the documentation of historical texts, for example in the case of the Dead Sea Scrolls [7, 8], and volcanic ash has been incorporated to produce high strength cements [9], for example in the production of hydraulic mortar using ash obtained from the area around Mount Vesuvius [10]. The success of ancient empires may largely be attributed to the development of materials and building technologies and their empirical improvements [11]. The sophistication of these ancient building techniques is observable in the enduring remains of these ancient civilizations in the present day, which still exhibit durability despite millennia of seismic activity, environmental changes, and natural disasters [12, 13]. In addition to their cultural and historical significance, these materials also offer modern researchers technological lessons in terms of sustainability and durability. The long-term resistance of ancient Roman concrete to environmental

degradation over the course of millennia, for example, could provide design inspiration for the production of a new generation of more durable construction materials.

2.1 Production and properties of ancient Roman concrete

The use of ancient Roman cement in the production of mortar (mixture of cement paste and fine aggregate) and *opus cæmenticum* or Roman concrete (mixture of mortar with larger aggregate: *cæmenta*) [14] permitted the fabrication of some of antiquity's most massive architectural marvels. The use of lime in the production of cement was not original to the Roman Empire; the Greeks had previously produced cement in this manner with varying levels of success. However, the addition of *pozzolana* (high alkali volcanic ash, primarily consisting of amorphous aluminosilicates), native to the areas surrounding Mount Vesuvius in Campania, to this mixture resulted in a superior binding mortar [10, 15], which produced concretes with a greater compressive strength than concretes produced using pure lime cement. Replicas of architectural Roman mortar have been found to have a 180-day compressive strength of approximately 13 MPa [16], which is 75% of that of modern structural lightweight aggregate concrete [17], and at least four times greater than that of pure lime mortar [18].

Ancient Roman cement paste is a mixture of slaked lime and siliceous volcanic ash (*pozzolana*). In its production process, calcium carbonate (limestone) is calcined at 900°C to produce calcium oxide, which is then mixed with water to produce slaked lime. Amorphous or poorly-crystalline calcium and aluminate silicate hydrate gel phases are then produced in reaction layers surrounding the *pozzolana* fragments as they react with the slaked lime [19, 20, 21]; these gel phases significantly contribute to the durability of ancient Roman mortar and its resistance to environmental damage [21]. Furthermore, recent studies have shown that mineral cements may be continually precipitated over long periods of time in certain concretes, such as ancient Roman

seawater concrete [22]; comprehensive studies of these concretes are imperative in the understanding of cements that generate new cementitious phases over time, which may prove to be crucial in the design of new construction materials.

2.2 Ancient Roman concrete vs. modern ordinary Portland cement-based concrete

The production of the world's mostly widely used modern construction material, ordinary Portland cement (OPC), accounts for approximately 5% of the world's carbon emissions [23], and 90% of its embodied carbon is due to the large fuel requirement for its production, particularly the hot stage, which occurs at approximately 1450°C. The significantly lower temperatures required for the production of ancient Roman concrete equate to a lower fuel requirement: another reason to look to this material for inspiration in the design of more sustainably-produced construction materials. Ancient Roman concrete does, however, exhibit some significant drawbacks. Whereas cement paste made using OPC may cure in air in as little as 28 days to achieve a compressive strength close to its maximum [24], the volcanic ash and lime-based architectural Roman mortar has been shown to require a relatively long cure time of at least 180 days [25]. However, by partially replacing the constituents of modern concrete with components inspired by these ancient Roman concrete mixtures, an improved cement that balances durability and sustainability with an acceptable curing time could be developed. To set the stage for other researchers to carry out this process and to gain a better understating of the compositional complexity of this heterogeneous material, samples of ancient Roman concrete have been investigated through the use of complementary advanced materials characterization techniques, and the results of this investigation are reported in this chapter.

2.3 Chemical characterization of modern concrete

OPC consists of two major components: alite (Ca_3SiO_5, or C_3S in cement chemistry notation), primarily responsible for the 28-day "early" strength development of hydrated cement, and belite Ca_2SiO_4, or C_2S in cement chemistry notation), primarily responsible for the development of its "late" strength [19]. Confocal Raman microscopy (CRM) is one method that has been used for the analysis of these specific phases. It has been used in modern cement chemistry research to non-destructively study the microstructure and spatial distribution of calcium silicate hydrate (C-S-H) and other reactants formed in hydrating C_3S [26]. This technique can also supplement more labor-intensive and time consuming methods, such as ^{29}Si nuclear magnetic resonance (NMR) spectroscopy, in the characterization of C-S-H, calcium aluminate silicate hydrate (C-A-S-H) and sodium and aluminum substituted C-S-H (C-N-A-S-H) gel phases [27]. Raman microscopy has also been used in the study of degradation processes in OPC, through the spatial characterization of phases that cause a reduction in cement hardening in C_3S and C_2S pastes [28]. In addition to Raman-based techniques, scanning electron microscopy (SEM) based characterization approaches such as energy dispersive X-ray spectroscopy (EDS), which can be used for the identification and spatial mapping of elemental ratios, have been used in the characterization of hydrated OPC and volcanic ash mixtures and in the generation of CaO-SiO_2-Al_2O_3 ternary phase diagrams, which can be used to identify specific C-A-S-H phases [29, 30]. When the ternary ratios of particular oxides are plotted, either in the characterization of OPC or Roman concrete [9, 31], the proportion of particular gels and other phases may be determined, and specific components may be identified. When large area SEM-EDS maps are collected for a given sample, the vast amounts of data collected (often millions of spectra) can be used to compute these ternary ratios, which may then be visualized as a ternary frequency plot, on which chemically distinct components of a heterogeneous sample may be identified [32].

2.4 Confocal Raman microscopy and SEM-EDS in the study of modern and ancient Roman concrete

Whereas other characterization techniques introduce inconvenient challenges, such as the need for ultrathin section preparation in the case of transmission electron microscopy (TEM), the lack of spatial resolution of detected phases in bench-top X-ray diffraction, or the low contrast between different cement phases typically seen in SEM/BS-SEM imaging data [33, 34], Raman spectroscopy and SEM-EDS mapping are appealing choices due to their need for minimal sample preparation and their utility in spatially resolving phases and elements present in a sample with high compositional specificity.

The high-throughput nature of SEM-EDS means that one can quickly determine the ratios and spatial distributions of different elements, and for Raman spectroscopy, Raman active phases only need to be in focus in order to be detected. When both of these techniques are utilized in parallel, the result is a rich set of complementary data, but each approach is not without its limitations: SEM-EDS yields the distribution of elements everywhere on the surface of a sample measured, but it does not directly specify the phases present and requires that samples are dry and under vacuum during measurement. Raman spectroscopy, in contrast, is able to detect the phases present in samples that are hydrated and at atmospheric pressure, but only in cases where a Raman active species is present.

Raman spectroscopy and SEM-EDS have both been employed in the study of ancient concretes, for example in the characterization of ancient Roman seawater concrete, as tools in detecting precipitated phillipsite, Al-tobermorite, and gel-like C-A-S-H in relict lime clasts and in interfacial zones along the perimeter of certain aggregates, which are believed to contribute to the resilience of the concrete [12, 22]. SEM-EDS has also been used to study ancient pozzolanic cements containing strätlingite, a mineral that reinforces the cementitious matrix and grows as plates

that resist crack propagation [13], which have been detected in Roman mortar found in the Colosseum [35], the Theatre of Marcellus [36], and in the wall core of the Great Hall of Trajan's Markets [37].

2.5 Advanced chemical characterization techniques

These characterization techniques have been developed for use in the field of biomineralization to gain a better understanding of the complex structure-function relationships of heterogeneous mineralized tissues. SEM-EDS and Raman spectroscopy, for example, have been optimized to enable the collection of micron-resolution phase maps of polished sections of mantis shrimp appendages [38] and the brick-and-mortar nanostructures of mollusk nacre [11, 39]. These techniques have also been augmented for use on irregular sample surfaces. With the development of *TrueSurface*® profilometry, it has become possible to pair large area Raman spectroscopy with topography measurements through the use of a piezo-driven stages to maintain confocality. SEM-EDS systems have also been developed with multiple detectors to largely eliminate shadowing artifacts, which are frequently a problem encountered when acquiring elemental maps of irregular surfaces with a single X-ray detector. By harnessing the combined strengths of multi-detector SEM-EDS and profilometry-augmented Raman spectroscopy in the study of topographically complex sea urchin teeth, for example, the elemental distribution of dried sample surfaces could be measured using SEM-EDS under vacuum, or in the case of native hydrated samples, the position of the Raman ν_1 CO_3^{2-} peak could be used for measuring the extent of Mg substitution in the calcite crystal lattice [40].

In the study presented in the following chapter, these two techniques are used to characterize ancient Roman mortar samples obtained from the Privernum archaeological area in Priverno, Italy. An approach for correlating data from these two techniques, in which a transformation matrix that relates the two datasets is computed using their corresponding phase maps, is also presented. Quantitative SEM-EDS maps were collected for both Roman mortar cross-sections and fracture surfaces, and

the ratios of the resulting elemental compositions were then visualized using ternary density plots, which demonstrated distinct compositional differences.

Chapter 3

3D SEM-EDS and Raman chemical imaging of ancient Roman mortar

This chapter introduces the two primary chemical characterization techniques used in this thesis: scanning electron microscopy energy dispersive X-ray spectroscopy (SEM-EDS) and confocal Raman microscopy (CRM). This chapter reports on the the use of these two techniques in the study of ancient Roman concrete samples obtained from the archaeological area of Privernum (Priverno, Italy). The ancient Roman city of Privernum was occupied by the Volsci prior to being conquered and destroyed by the Romans in the 4th century BC. Though it recovered under Roman rule, Privernum eventually disappeared with the fall of the Western Roman Empire. Excavations of the Privernum archaeological area began in the 1980s, and although many of the artifacts that were excavated are now protected in the Archaeological Museum of Privernum and its associated storage, the site has undergone cyclical flooding and drying and sustained exposure to the elements, which have contributed to the deterioration of the structures held within it. In this chapter, the results of the SEM-EDS and CRM characterization of both cross-sections and the fracture surfaces of ancient Roman mortar samples from Privernum are presented.

3.1 Chemical Characterization Techniques

3.1.1 Sample preparation

The ancient Roman mortar samples investigated in this study were sourced from a perimeter wall (Fig. 3-1B and 3-1C) of Privernum archaeological area (3D reconstruction of the site shown in Fig. 3-1A). The samples were first embedded in a cold-cure epoxy and trimmed to size with a slow speed water-cooled diamond saw. The resulting samples were then progressively polished with diamond grinding disks from 60 grit to 800 grit, followed by final polishing using diamond suspensions down to 0.25 µm. Sample polishing was carried out by Wagner Petrographic (Lindon, UT).

3.1.2 Multi-detector environmental SEM-EDS

Multi detector SEM-EDS was performed (on both the polished cross-sections and the fracture surfaces of the samples) using a Tescan Vega GMU scanning electron microscope equipped with dual Bruker XFlash 5030 X-ray detectors. Typically, when SEM-EDS element mapping is conducted, a single detector is used to measure the X-rays emitted from the sample. This results in a shadowing effect, where parts of the topography may be situated between the sample area being measured and the detector, which would obstruct the X-rays en route to the detector and prevent their measurement. In multi-detector EDS, two diametrically-opposed detectors are used to detect the X-rays from the surface, which greatly reduces the shadowing effect and thereby allows for more reliable element mapping on rough surfaces.

Mapping data were acquired at a 15 mm analytical working distance at an accelerating voltage of 20 keV. Mapping times varied as a function of map pixel density as well as the specific elemental abundances in the phases being analyzed, but for all of the Ca to Si to Al phase diagrams generated in this work, acquisition times were always determined such that they resulted in a minimum of 5000 counts per pixel. The acquired spectra from each pixel were then used to calculate elemental ratios, which were then exported as single element quantitative maps and used for

Figure 3-1: **Collection location of the ancient Roman mortar samples used in this study.** **A**: 3D reconstruction of the Privernum archaeological site, collected using drone photogrammetry. **B**: 3D reconstruction of the wall from which the mortar sample was collected, using a DotProduct DPI-8 3D scanner, and **C**: a higher magnification photograph of the wall surface.

generation of the ternary diagrams.

3.1.3 Coupled profilometry and confocal Raman microscopy

Confocal Raman microscopy (CRM) differs from typical Raman spectroscopy, in that the Raman spectrometer is coupled with an optical microscope. This allows for the collection of Raman spectra on microscopic spot sizes on the surface of a sample. The spatial resolution is dependent on the wavelength of the incident beam, γ, and the numerical aperture, NA, of the objective being used:

$$\text{Spatial resolution} = \frac{0.61\gamma}{NA} \tag{3.1}$$

As a result, it is possible to obtain maps with sub-micrometer resolutions using CRM. The challenge with CRM, however, is that the surface of the sample must be in focus in order to collect a Raman spectrum, so usually, samples must be polished so that they are very flat if a Raman phase map (i.e. a map of Raman spectra) is to be collected. Recent developments in the design of confocal Raman microscopes have addressed this issue with the development of topography measurement techniques such as *TrueSurface*® profilometry, which allow for Raman phase mapping on irregular surfaces. By pre-measuring the topography of the sample and having a sample stage that is able to move in the vertical direction, the sample stage can follow the topographical map of the sample during confocal Raman phase mapping, all while maintaining confocality, thus enabling the collection of a Raman spectrum at every pixel throughout area of interest on the irregular surface of the sample.

For the Raman phase mapping of topographically complex fractured surfaces, surface profilometry measurements were conducted using WITec's *TrueSurface*® microscopy module, which maps three-dimensional surfaces using chromatic aberration techniques. A beam of white light is directed at the surface of the sample; since the components of this beam of white light have different focal distances, the elevation of a location on the sample may be deduced when the CCD camera detects a particular color. After measuring the topography, large-area CRM mapping was then executed and the resulting phase map collected. Raman phase mapping was conducted using a confocal Raman microscope system (alpha300R, WITec, Ulm, Germany). The system consisted of a frequency-doubled Nd:YAG 532 nm laser, which was used along with a multi-axis piezo scanner (P-527, Physik Instrumente, Karlsruhe, Germany) and a motorized large-area stage for sample positioning. As the sample was scanned, the system used the topographic information collected using TrueSurface profilometry to maintain confocality during large area mapping. Raman spectra were acquired using a thermoelectrically cooled CCD detector (DU401A-BV, Andor, UK) placed

behind the spectrometer (UHTS 300, WITec, Ulm, Germany) using a grating of 600 g mm^{-1}. Raman phase mapping was carried out at one-third maximum intensity to avoid damage to the sample. For each point on the sample at which a Raman spectrum was recorded, an integration time of 300 ms was used, and at each pixel, three spectra were recorded, and the average was taken. For each sample, an area of 8000 µm by 8000 µm was measured at a resolution of 200 pixels by 200 pixels. WITec Control FOUR (version 4.1, Witec) was used for data acquisition, and WITec Project FOUR (version 4.1, Witec) was used for cosmic ray removal, smoothing and background subtraction, as well as for conducting non-negative matrix factorization (NMF) to determine the spectra of individual phases contained within the total set of spectra collected during large area scans.

3.2 Chemical Characterization Results

3.2.1 Chemical imaging of the cross-section of ancient Roman mortar

In order to study the average composition of the samples collected from Privernum, SEM-EDS elemental and Raman phase maps of polished thin-sections of ancient mortar samples, shown in Fig. 3-2A and Fig. 3-2C, were collected. The total average SEM-EDS spectrum, shown in Fig. 3-2B, which shows the total number of X-rays emitted and their energies, describes the average elemental composition of the measured area. The maximum pixel intensity spectrum, which shows the maximum number of counts for a particular X-ray energy detected anywhere in the sample (which is especially useful for the identification of trace elements), is shown in Fig. 3-2B. The Raman spectra of the phases detected, extracted from the entire dataset using NMF, are shown in Fig. 3-2D in colors corresponding to the colors used in the Raman phase map in Fig. 3-2C.

Silicon-rich areas shown in green in the SEM-EDS map in Fig. 3-2A correspond to the grains colored green in Fig. 3-2C, which were identified as quartz, a major

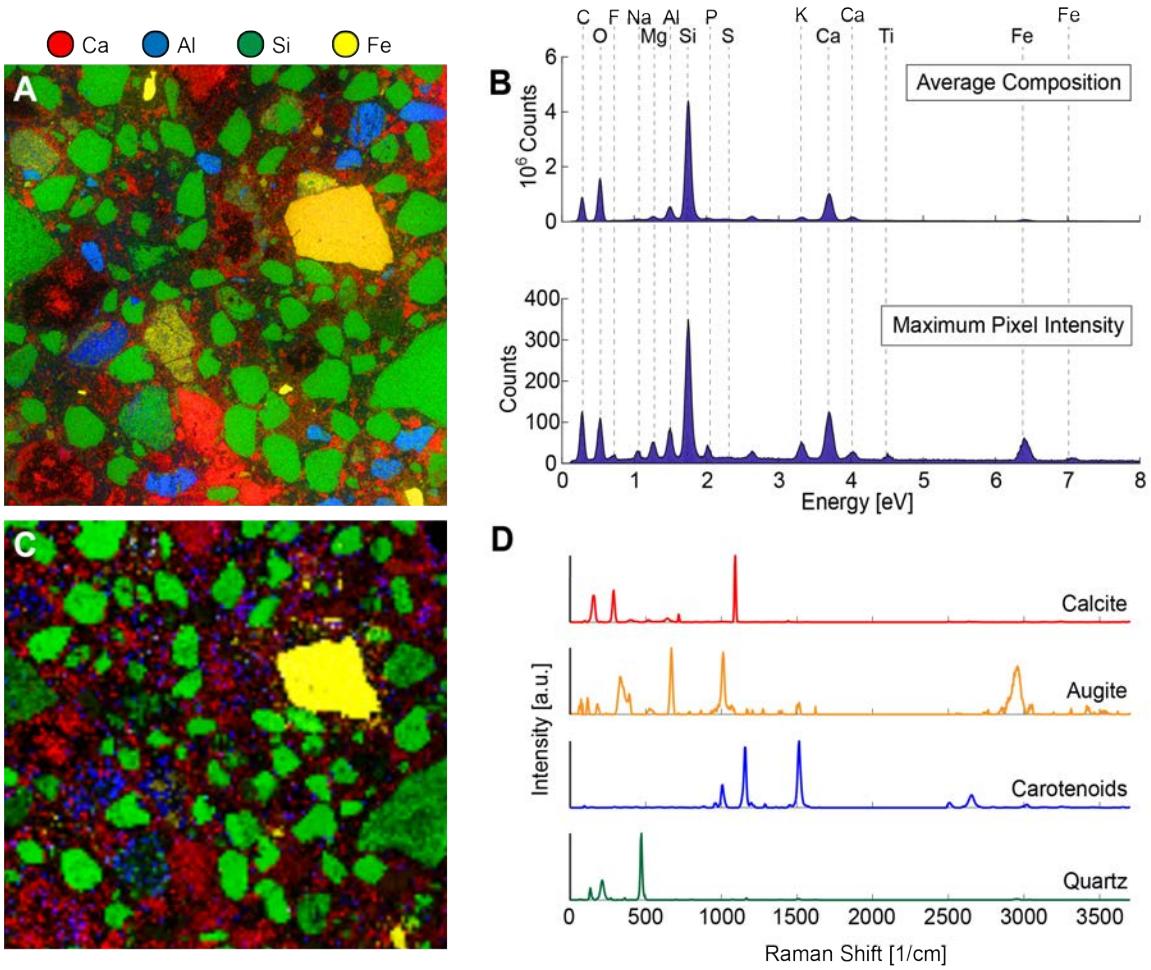

Figure 3-2: **SEM-EDS and Raman distribution maps of a polished thin section of ancient Roman mortar.** **A**: SEM-EDS elemental map of polished mortar sample. **B**: SEM-EDS spectra of shown sample area indicating the total average composition of the sample (upper) and the combined maximum pixel intensities of the detected elements (lower). **C**: Raman phase map of polished thin-section showing region measured using SEM-EDS and spatial distribution of **D**: the constituent spectra (which are color-coded corresponding to the different displayed map phases). Element and phase maps are each 3 mm by 3 mm.

component of the siliceous sand used to produce ancient Roman mortar. The calcium-rich areas in Fig. 3-2A correspond to the calcite-rich regions shown in Fig. 3-2C, and the iron-containing regions, colored yellow in both Fig. 3-2A and Fig. 3-2C, were found to produce characteristic Raman peaks for the rock-forming pyroxene mineral, augite [$(Ca,Na)(Mg,Fe,Al,Ti)(Si,Al)_2O_6$]. The region along the perimeter of the pore in the top-right corner and other regions colored blue in Fig. 3-2C were found to

consist of carotenoids, organic pigments produced by plants and algae, and some bacteria and fungi, likely present due to the exposure of the archaeological ruins to the environment. The cementitious binding phase in the regions between the aggregate yielded Raman spectra with large amounts of background fluorescence that obscured any detectable Raman signal. This is often an issue when a material contains features that absorb laser radiation, such as volcanic ash containing rare earth elements: a known component of ancient Roman cement.

3.2.2 Chemical imaging of the fracture surface of ancient Roman mortar

SEM-EDS and CRM were also used to generate phase maps of the fracture surface of a Roman mortar sample from the same region of the perimeter wall. Through observation by eye, one can see that the proportion of aggregate on the fracture surface is much lower than the proportion of aggregate visible in the cross section. Therefore, data collected on the fracture surface is expected to be more representative of the cementitious binding phase, whereas data collected for the polished thin section would provide more information about the average composition, including the aggregate composition, of the mortar. Fig. 3-3A and Fig. 3-3B show the Raman phase map of the fracture surface and the corresponding Raman spectra of the phases detected using the same color scheme: quartz in green and calcite in red. Although quartz aggregate and calcite are still observed, a much larger region of the measured area yields Raman spectra with high background fluorescence, supporting the assessment that the fracture surface contains a greater proportion of the cementitious binding phase.

Fig. 3-3C shows both the quantitative and normalized SEM-EDS elemental maps obtained for the fracture surface. The corresponding total counts for the X-rays emitted at different energies and the maximum number of counts detected anywhere on the measured area, indicated by the white box on the sample in Fig. 3-3C, are shown in the SEM-EDS spectra in Fig. 3-3D. The Raman phase map of the region

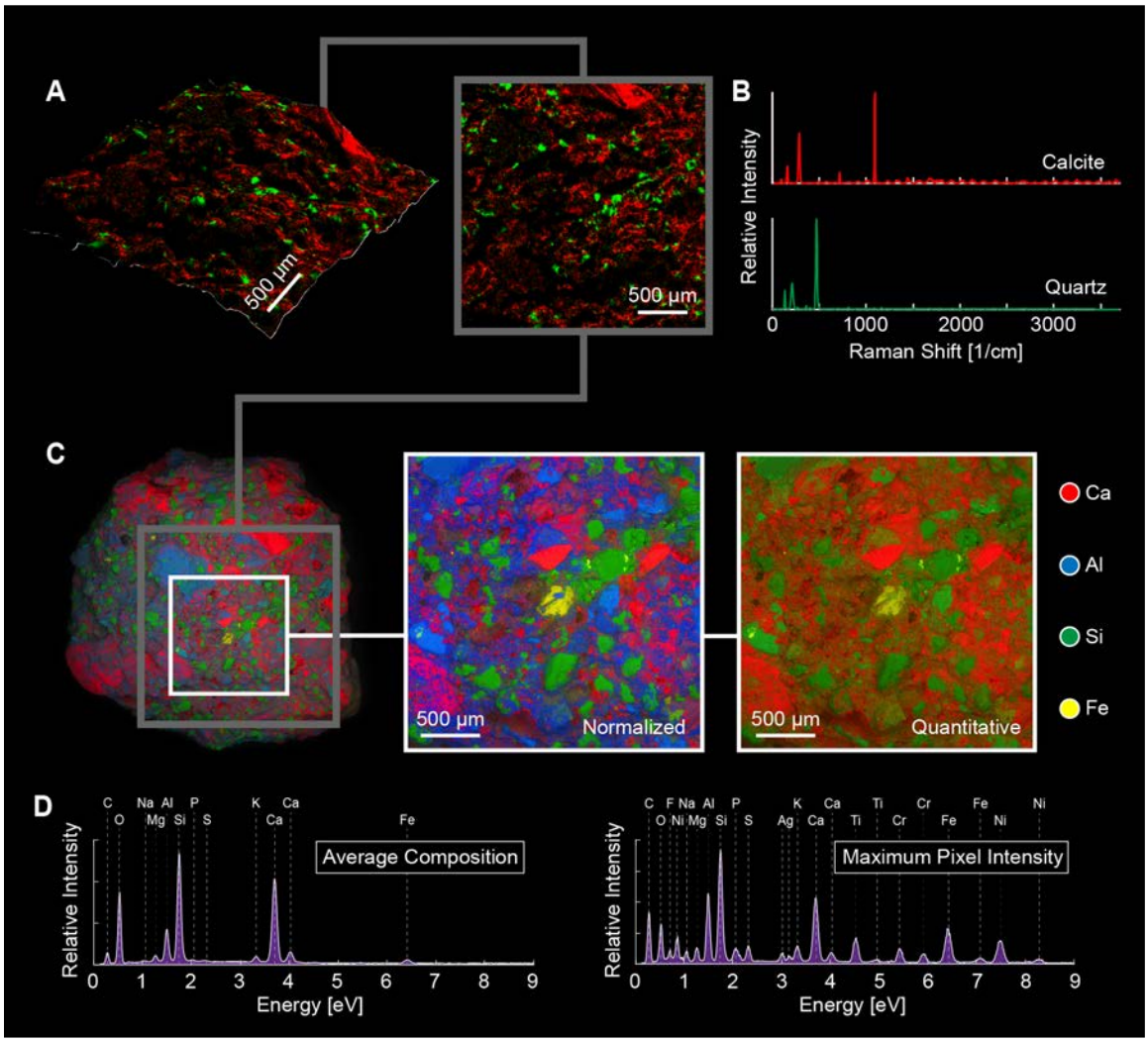

Figure 3-3: **SEM-EDS and Raman distribution maps of the fractured surface of a sample of ancient Roman mortar.** **A**: 3D and plan views of Raman phase map. **B**: Constituent Raman spectra (color-coded corresponding to the different displayed map phases). **C**: SEM-EDS elemental map of the fracture surface of the mortar sample, with normalized and quantitative element maps of region within white square. **D**: SEM-EDS spectra for the entire element map indicating the total average composition of the sample (left) and the combined maximum pixel intensities of the detected elements (right).

indicated by the grey box in Fig. 3-3C is shown superimposed on the topography of the surface in Fig. 3-3A. The corresponding Raman spectra of the detected phases, calcite and quartz, shown in red and green respectively, were extracted from the total dataset using NMF and are presented in Fig. 3-3B.

3.3 Summary

Primary phases in the Privernum mortar samples were detected using large-area confocal Raman phase mapping. For fractured samples with intrinsically irregular surface topographies, profilometry measurements were collected to generate a 3D surface map, which was then used in conjunction with the Raman microscope's motorized piezo stage to maintain the constant intersection of the sample surface with the focal plane. This approach enabled the detection of a Raman signal over the entire area of interest, while maintaining confocality (Fig. 3-3).

While Raman spectroscopy is extremely useful in identifying phases that consist of Raman active chemical bonds, this technique loses its utility when there are complex phases in materials that have no distinct stretching or bending modes that give a clear Raman shift. EDS, in contrast, is able to map the elements present on a sample's surface, and while it cannot identify specific phases, it may be used to obtain compositional information that could be used to determine the phases present where they cannot be successfully identified using Raman spectroscopy. In addition, the use of multiple SEM-EDS detectors for signal acquisition provides a relatively uniform coverage of samples with complex surface topographies, while largely minimizing shadowing artifacts that commonly occur when single detector systems are employed.

Furthermore, the need for minimal sample preparation (fractured samples were simply fixed to slides using minimal adhesive to avoid sample movement during phase mapping) dramatically reduces the potential for surface contamination, which can occur during resin embedding, sectioning, and polishing processes that are traditionally employed in the characterization of these materials. Studying the fracture surface also allows for the identification of mechanically weak interfaces, which could be the phases that ultimately lead to material failure. Although the focus of this work was on the characterization of ancient Roman mortar, the techniques and tools presented in this study could be applied to the characterization of a wide range of complex, heterogeneous materials with irregular surfaces.

Chapter 4

Computational tools for the analysis of chemical characterization data

In this chapter, computational tools developed to be used in conjunction with the spectroscopic techniques presented in Chapter 3 are presented. First, the image processing-based methodology for correlating data obtained using these two techniques is described. Next, large quantified SEM-EDS datasets are used with calcium-silicon-aluminum (Ca-Si-Al) ternary diagrams to study the phases present in cementitious materials. Finally, unsupervised learning techniques are applied to high-resolution maps of quantified SEM-EDS data to show the distribution of chemically distinct phases in ancient Roman mortar.

4.1 Correlation of complementary SEM-EDS and Raman datasets

One of the challenges in using complementary chemical characterization techniques to study heterogeneous samples is repeatedly finding the precise locations where data has been previously collected. This problem is less challenging when regions of a sample are easily distinguished by eye, but it becomes progressively more challenging with sample heterogeneity or complexity. As an example, when looking at a very

large (centimeters wide) region of ancient Roman concrete, it becomes challenging to find a particular region of cement near a particular grain of sand (Fig. 4-1).

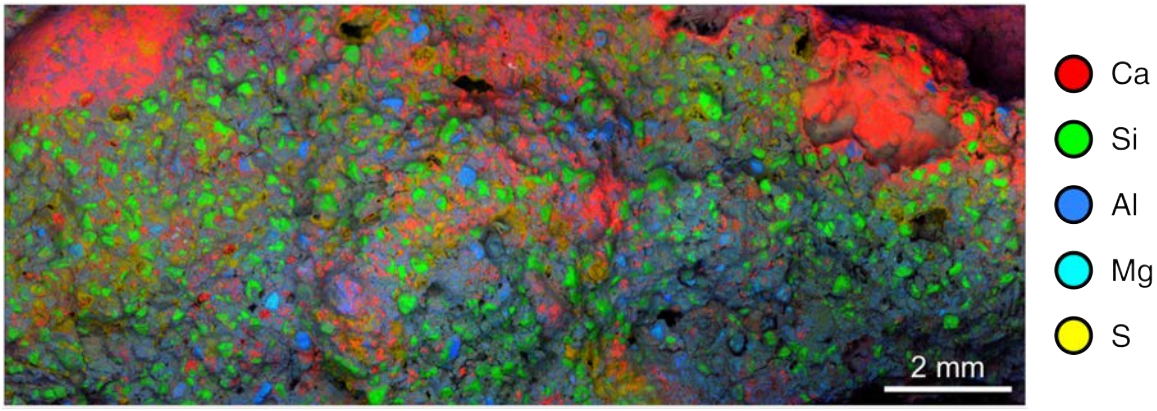

Figure 4-1: **Normalized SEM-EDS map of the fracture surface of an ancient Roman mortar sample from the Privernum archaeological area.** Data collected by Dr. James C. Weaver.

The Raman phase map in Fig. 4-2E was collected on the same sample for which an optical micrograph, BS-SEM image and SEM-EDS map are shown in Fig. 4-2A-Fig. 4-2C. However, the Raman phase map was collected for a different measured area orientation. Different views of the same three-dimensional object are related to each other by a projective transformation known as the planar homography: a 3×3 transformation matrix that relates the two planar projective spaces. Thus, data collected using the two measurement system s for two different views of the sample can be correlated by computing the corresponding homography matrix, $\mathbf{H}$, that relates them. When the resulting transformation is applied to the SEM-EDS map shown in Fig. 4-2C, the transformed SEM-EDS map shown in Fig. 4-2F is obtained, and one may then directly compare Raman spectra to quantified SEM-EDS data, pixel by pixel.

To enable the pixel by pixel comparison of data, one must first ensure that the images match the resolution of the data collected. Therefore, the Raman phase map was first resized to 200 by 200 pixels to match the 40,000 Raman spectra encoded in the phase map. Since the SEM-EDS map was generated using the underlying quantified elemental data, its resolution matches the resolution of the data collected

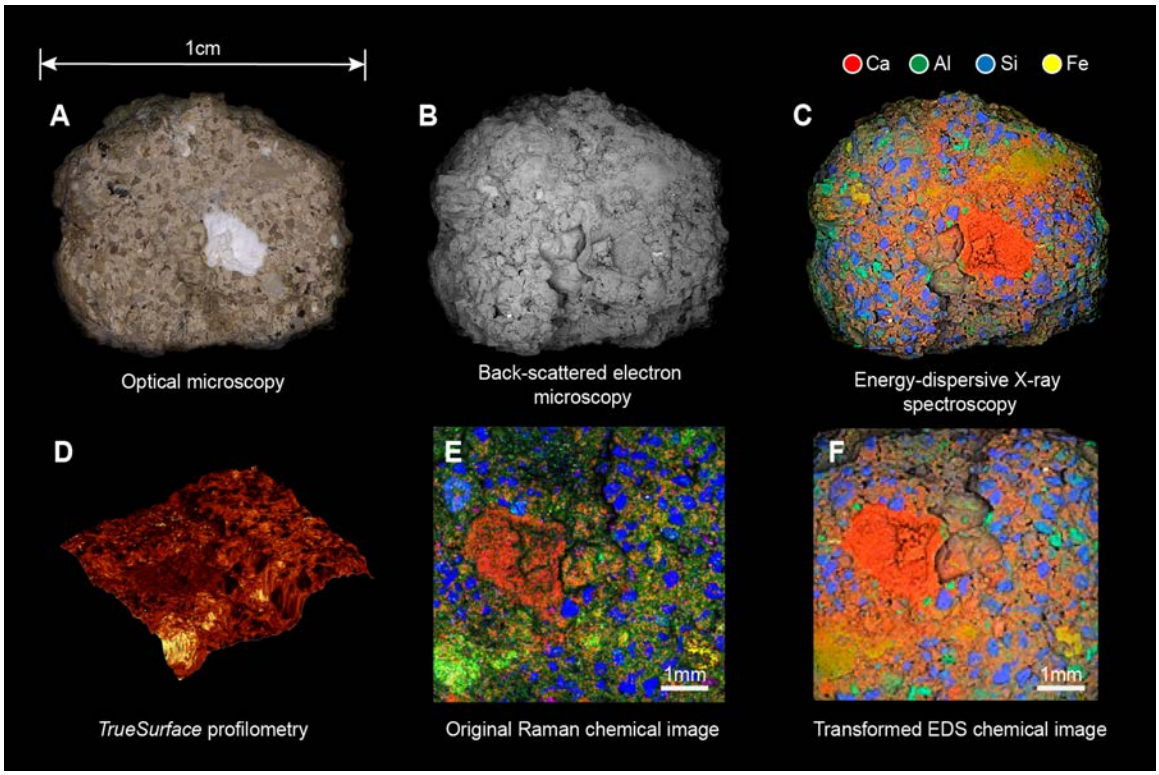

Figure 4-2: **Chemical characterization of ancient Roman mortar.** Images obtained using **A**: optical microscopy, **B**: backscattered scanning electron microscopy (BS-SEM), **C**: scanning electron microscopy energy dispersive X-ray spectroscopy (SEM-EDS), and **D**: profilometry, which measures sample topography. **E**: Raman phase map of the region in **D** (blue: quartz, red: calcite) and **F**: EDS element map transformed into that region's coordinate system.

at the time of map generation.

The 8 unknowns, H_{ij}, of the 3x3 homography matrix, **H**, (defined in Eqn. 4.1) may be solved for using the x- and y-coordinates of at least four corresponding locations on each phase map, but the greater the number of corresponding locations used, the smaller the error associated with the resulting homography matrix. The relationship between the coordinates in the two phase maps is shown in Eqn. 4.2, in which (x, y) are the coordinates of a point in the image to be transformed and (x', y') are the coordinates of the corresponding point in the second image.

$$\mathbf{H} = \begin{bmatrix} H_{11} & H_{12} & H_{13} \\ H_{21} & H_{22} & H_{23} \\ H_{31} & H_{32} & 1 \end{bmatrix} \tag{4.1}$$

$$\begin{bmatrix} x' \\ y' \\ 1 \end{bmatrix} \sim \mathbf{H} \begin{bmatrix} x \\ y \\ 1 \end{bmatrix} \tag{4.2}$$

The `homography` function from the Machine Vision Toolbox [41] was used to compute the components of **H** representing the planar homography using several corresponding locations from the two datasets and transform the SEM-EDS element map into the projective space of the Raman phase map. At this point, the same transformation may also be applied to the quantitative SEM-EDS element maps to enable the direct comparison of Raman spectra to element quantities.

4.2 SEM-EDS and ternary diagrams for the study of cementitious materials

EDS element maps were collected for the fracture surface of a sample of ordinary Portland cement, the fracture surface of a sample of ancient Roman mortar, and the polished cross-section of a sample of resin-embedded ancient Roman mortar. Schematics of these samples and the their normalized element maps are shown in Fig. 4-3A-C and Fig. 4-3G-I, respectively. Fig. 4-3D-F show the ternary density plots of the three sets of SEM-EDS data, which were generated as follows:

1. The SEM-EDS data was quantified and exported as 16-bit greyscale maps for each element, in which the greyscale intensity value of a pixel corresponds to the atomic percentage of that element at that location in the measured area. A white pixel corresponds to an atomic percentage of 100%, and a black pixel corresponds to an atomic percentage of 0%.

2. The quantitative maps of the three major elements of interest, calcium, silicon, and aluminum, were used to compute the ratios of those elements relative to each other (where Ca + Si + Al = 1) for all pixels of the mapped area.

3. The Si-Ca-Al ratios computed for each pixel were converted to ternary coordinates and plot on ternary axes. If a pixel contained silicon, but no calcium or aluminum, it would lie at the Si vertex of the diagram. If a pixel contained calcium and aluminum, but no silicon, it would lie on the Ca-Al axis.

4. The pixels on the ternary plots were colored according to the density of coordinates on the plot. The most densely populated regions of the ternary diagrams were colored yellow, and the least densely populated regions were colored purple, as indicated by the color bars below Fig. 4-3D-F.

Researchers in the cement characterization field have previously developed ternary frequency diagrams for representing SEM-EDS data; by dividing each of three ternary axes into n bins, a 2D ternary histogram consisting of n^2 bins is generated. The ternary coordinates are then sorted into bins, and the number of coordinates in each bin is shown using an intuitive color map, which allows for the rapid identification of the major phases present [32].

Fig. 4-4 shows the implementation of two visualization tools that were developed for use in conjunction with the ternary density plots shown in Fig. 4-3. In Fig. 4-4A-Fig. 4-4C, elliptical sub-regions of the ternary density plots were selected, and the pixels corresponding to those ellipses were colored with the same colors in Fig. 4-4D-F. In Fig. 4-4G-I, a color was assigned to each of the three vertices of the ternary diagram, and each ternary coordinate was colored as a mixture of the three colors corresponding to the Ca-Si-Al ratio it represents. The corresponding pixels were then colored using this same color space to enable the visualization all of the different phases present in the entire mapped regions (Fig. 4-4J-L).

The ternary density plot for OPC (Fig. 4-3D) shows most ternary coordinates lying close to the Ca/Si axis, with a very densely populated cluster close to the Ca vertex. This suggests a very large proportion of C-S-H and low-alumina C-A-S-H,

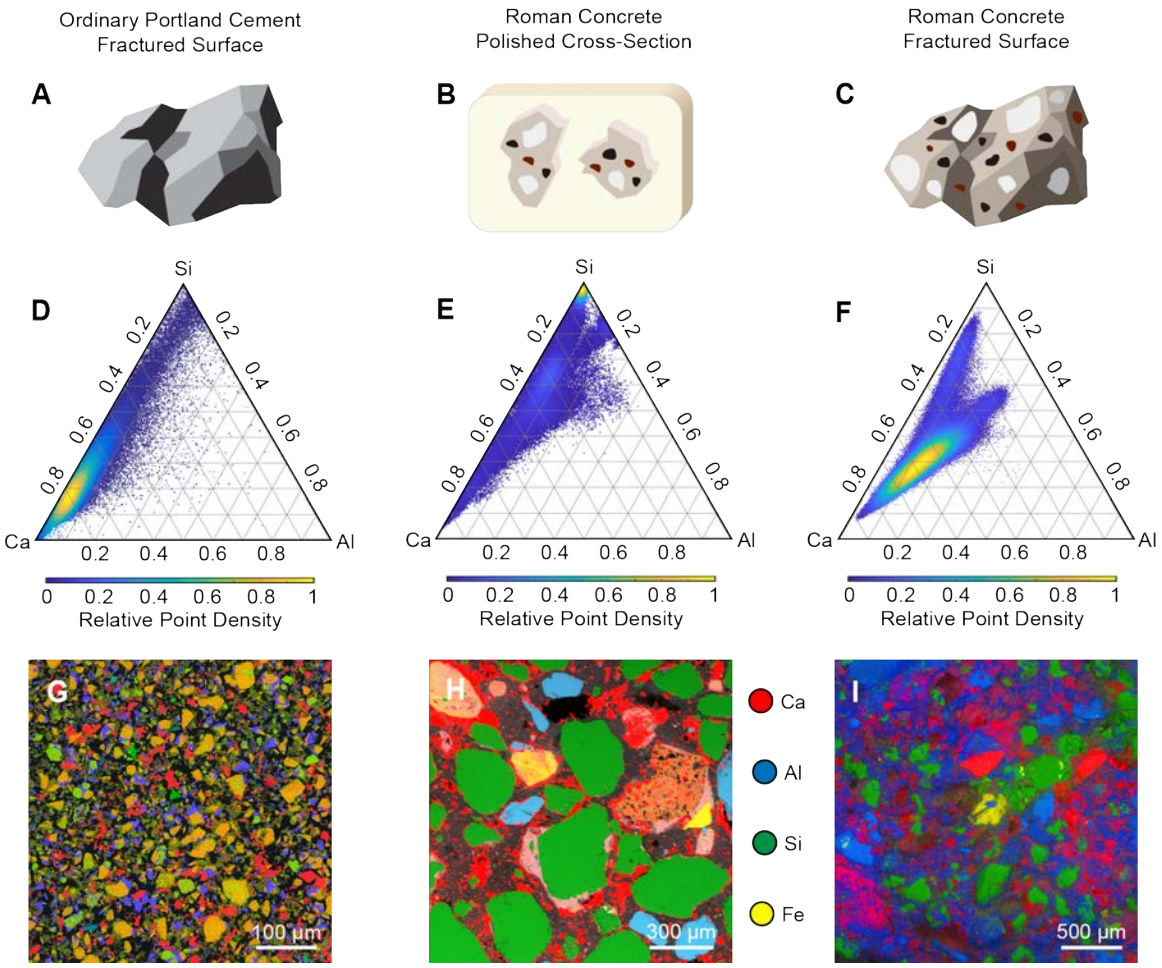

Figure 4-3: **Ternary density plots and SEM-EDS phase maps of ordinary Portland cement and ancient Roman mortar.** Schematics of **A**: the fractured surface of an ordinary Portland cement sample, **B**: the polished cross-section of ancient Roman concrete that has been embedded in resin, and **C**: the fractured surface of an ancient Roman mortar sample. Below the sample illustrations (upper row, **D-F**) are the ternary density plots (middle row) showing ratios of Ca to Si to Al at each pixel in the different SEM-EDS maps (bottom row, **G-I**). For each of the ternary density plots, the purple regions are most sparsely populated and the yellow regions are most densely populated.

which is expected for OPC [42]. The ternary density plot for the fracture surface of ancient Roman mortar (Fig. 4-3F), however, shows coordinates clustered away from the Ca-Si axis. The large dense cluster corresponds with the region occupied by higher-alumina C-A-S-H, suggesting a much greater presence of this binding phase in the ancient Roman mortar sample than in modern cement. The "arm" of the ternary coordinates closer to the top of this ternary density plot corresponds to sand

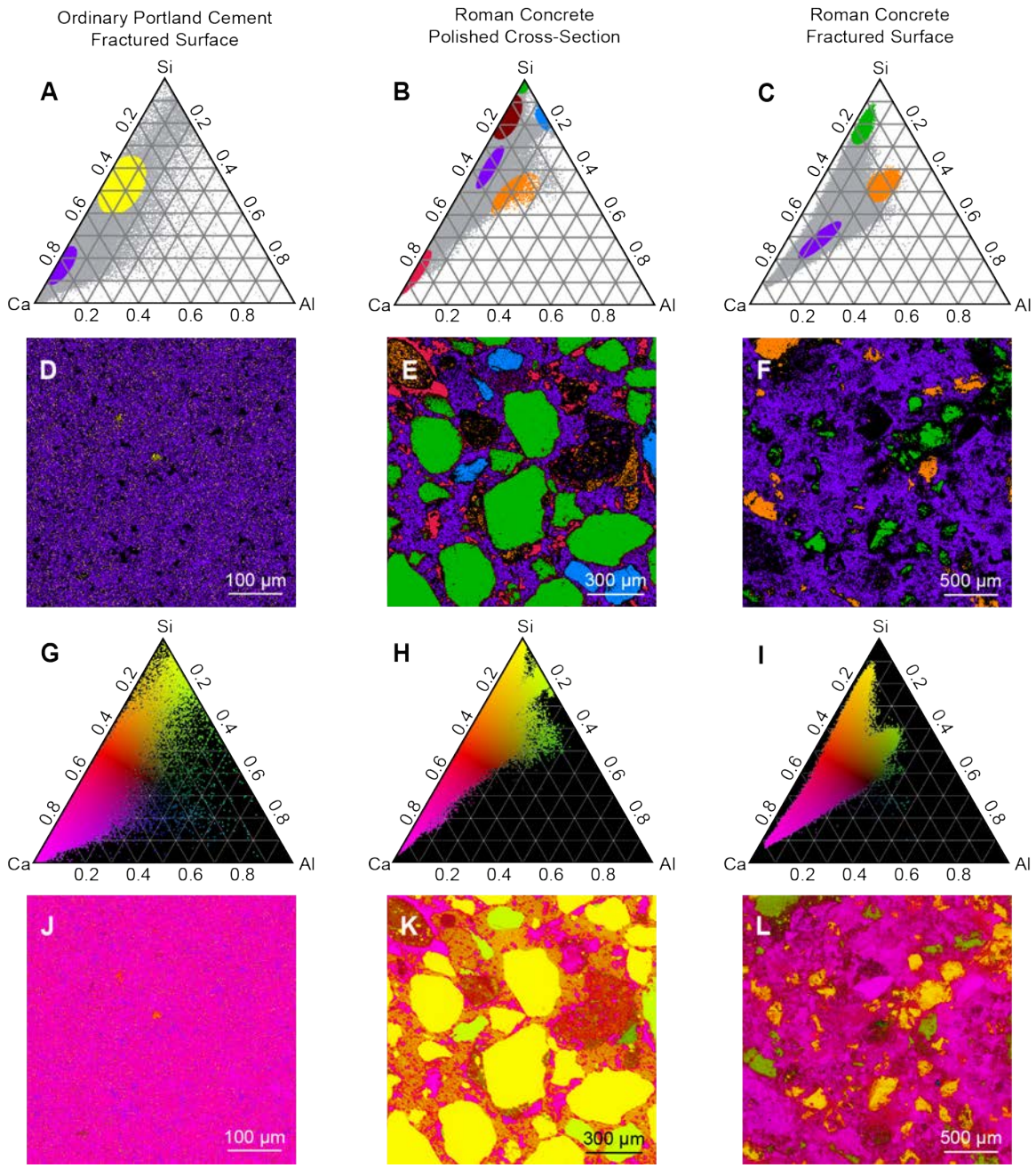

Figure 4-4: **OPC and Roman mortar phase identification and mapping.** The leftmost column is the fractured surface of OPC, the middle column is the polished cross-section of ancient Roman mortar, and the rightmost column is the fractured surface of ancient Roman mortar. **A-C**: All ternary coordinates are shown in grey, and points within particular ellipses are colored and the corresponding SEM-EDS pixels are indicated in **D-F**. **G-I**: A color gradient is used to color each ternary coordinate based on its position in the ternary diagram, and its corresponding pixel is colored the same color in **J-L**.

grains that are partially covered with binder, which shifts its coordinates away from the Si vertex. This is corroborated by comparing the phase map in Fig. 4-4F with the corresponding Raman phase map showing quartz distribution in Fig. 3-3A. The second arm of coordinates (orange in in Fig. 4-4C and Fig. 4-4F) extends towards the center of the ternary diagram where coordinates corresponding to natural pozzolans (e.g. volcanic ash) would be found [43].

The ternary density plot for the polished cross-section of ancient Roman mortar provides more insight into its average composition. The cluster at the very top of the ternary diagram close to the Si vertex corresponds to quartz aggregate. The region in the red ellipse in Fig. 4-4E, which corresponds to the calcium-rich hydrated binding phase that occupies the region on the ternary diagram in which C-S-H would also be found, is found in the binder of the Roman mortar cross-section but is notably absent from the fracture surface of Roman mortar. Since a material would fracture along its weakest component, this suggests that the higher-alumina C-A-S-H found on the fracture surface is weaker than the lower-alumina C-A-S-H and calcium-rich hydrated binding phase that is more prevalent in the polished cross-section. Other aggregates found in the Roman mortar that are richer in aluminum are colored blue and shown in Fig. 4-4B and Fig. 4-4E. The majority of the binder appears to be some form of C-A-S-H, but the binder that is located near the perimeter of the quartz aggregate is richer in silicon (colored burgundy in Fig. 4-4B and Fig. 4-4E). Expectedly, natural pozzolans, colored orange, are found in both the polished cross-section and on the fracture surface of the ancient Roman mortar sample.

4.3 Unsupervised learning and quantitative SEM-EDS elemental data

4.3.1 Background: Clustering techniques in the study of materials

In this section, it is demonstrated how unsupervised learning may be used with large area, high-resolution, spatially resolved SEM-EDS data to generate phase maps. In the previous section, it was shown that particular ratios of the major elements (Ca, Si, Al) corresponded to distinct phases present in the mapped regions, and it was shown that when different groupings of datapoints in the ternary plots are selected and mapped onto the original sample area, phases such as sand, high-Ca binder, and aluminosilicate aggregate grains could be identified. The work presented in this section shows that by partitioning the SEM-EDS data with respect to *all* quantifiable elements, every pixel of the mapped area can be assigned to a chemically distinct phase. The procedure presented in this section is well-suited for poorly understood composite materials, such as ancient Roman mortar and concrete, since it does not require that the operator know what phases to expect or even the number of phases a priori.

Unsupervised learning, which does not require that constituent groups of a dataset be known a priori, can be useful in the study of materials since it may be used to identify patterns in large datasets [44]. When used with SEM-EDS data for particulate matter, unsupervised learning techniques have been used to group soil particles into different types [45], sort sediment particles from various Amazonian rivers [46], and distinguish types of airborne particulate matter to determine their emission sources [47, 48, 49]. Previous studies have also used various algorithms with spatially resolved chemical data to partition images of samples based on chemistry. Non-negative matrix factorization has been used with SEM-EDS spectra to map the phases present in igneous rock samples [50], fuzzy c-means clustering has been used with hyperspectral images to map the phases present in a solder bump [51], and a modified hierarchical

clustering algorithm EFE-HCA (Extremely Fast and Efficient Hierarchical Clustering Algorithm) has been used to distinguish different types of wires in an epoxy matrix [52]. Principal component analysis (PCA) has been used with X-ray fluorescence (XRF) data to identify the eigenimages of biological specimens, such as cells and bacteria, some of which correspond to components, such as the nucleus or cytoplasm [53]. Combinations of PCA and k-means clustering have been used with micro-XRF data to maps the phases present in granite and Roman glass in 2D [54] and in an inclusion in a natural diamond sample in 3D [55]. Mapping the phases present in highly heterogeneous composites, such as cementitious materials, has previously been conducted by applying a two-step classification algorithm developed for classifying hyperspectral satellite images [56], but as a classification technique, it requires that the spectral signatures of the constituent phases be known a priori and supplied as training points for the algorithm [57].

The work in the following section shows that by choosing k-means clustering, which is an unsupervised learning technique, over classification techniques that require that the phases present be known a priori, the approach may be applied to heterogeneous composites of unknown composition in general. Furthermore, since a technique for model selection is included, the operator also does not need to know the number of phases present in advance.

4.3.2 Fuzzy c-means clustering in the study of remnant lime clasts in ancient Roman mortar

Ancient Roman mortars and concretes have survived millennia, but mechanistic insights to their durability remain largely a mystery. Micro computed tomography (µCT) studies of the Privernum mortar samples, conducted by Linda Seymour, have shown that the samples have a diffusional tortuosity of 4.8, which is similar in value to the diffusional tortuosity of modern OPC mortars that have been subjected to artificial aging [58, 59, 60]. This suggests the presence of a mechanism in ancient Roman mortar that has allowed for the replacement of material that has been lost

through degradation processes. In fact, when observing the material along the pore space in ancient Roman mortar, one sometimes finds that the cementitious matrix is rich in sulfur, which is a result of the degradation pathway in which sulfate ions (from acid rain, for example) displaces carbonate ions in insoluble calcium carbonate to form soluble calcium sulfate, but in other instances, finds that the material along the pore space is rich in calcium, which suggests the occurrence of a recrystallization process that has led to the reinforcement of the matrix (Fig. 4-5).

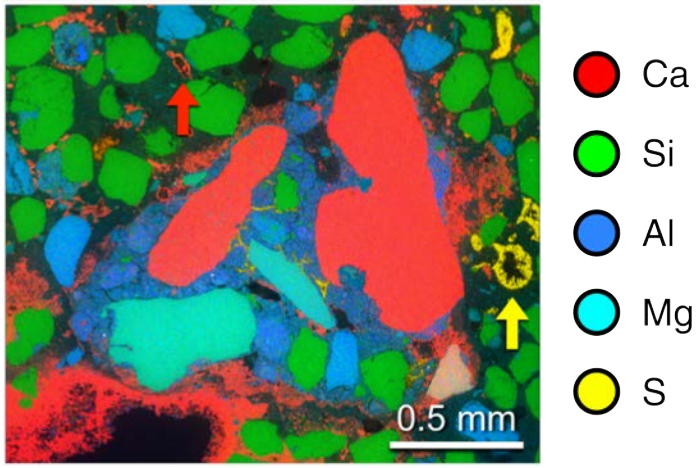

Figure 4-5: **Normalized SEM-EDS element map of the cross-section of a sample of ancient Roman mortar.** The large red inclusions are examples of the remnant lime clasts often found in both marine and architectural ancient Roman mortars. The arrows show the positions of two pores in the matrix, one showing signs of sulfur-degradation (yellow) and one showing potential reinforcement of the matrix with recrystallized calcium-rich material (red).

There have been numerous recent studies of the chemical and mineralogical processes in ancient pozzolanic mortars and concretes that have contributed to their resilience. Studies of Roman concrete in marine environments have suggested that remnant lime clasts may have reacted over time with amorphous aluminosilicates within the matrix in the presence of water, resulting in the precipitation of C-A-S-H which then recrystallized as Al-tobermorite [22]. These lime clasts, which may be present as a result of a variety of processes that may have occurred during concrete production [61, 62, 63, 64], have previously been found to be heterogeneous and have been found to contain calcite, vaterite, brucite, C-A-S-H, and Al-tobermorite

[22, 63, 13, 12, 65, 66]. Prior studies of remnant lime clasts in ancient Roman marine mortars have shown that partially dissolved clasts are calcite-rich at the core and have a perimeter primarily comprised of C-A-S-H, and outside the perimeters of these clasts, hydrocalumite (formed during the alkaline activation of aluminosilicates) and ettringite (a phase that is formed during the hydration of modern OPC following the reaction of calcium aluminate with calcium sulfate) have been identified [63]. In order to observe the differences in composition both within and around the remnant lime clasts, fuzzy c-means clustering was used to partition the quantitative SEM-EDS data.

Fuzzy c-means clustering

Unsupervised learning, or clustering, techniques can fall into the categories of hard (or non-fuzzy) clustering or fuzzy clustering. In hard clustering, each data point can belong to exactly one cluster, whereas in fuzzy clustering, data points can belong to multiple clusters. If they belong to multiple clusters, they are assigned membership grades for each cluster, with higher membership grades corresponding to a higher degree to which a data point belongs to that cluster.

In fuzzy c-means clustering, the operator chooses the number of clusters into which the dataset is to be partitioned. The algorithm randomly assigns membership values for each of the data points for each of the clusters. An objective function, computed using the data points, their membership values, and the centroids of each cluster, is then iteratively minimized until the change in the objective function between subsequent iterations falls below a predetermined threshold.

Ternary diagram study and clustering of the remnant lime clast SEM-EDS element data

A quantitative analysis of the elemental composition of the lime clasts was conducted in two modes: on a freshly fractured surface (Fig. 4-6A-B) and a prepared, polished cross-section (Fig. 4-6C-D). Quantitative EDS data were plotted pixel by pixel on Ca-Si-Al ternary axes (Fig. 4-6A,C) to reveal the relative ratios of the three key

elements of the cementitious phases [67]. Immediately evident is the shift in the fractured surface towards the calcium vertex of the ternary diagram, suggesting that the sample likely failed along weaker binding phases, the lime clast, and binder immediately surrounding the clast. Quantitative EDS data were clustered using fuzzy c-means clustering (Fuzzy Logic Toolbox, MATLAB R2018a), another unsupervised learning technique, to visualize the distribution of subtle differences in composition throughout the mortars. Fuzzy c-means clustering differs from hard clustering like k-means clustering, in that each data point may be a part of multiple clusters. This assumption holds for this purpose, since a given 3Âţm by 3Âţm pixel of the measured area may encompass more than one phase. The algorithm assigns membership values to each data point for each cluster, and the cluster for which each data point had the highest membership value was used to segment the data. Using this technique, each dataset was divided into clusters, and the number of clusters was increased until the map was appropriately segmented. Clustering was performed on an n by 5 array of EDS data, where n equaled the number of pixels in the EDS map of interest and each column contained the amount of each of the five elements of interest (oxygen, silicon, calcium, magnesium, and aluminum) in atomic percent.

Points on the ternary diagrams (Fig. 4-6A,C) as well as individual pixels on the original map area (Fig. 4-6B,D) were then colored based on the assigned cluster. Within the polished cross sections (Fig. 4-6D), the lime clasts separate into two clusters: one around the clast perimeter and another in the core. Evident here is a transition from the calcium-rich core to a rim with higher concentrations of silicon and aluminum. Just outside of the lime clasts and extending to the edge of the sample, a matrix phase rich in calcium with aluminum and silicon incorporated can also be seen. These points (red) are distinct from the primary binding phase (yellow) which has ratios of silicon, aluminum, and calcium more closely associated with C-A-S-H binders [67]. Through petrographic analysis, conducted by Linda Seymour, it was shown that the binder is predominantly isotropic, as would be the expected product from the pozzolanic reaction (poorly crystalline C-A-S-H), with calcite occurring in the matrix near lime clasts and some pores.

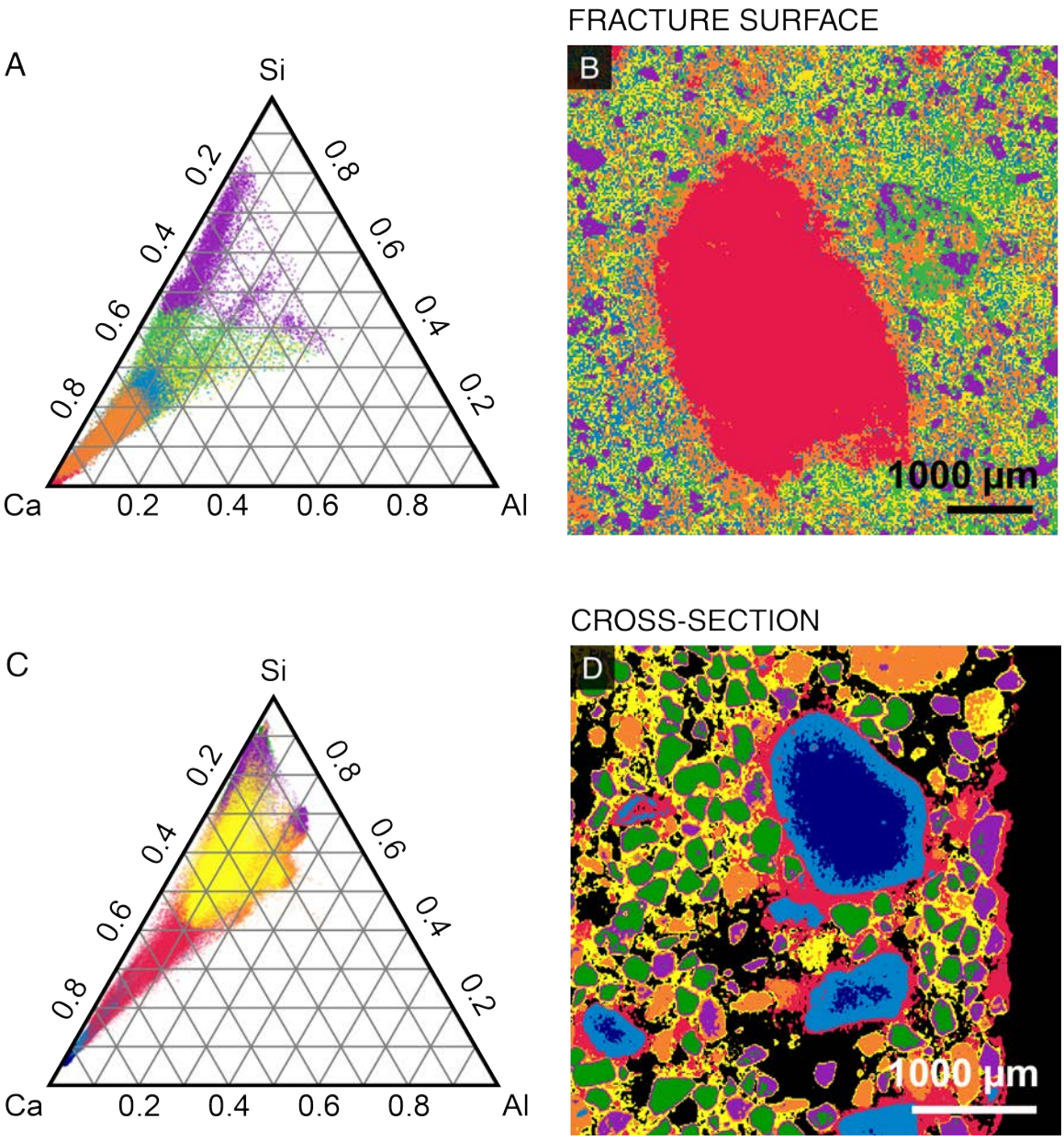

Figure 4-6: **SEM-EDS compositional analysis of ancient Roman mortar samples.** Ternary diagrams and phase maps showing the clusters of SEM-EDS data as obtained using fuzzy c-means clustering. Results are shown for **A**: a freshly fractured surface of a lime clast in a mortar sample and **B**: a polished cross-section.

In this study, it was demonstrated that the phases present in heterogeneous lime clasts, which are often observed in ancient Roman mortar samples, were distinguishable through the clustering of quantitative SEM-EDS elemental data. By mapping the phases present, it was shown that the inner lime clasts are lower in silicon and

aluminum than the outer lime clasts, which suggests the formation of C-A-S-H like phases, possibly via the reaction of the material contained within the lime clasts with amorphous aluminosilicates in the surrounding matrix in the presence of water.

In this study of the remnant lime clasts, the objective was to detect differences in calcium composition within and around the clasts, which could then be compared using Ca-Si-Al ternary diagrams. Prior to this analysis, these lime clasts had been characterized using Raman microscopy (Fig. 4-2) and were known to be primarily composed of calcite. Therefore, the types of phases present and the expected differences were known beforehand. As such, the methodology used, in which the data was fit with many clusters, which were then plot on the ternary diagrams to observe compositional differences, was suitable in this case. However, in the study of composites of unknown composition in general, the types of phases to expect and the number of phases present tend to not be known by the operator beforehand, so another method must be used to determine this information. In the following section, it is demonstrated how this can be done using k-means clustering with the Calinski-Harabasz method of model selection.

4.3.3 Standard k-means clustering

In the process of k-means clustering, a hard clustering technique, a dataset or set of observations is partitioned into a predetermined number, k, of clusters. First, k centers are randomly selected, then each observation is assigned to the cluster associated with the center to which it is closest. The center of each cluster is then recalculated after the assignment, and the process is repeated until the assignments of observations to clusters no longer changes (see Fig. 4-7). Whereas fuzzy c-means clustering, which was used to partition the Roman mortar data in Section 4.3.2, allows each observation to belong to multiple clusters and assigns membership grades indicating the extent to which observations belong to different clusters, k-means clustering assigns each observation to a single cluster.

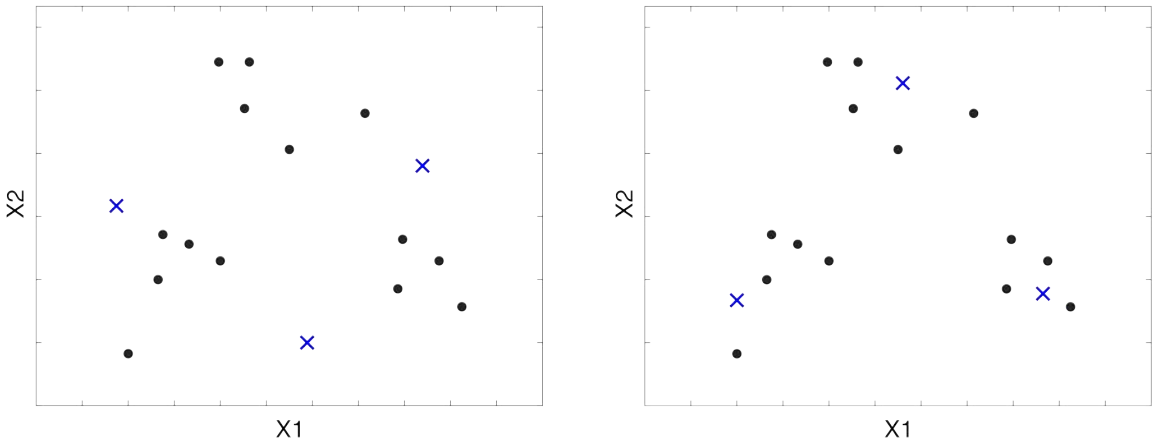

Figure 4-7: **Repeated selection of cluster centers.**

4.3.4 Treatment of quantitative SEM-EDS data prior to k-means clustering

The SEM-EDS datasets presented in this chapter were all collected at a resolution of 512 pixel by 512 pixels. The SEM-EDS map spectra were then ca'ted and the data was quantified using Bruker's ESPRIT 2.1 software using the built-in Linemarker PB-ZAF correction, which corrects for background radiation, atomic number effects, absorption of X-rays by the specimen, and fluorescence. The SEM-EDS element maps were quantified using bins of 2 pixels by 2 pixels in order to improve the statistics in determining the atomic percentages of each detected element throughout the mapped area, which resulting in quantified maps of resolution 256 pixels by 256 pixels. For all the maps collected, significant amounts of carbon and oxygen were detected, but these were excluded from the k-means analysis since they are difficult to quantify reliably due to the ease of adsorption of CO_2 and O_2 onto the sample surface and surfaces within the SEM chamber.

The set of elemental data for the remaining N reliably quantified elements used to perform k-means clustering is as follows

$$\mathbf{X} = [\mathbf{X_1}, \mathbf{X_2}, \ldots, \mathbf{X_{N-1}}, \mathbf{X_N}] \tag{4.3}$$

where

$$\mathbf{X_i} = \left[x_1^i, x_2^i, \ldots, x_{256^2-1}^i, x_{256^2}^i\right]^\top \tag{4.4}$$

and x_n^i is the atomic percentage of the ith element present at the nth of each of the 256^2 pixels of the mapped area. In order to ensure that all the quantified elements had the same dimensionality prior to performing k-means clustering, the data was normalized as follows:

$$\mathbf{X_i^{norm}} = \frac{\mathbf{X_i} - \mu_{\mathbf{X_i}}}{\sigma_{\mathbf{X_i}}} \tag{4.5}$$

where $\mu_{\mathbf{X_i}}$ is the arithmetic mean of $\mathbf{X_i}$ and $\sigma_{\mathbf{X_i}}$ is the standard deviation of $\mathbf{X_i}$.

4.3.5 Using replicates to ensure optimal results

K-means clustering was then performed ten times for each $k = [1, 2, \ldots, 14, 15]$ with new, randomly selected initial cluster centroid positions each time in an attempt to ensure that the resulting clustering result would be optimal for that k. The optimal clustering result was chosen for each k by computing the total within-cluster sums of point-to-centroid Euclidean distances.

$$\sum_{i=1}^{k} \sum\nolimits_{e \in c_i} |e - \mu_i| \tag{4.6}$$

for each iteration, where e is an element within cluster c_i and μ_i is the mean of cluster c_i, and choosing the result for which it was smallest.

4.3.6 Model selection using the Calinski-Harabasz criterion

The Calinski-Harabasz criterion was then used to select the optimal number of clusters, or k, for each quantitative SEM-EDS dataset. The Calinski-Harabasz criterion for a given k in which there are N observations (here, the total number of pixels in the mapped region) is defined as

$$\frac{N-k}{k-1}\frac{\sum_{i=1}^{k} n_i|\mu_i-\mu|^2}{\sum_{i=1}^{k}\sum_{e\in c_i}|e-\mu_i|^2} \tag{4.7}$$

where n_i is the number of datapoints in cluster c_i of k clusters, and μ is the overall mean of the data for the entire mapped area. The Calinski-Harabasz criterion was computed using the optimal clustering result found for each k. The numerator of the right-hand term of Eqn. 4.7 corresponds to the overall between-cluster variance, and the denominator corresponds to the within-cluster variance. The "best" clustering result is one that maximizes the between-cluster variance and minimizes the within-cluster variance. Therefore, the k for which the Calinski-Harabasz criterion was largest was chosen as the optimal clustering result for that sample region. Built-in MATLAB functions were used to carry out k-means clustering and compute the Calinski-Harabasz criterion the optimal result found for each k. The replicates for each k were run concurrently on a parallel pool of workers to reduce the total runtime of the algorithm. Custom MATLAB scripts were written to generate the ternary diagrams, normalize the data, interpret the k-means clustering results, and generate the phase maps.

4.3.7 Example: Phase mapping of the cross-section of ancient Roman mortar

The above methodology was applied to the polished cross-section of ancient Roman mortar studied in Fig. 4-3 and Fig. 4-4. The BS-SEM image shown in Fig. 4-8A shows the distribution of binder, aggregate, and pore space, but compositional differences are not as obvious as they are in the normalized SEM-EDS element map in Fig. 4-8B. In Fig. 4-8B, one can see that there are clear differences in the types of aggregate; some grains (blue) that are richer in aluminum can be distinguished from those that are far richer in silicon (green).

The ternary diagram that was presented in Fig. 4-4 is shown once again in Fig. 4-

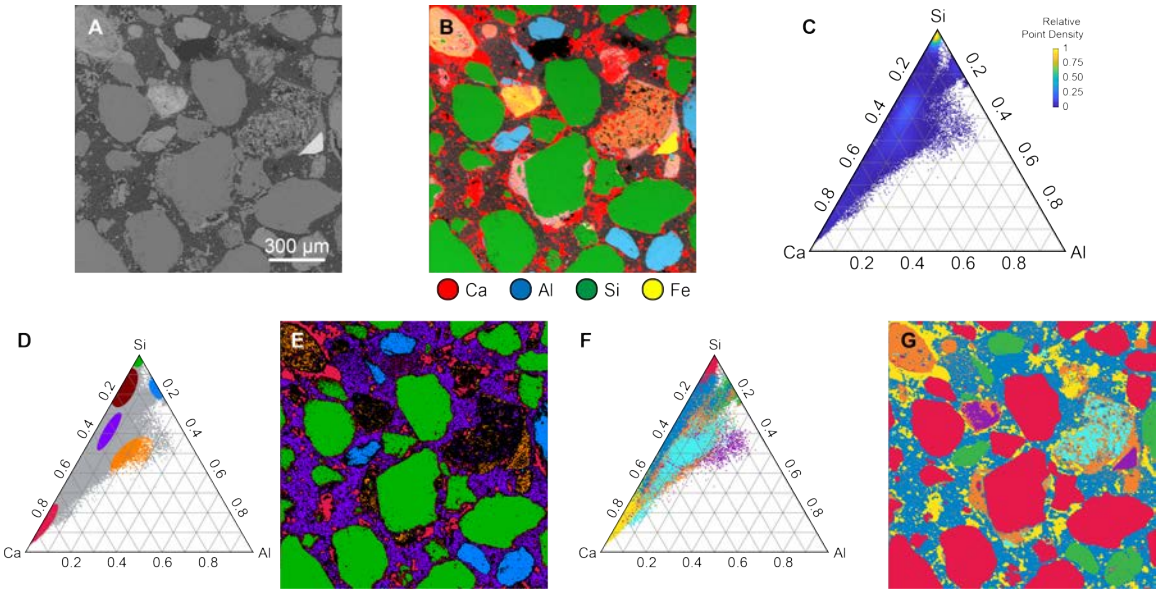

Figure 4-8: **K-means clustering and model selection for the cross-section of a sample of ancient Roman mortar from the Privernum archaeological area. A:** BS-SEM image, **B:** normalized SEM-EDS element map, **C:** ternary density plot of quantitative SEM-EDS data. **D:** Ternary plot and **E:** phase map for selected regions of the ternary plot. **F:** Ternary plot and **G:** phase map for optimal number of phases determined via k-means clustering and the Calinski-Harabasz criterion.

8D. Here, we see that different regions of the ternary plot correspond to unique phases. The application of the k-means algorithm and model selection step that were described in the previous section yield the clustering result shown in Fig. 4-8F and Fig. 4-8G, which show the Ca-Si-Al ratios and distributions of the seven identified clusters, respectively. In Fig. 4-8G, the silicon-rich aggregate (most likely quartz) is shown in red and the aluminosilicate aggregate grains are shown in green. It is also seen that there are two major types of binding phase present: a high-Ca component shown in yellow and a lower-Ca component shown in dark blue. The iron-rich grains that can be seen in the normalized SEM-EDS map in Fig. 4-8B are shown as the purple phase in Fig. 4-8F and Fig. 4-8G. Due to their positions on the ternary diagrams, the orange and light blue phases likely correspond to calcium-rich aluminosilicates [32].

The clustering procedure described and illustrated in this chapter has proven to be generally applicable. When used with the SEM-EDS data for kidney stones, they showed distributions of phases that were consistent with clinical IR data. More details

about this study can be found in Appendix B.

4.4 Identification of pore space via segmentation of BS-SEM images

If the empty space in a porous composite is filled with epoxy or another mounting medium, clustering the SEM-EDS data may show the distribution of the pore space, especially if the mounting medium is distinct is chemical composition from the composite itself. For example, epoxy is usually rich in chlorine due to the presence of epichlorohydrin [C_3H_5ClO], and cementitious materials tend to contain only trace amounts of chlorine if there is any at all.

In some cases, however, clustering the SEM-EDS data does not show the distribution of pore space. For example, for the Roman mortar sample in Fig. 4-8, pore space can be visually identified near in the top of the mapped region. In Fig. 4-8A, it can be identified as a region of low greyscale intensity, and in Fig. 4-8B it can be seen in black. However, in the phase map that that was generated using the clustering procedure in Fig. 4-8G, the pore space was assigned to the dark blue component of the binding phase, likely due to the elemental ratios in these regions being similar to those of the other pixels in the dark blue phase. In these cases such as these, another technique needs to be implemented to identify the pore space.

When composites are imaged using BS-SEM, the empty space tends to be visible by eye, because the pixel brightness in a BS-SEM image is directly related to the heaviness of the atoms present in the same in those regions. Therefore, empty spaces show up in the images as regions of very low greyscale intensity (Fig. 4-9) that can isolated using various image segmentation techniques. In this work, the pixels of the BS-SEM images were partitioned using the built-in k-means clustering based image segmentation MATLAB function, `imsegkmeans`.

Prior to segmenting a BS-SEM image, it may be necessary to first apply a flat-field correction. Depending on the imaging parameters using during collection of

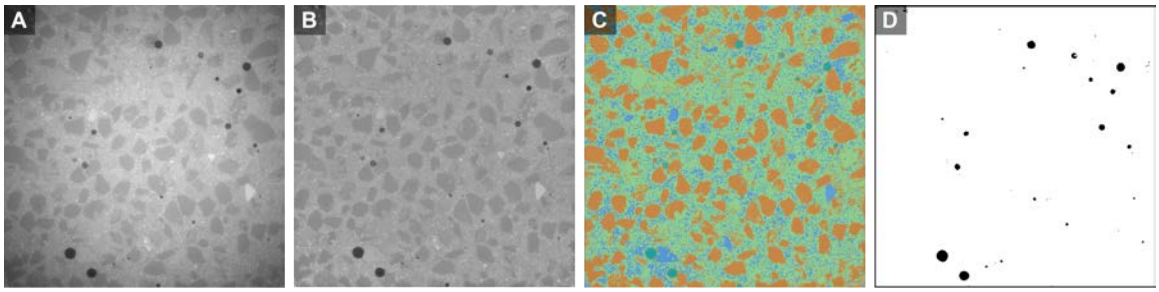

Figure 4-9: **Procedure for mapping void space using BS-SEM images.**

a BS-SEM image or as a result of the view field being too large, there may be a vignette or shadowing effect seen around the perimeter the image. The MATLAB built-in function `imflatfield` was used to correct the vignetting seen in Fig. 4-9A using Gaussian smoothing with a user-defined standard deviation. A standard deviation of 20 was used to correct the vignetting in Fig. 4-9. The corrected BS-SEM image (Fig. 4-9B) was then used as the input for the image segmentation. For this particular BS-SEM image, segmenting the pixels into four clusters yielded the result seen in Fig. 4-9C. The cluster corresponding to the pore space is shown separately in Fig. 4-9D.

4.5 Summary

This chapter demonstrated the use of a series of computational tools that were applied in conjunction with the high-throughput chemical characterization techniques that were presented in Chapter 3. First, the homography transformation was used to coordinate 3D surface chemical data that were collected using complementary characterization techniques, enabling the pixel to pixel comparison of quantitative SEM-EDS element data to the corresponding Raman spectra. Next, ternary diagrams were used as tools for visualizing the distinct phases present in the heterogeneous systems of ancient and modern cementitious materials. It was shown that particular regions of the ternary diagrams corresponded to unique phases present in the composites, which was illustrated by backplotting particular regions of data points onto the original mapped regions. Given this observation, unsupervised learning in the form of

k-means clustering was used to partition the SEM-EDS element maps into chemically distinct phases, which were then identified with the aid of the corresponding ternary plots. The most likely number of phases present was identified using the Calinski-Harabasz method. Finally, a procedure for isolating the pore space in the composite was presented. The efficacy of the approaches presented in this chapter suggests that they would likely be successful when applied to composites of unknown composition in general.

Chapter 5

The Temple Scroll: Reconstructing an ancient manufacturing process

This chapter illustrates that the tools presented in Chapters 3 and 4 may be used to study materials in general—not only ancient Roman cementitious materials. Here, they have been applied to the study of another kind of complex composite from the ancient world: parchments. The remarkably preserved 2000-year-old Dead Sea Scrolls, ancient texts of invaluable historical significance, were discovered in the mid-20th century in the caves of the Judean desert. The texts were mainly written on parchment and exhibit vast diversity in their states of preservation. One particular scroll, the 8-m-long Temple Scroll is especially notable because of its exceptional thinness and bright ivory color. The parchment has a layered structure, consisting of a collagenous base material and an atypical inorganic overlayer. In the study presented in this section [68], the chemistry of the inorganic layer was analyzed using X-ray and Raman spectroscopies and a variety of evaporitic sulfate salts were discovered. The chemistries of various Dead Sea Scrolls found in three different caves in Qumran were then compared to the Temple Scroll using ternary diagrams to determine which scrolls may have been produced using similar production technologies. The results of this work indicate a unique ancient production technology in which the parchment was modified through the addition of the inorganic layer as a writing surface. Due to the hygroscopic nature of the minerals identified, the authors of this work

have concluded that the identification of these minerals is critical in the selection of environmental conditions that are necessary for the preservation of these invaluable historical documents.

5.1 The Dead Sea Scrolls: Background

Ancient texts, known collectively as the Dead Sea Scrolls (DSS), were discovered in the middle of the last century and are certainly some of the most treasured objects of cultural heritage. The DSS were miraculously preserved in the natural limestone and man-made marl caves of the Judean desert, and the main collections are held in the Israel Antiquity Authority, the Shrine of the Book, and Jordan. Apart from having inherent textual value, the DSS also carry historical information related to the materials processing technologies that were used to produce them. A detailed understanding of these ancient technologies could be used for forgery identification purposes and for the development of modern antiquity-inspired, collagen-based materials [69].

Most of the DSS were written on animal skin-based material that can be roughly described as a hybrid of parchment and leather. Similar to medieval practices, production of the writing surfaces from the skins of cattle, sheep, and goats included four main steps: de-hairing, thinning, drying under tension, and finishing. However, in contrast to medieval and modern techniques, the first step (i.e., de-hairing) was conducted without a lime solution, which led to a higher content of fats in the processed skins [70]. The de-hairing in the case of DSS involved an enzymatic treatment, which was likely carried out by application of fermented grains. In addition, vegetable tannins were occasionally applied to the surface during the final stage of skin processing [71, 72].

This general description of the DSS production process, however, lacks the specific characteristics of the materials used for the drying and finishing steps. It is known that in the case of Middle Age parchments, chalk and powdered pumice were applied to the flesh side to aid in the cleaning and drying of the de-haired skin [73], but this was not the case for the DSS. It is also known that aluminum sulfate salts, known as

alum [$MAl(SO_4)_2 \cdot 12\,H_2O$, M = Na, K, NH_4], have been used throughout antiquity for tawing skins to produce soft, white leather of excellent quality [74]. In the case of extremely thin parchments from the DSS collection, which served as a writing surface for phylacteries, the production involved splitting of the de-haired skin into two parts, the grain split (carrying a follicle pattern) and the flesh split [75]. It appears, however, that the practice of manually splitting skins did not exist in the Middle Ages, when lime was universally used as the de-hairing agent.

In a recent study, an integrated methodology for determining the original and acquired properties of the DSS has been developed [76]. Using a combination of X-ray, Fourier transform infrared (FT-IR), and Raman techniques, it was possible to identify the organic and inorganic phases present in the scrolls. It was shown that the organic (parchment) and inorganic (sediments from the caves) phases of the ancient fragments were not completely intermixed and could be spatially resolved. In most of the cases studied, the mineral deposits that were detected on the surface of the scrolls could be linked to those of the caves. In a smaller number of fragments, however, the surface was coated with a thin mineral layer that presumably originated from the parchment production process. These investigations led to the conclusion that the skin-based writing surfaces of the DSS could be roughly grouped into three different categories: leather parchments; parchments of various shades of brown, which were tanned using the "Eastern" practice; and light-colored untanned parchments, which were produced using the "Western" practice [77]. The similarities of the second and third of these categories of the DSS to Babylonian documents from the 5th century BCE and early Greek parchments led to the hypothesis that Eastern and Western parchment production technologies coexisted at the time of the production of the DSS.

Among all the DSS, there is one particular document, the Temple Scroll (TS) ($11QT^a$) from the Israel Museum's collection, which is especially notable because of its physical appearance (Fig. 5-1, A and B). The TS is written on a bright ivory-colored parchment that measures 8.148 m in length, and its thickness hardly exceeds 0.1 mm. Its recovery history is more complicated than that of other scrolls in the

collection. Allegedly, a group of Bedouins found it wrapped in cloth in a jar in 1956 in Cave 11 of Qumran and then sold it to an antiquities dealer who replaced the original encasement with cellophane and then transferred it from the jar into a shoebox that he hid under the floor in his home. When scholars finally accessed the scroll some 11 years later, it was severely damaged by moisture, particularly on its outer sheets and upper edge [78]. Previous studies have confirmed that the TS was retrieved from Cave 11 [79].

Immediately after its purchase by the State of Israel, the unrolling of the tightly wound scroll was conducted in accordance with the Plenderleith method [80]. This involved the humidification of the scroll up to 100% relative humidity with subsequent short freezing to arrest the gelatinization process. Thus, the first visual description of the scroll by Y. Yadin depicted its state after unrolling and the reassembly of previously detached fragments. Yadin believed that the nonuniform state of preservation, which varied greatly from sheet to sheet, resulted from a nonuniform treatment of the parchment in antiquity [78]. Furthermore, some of the text was found only as a mirror image imprint on the verso of the columns with which it was in contact, leaving blank surfaces behind. This type of text transfer occurred indiscriminately throughout the scroll and did not seem to be correlated with the state of degradation [1]. X-ray diffraction and FT-IR studies of the TS parchment collagen showed high degrees of degradation juxtaposed with apparently good states of preservation [81, 82]. More recently, through an investigation of individual collagen fibers within the TS fragments using polarized μRaman spectroscopy, well-preserved collagen was detected beneath a detached outer inorganic layer [83].

In this work, the chemistry of the inorganic layer of an unprepared fragment of the TS was studied using μ-X-ray fluorescence (μXRF), energy-dispersive X-ray spectroscopy (EDS), and Raman spectroscopy. The results demonstrate the presence of a complex mixture of evaporitic salts as the major component of the inorganic layer on which the text was written. The mineral phases that were detected on the TS are typical for nonmarine evaporitic mineral deposits, and the findings of this work point to a specific technique that was used to produce the TS.

5.2 Prior characterization of Temple Scroll fragment and particulates

The data presented in this section was primarily collected by Dr. Roman Schuetz of the Israel Institute of Technology and is necessary for providing context for the remainder of this chapter.

Whereas most of the DSS are quite dark in color, a small number among them, including the TS, are light colored [84]. In addition to its bright appearance, the TS exhibits a multilayered structure with the text written on the ivory-colored inorganic layer that covers the flesh side of the skin. The reverse side of the TS reveals the hair side of the processed skin, which is more yellow in appearance. The hair follicle pattern visible on the reverse side of the scroll (Fig. 5-1A) indicates that the text was at least partially written on the flesh side of the parchment. On the text side (Fig. 5-1C, left), regions of the inorganic layer are often missing, exposing the yellowish collagenous layer beneath. Similarly, there are regions where the detached inorganic layer is preserved. The patches of the detached text-containing inorganic layer that were found stuck to the reverse side of the scroll were an unexpected result in the study of the TS [78]. The uninscribed fragment of the TS presented here (Fig. 5-1) includes regions where the yellowish organic layer is missing, and the resulting differences in thickness throughout the sample can be seen in the light transmittance image in Fig. 5-1D. The multilayered structure is also clearly visible in the enlarged optical micrograph in Fig. 5-1E corresponding to the region of interest (ROI) in Fig. 5-1C (left). A schematic representation of the fragment stratigraphy can be found in Fig. 5-2.

5.2.1 µXRF and EDS study of the Temple Scroll

The TS is a striking heterogeneous material (Fig. 5-3A), so to better characterize this complexity, µXRF and EDS analyses were conducted on the both sides of the TS fragment to investigate its elemental composition. The µXRF sum spectra of two

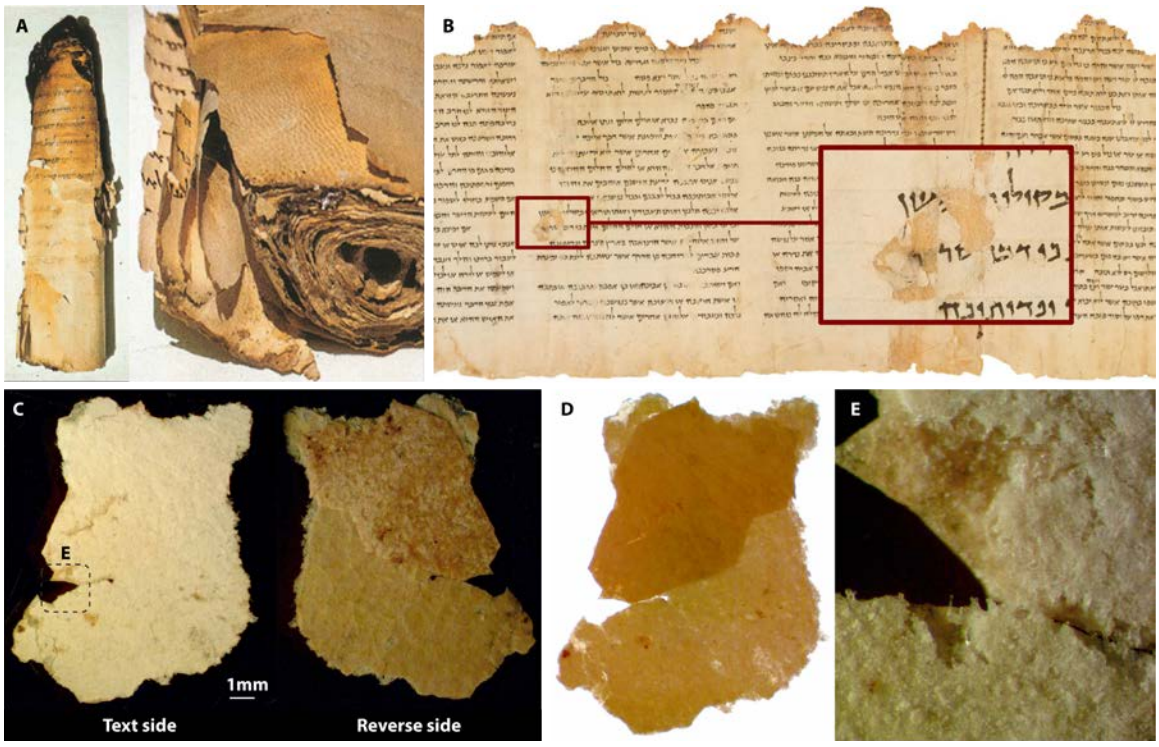

Figure 5-1: **Light microscopy of the TS, showing its layered structure from the macroscale to the microscale.** **A**: Photographs of the TS showing damage to the upper part of the scroll (left). The reverse side of the preserved section (right) shows the follicle pattern of the hairs removed from the skin, which indicated that the text is written on the flesh side of the treated skin [1]. [**A**: Courtesy of the Estate of Yigael Yadin.] **B**: Column 54 of the unrolled TS [2]. The enlarged inclusion (inset) shows that some parts of the bright, text-carrying inorganic layer have been detached. [**B**: Photo credit: The Israel Museum, Jerusalem.] **C**: Fragment of TS showing inorganic layer on text side (left) and reverse side (right). The organic layer has partially detached, revealing the inner surface of the inorganic layer. **D**: The same fragment in light transmittance from the back differentiating the thinner lower part, where the detachment has occurred from the thicker upper part. **E**: Enlarged optical micrograph of the boxed region in **C**.

ROIs (Fig. 5-3B) show a complex inorganic layer composition with major elements that include Na, Mg, Al, Si, P, S, Cl, K, Ca, Mn, Fe, and Br. The K-line μXRF element distribution maps of some of these elements, plotted in Fig. 5-3C, show that the major elements Na, Ca, S, Mg, Al, Cl, and Si are distributed throughout the entire fragment. Al appears to be fairly evenly distributed throughout the fragment, but this map may be unreliable due to the close proximity of the K-line of Al to the L-line of Br. The K and Fe maps are likely associated with contaminants, rather than

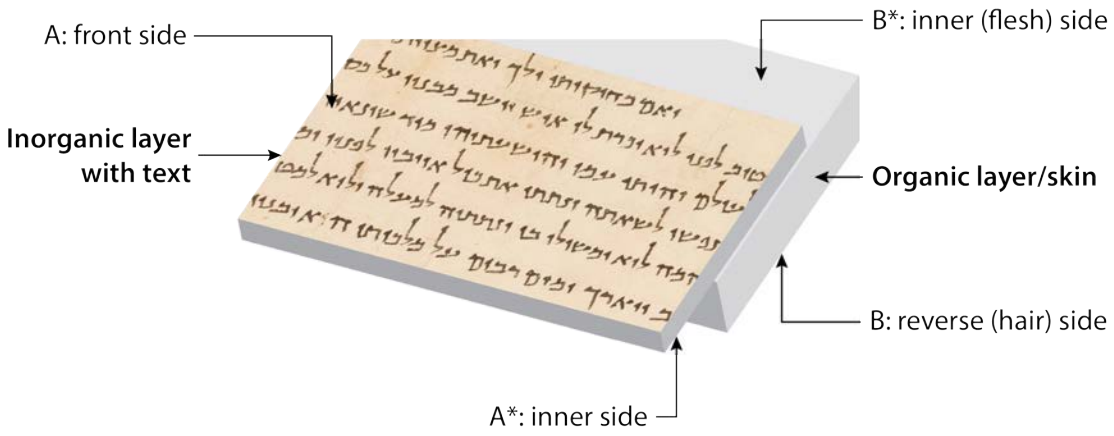

Figure 5-2: **Schematic showing the stratigraphy of the TS fragment, 11QT^a.**

with intentional additives during the TS production process.

Although certain elements, such as Mn, Fe, and Br, appear to be more concentrated in the thicker regions of the fragment where the organic layer was not detached, it should be noted that this could be an artefact due to sample thickness. Lighter elements would only be detected near the surface due to the absorption of their lower energy characteristic X-rays within the sample, whereas higher energy X-rays from heavier elements would be detected throughout the entire thickness of the fragment.

The µXRF element maps may be studied in conjunction with the distribution of cracks and small detachments throughout the inorganic layer to improve the understanding of the phases associated with the different elements. Na and Cl show a similar distribution throughout the entire measured area i.e. the regions of the fragment that still have the organic layer attached have a greater Na and Cl concentration. In contrast to Na's more uniform coverage of the sample, the Cl distribution map does not follow the pattern of cracks and small detachments in the inorganic layer. The Na-Cl distribution correlation maps may thus indicate the presence of sodium chloride (NaCl) only inside the organic skin layer, which is a known remnant from the Dead Sea Scroll skin/parchment processing process [85, 74, 86].

To quantify the elements of interest on the surface of the fragment, SEM-EDS was conducted on the ROI illustrated by the dashed box on the multi-color EDS

map in Fig. 5-3A. SEM-EDS allows for high lateral spatial resolution due to the comparatively smaller depth penetration of the electrons. Low-vacuum SEM was used for this purpose, since it minimizes vacuum-induced damage and allows for the elemental mapping of non-coated (non-conductive) samples. The EDS element maps (Fig. 5-3D) show particles in the inorganic layer ROI that predominantly contain sodium, sulfur, and calcium. Silicon was also detected in the inorganic layer, but not in the Na-S-Ca particles found on the surface of the inorganic layer, and Al and Cl were detected at higher concentrations between the particles and in the organic material. The Na, S, and Ca element maps (inset in Fig. 5-3B) show clear correlation between these three elements and arrows indicate the particles in which sodium and sulfur, but little calcium, were observed.

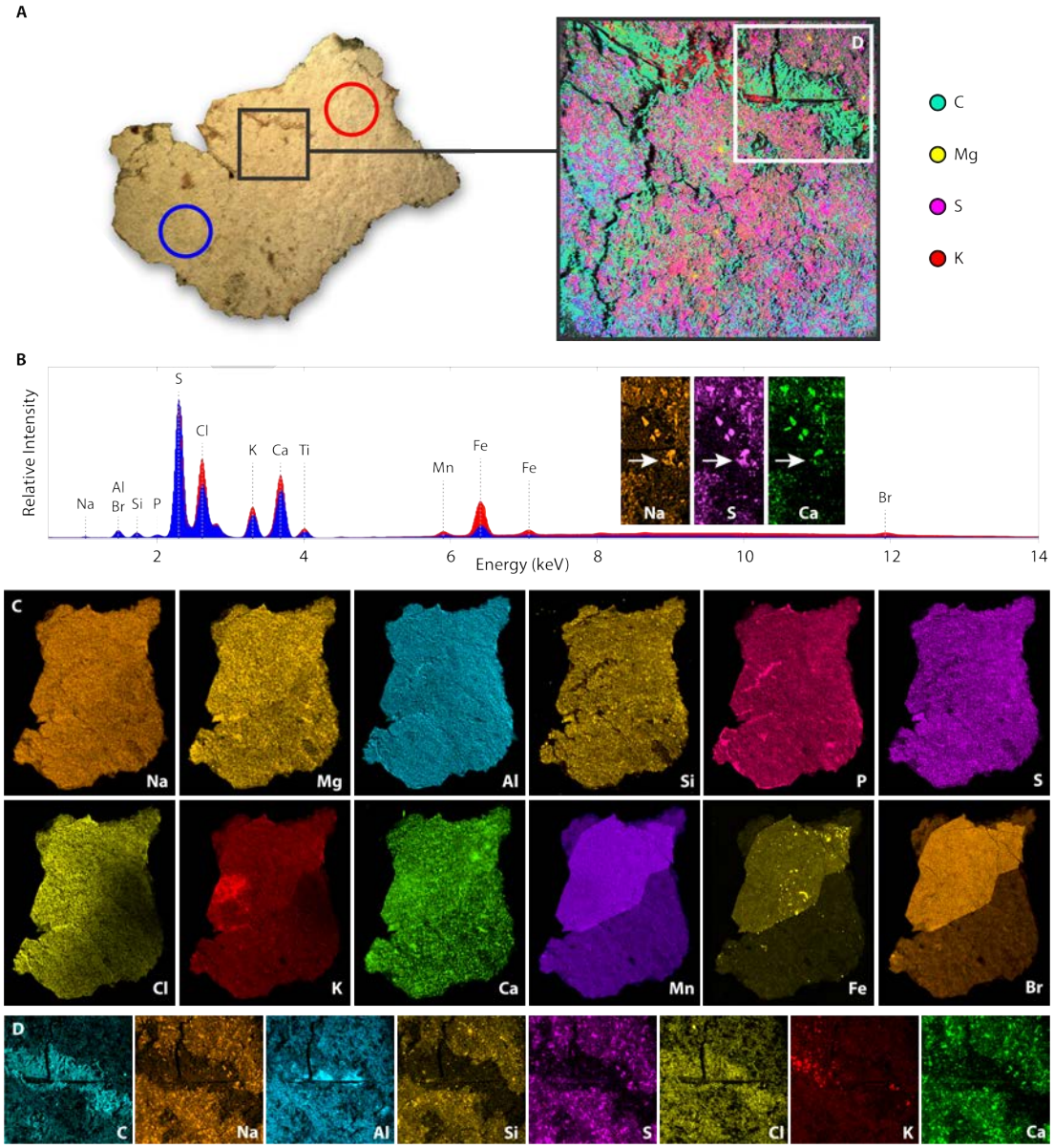

Figure 5-3: **Large-scale µXRF and EDS characterization of the text-containing side of the TS. A**: The text-containing surface of the TS (optical image, left) is extremely heterogeneous, as demonstrated in the large-area multielement EDS map (right). **B**: Large-area µXRF elemental averages demonstrate clear compositional differences between the blue circled region, which largely encompasses the inorganic overlayer, and the red circled region, which includes both the mineral overlayer and the underlying collagenous base material. **C**: µXRF elemental distribution maps of the 12 most evident relevant elements. **D**: EDS elemental maps of the ROI area indicated on the multielement EDS map in **A**. From these EDS measurements and those shown in the small Na, S, and Ca elemental maps **B**, inset] of cropped regions of **D**, we observe some elemental clusters where the particles (denoted by the arrows) contain Na and S but very little Ca. Other Ca-containing particles without Na and/or S were also identified.

5.2.2 Raman spectroscopy study of the Temple Scroll

From the µXRF and EDS studies, it is clear that the inorganic layer contains particles rich in sodium, calcium, and sulfur, along with other independent mineral phases. However, since the chemical bonding and phase characterization cannot be fully realized using µXRF and EDS, Raman spectroscopic investigations were also performed (Fig. 5-4). In order to reduce the background fluorescence typically observed in Raman spectra of the DSS, low-energy excitation wavelengths were used. First, FT-Raman operating at an excitation wavelength of 1064 nm was used to collect average spectra from the TS fragment from very large spot sizes (400 µm in diameter) (Fig. 5-4A). Both spectra show three main components: a sulfate double peak at 987 cm^{-1} and 1003 cm^{-1}, a nitrate peak at 1044 cm^{-1}, and the proteinaceous contribution typical of collagen or gelatin.

The spatial resolution of FT-Raman did not allow for the differentiation of the inorganic particles and the collagen fibers, so confocal Raman spectroscopy measurements were performed using a near-infrared 785 nm excitation laser on the same fragment. Spectra for the collagen fibers (spectrum I) and inorganic particles (spectra II and III) are reported in Fig. 5-4B. The collagen fiber spectrum includes the characteristic nitrate peak at 1043 cm^{-1}, which can be assigned to the ν1 vibration of the NO_3^- ion in NH_4NO_3 (20).

Spectrum II, which was collected on a Na-S-Ca-containing particle of the inorganic layer, is characterized by two peaks in the sulfate SO_4^{2-} region (987 cm^{-1} and 1007 cm^{-1}). The intensity ratio of these two peaks varied from particle to particle throughout the TS fragment (data not shown). The variability in the Na-S-Ca particles suggests that the particles are comprised of mixtures of various sulfate-containing minerals in different proportions. Comparison of the spectral features of these particles with spectra of reference samples of inorganic salts containing SO_4^{2-} ions, namely glauberite [$Na_2Ca(SO_4)_2$], gypsum [$CaSO_4 \cdot 2\,H_2O$], and thénardite [Na_2SO_4] did not yield satisfactory matches (Fig. 5-5). Raman peaks of the air-dried, synthetic Na_2SO_4 and $CaSO_4$ aqueous mixture, which are located around 450 cm^{-1} and 630 cm^{-1} also

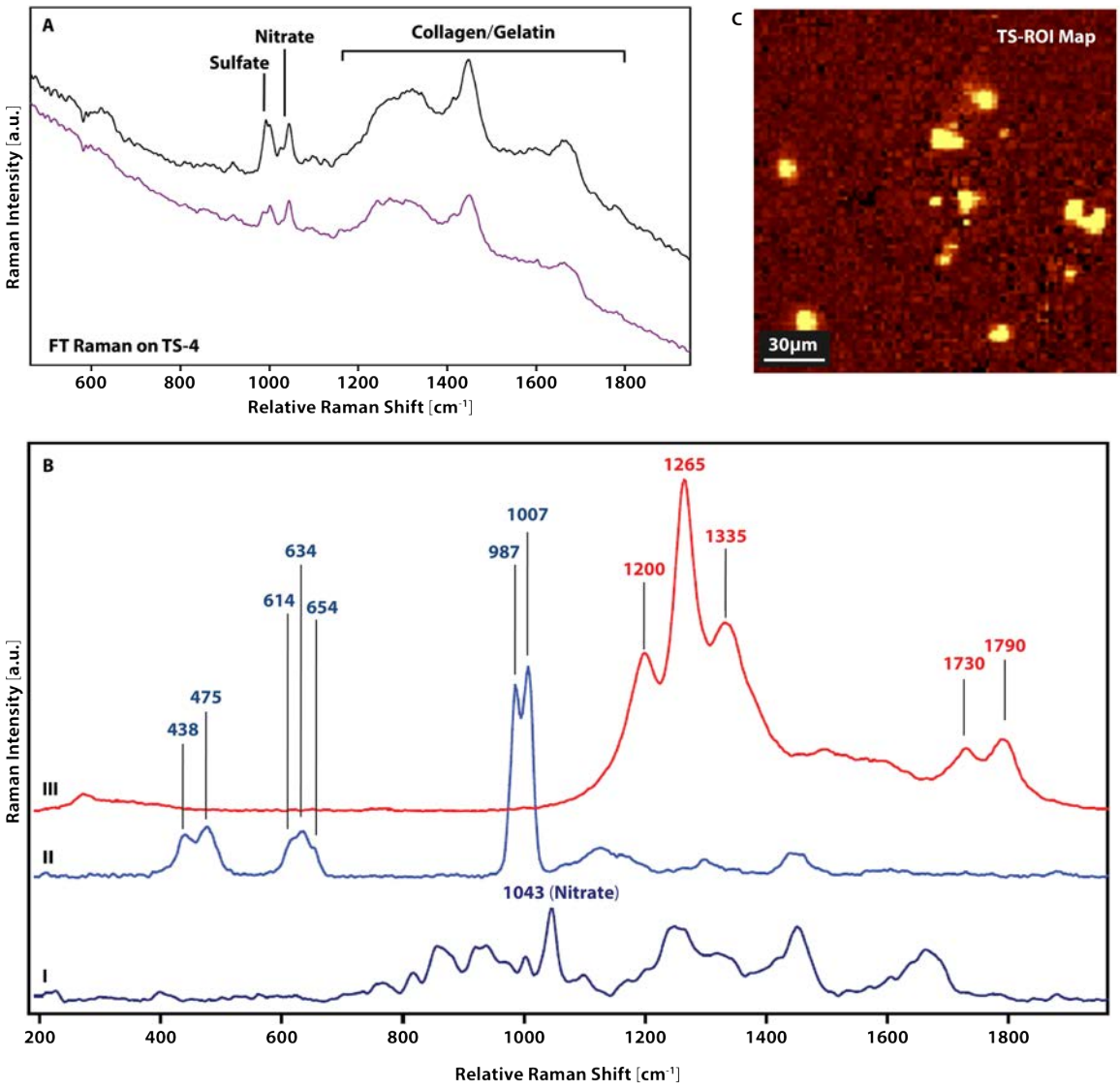

Figure 5-4: **Raman spectra for the composite materials of the TS. A**: FT-Raman spectra of two regions of the text side of a TS fragment. a.u., arbitrary units. **B**: Confocal µRaman at 785 nm spectra of the TS composites. I: Collagen spectrum; collagen spectra inside the TS always contain a nitrate peak at 1043 cm^1. II: Sulfate spectrum of particles with Na, S, and Ca constituents. III: Unidentified particles distributed throughout the inorganic surface layer, which yielded very resonant Raman signals with 785 nm laser excitation. **C**: Distribution map of the particles on the surface of the inorganic layer, which were resonant for Raman excitation at 785 nm.

differ from the TS Spectrum II (Fig. 5-4B). Interestingly, however, drying this synthetic mixture by fast evaporation at 250°C resulted in different evaporate particles, which in some cases yielded Raman spectra similar to those of the TS in the sulfate regions (Fig. 5-5).

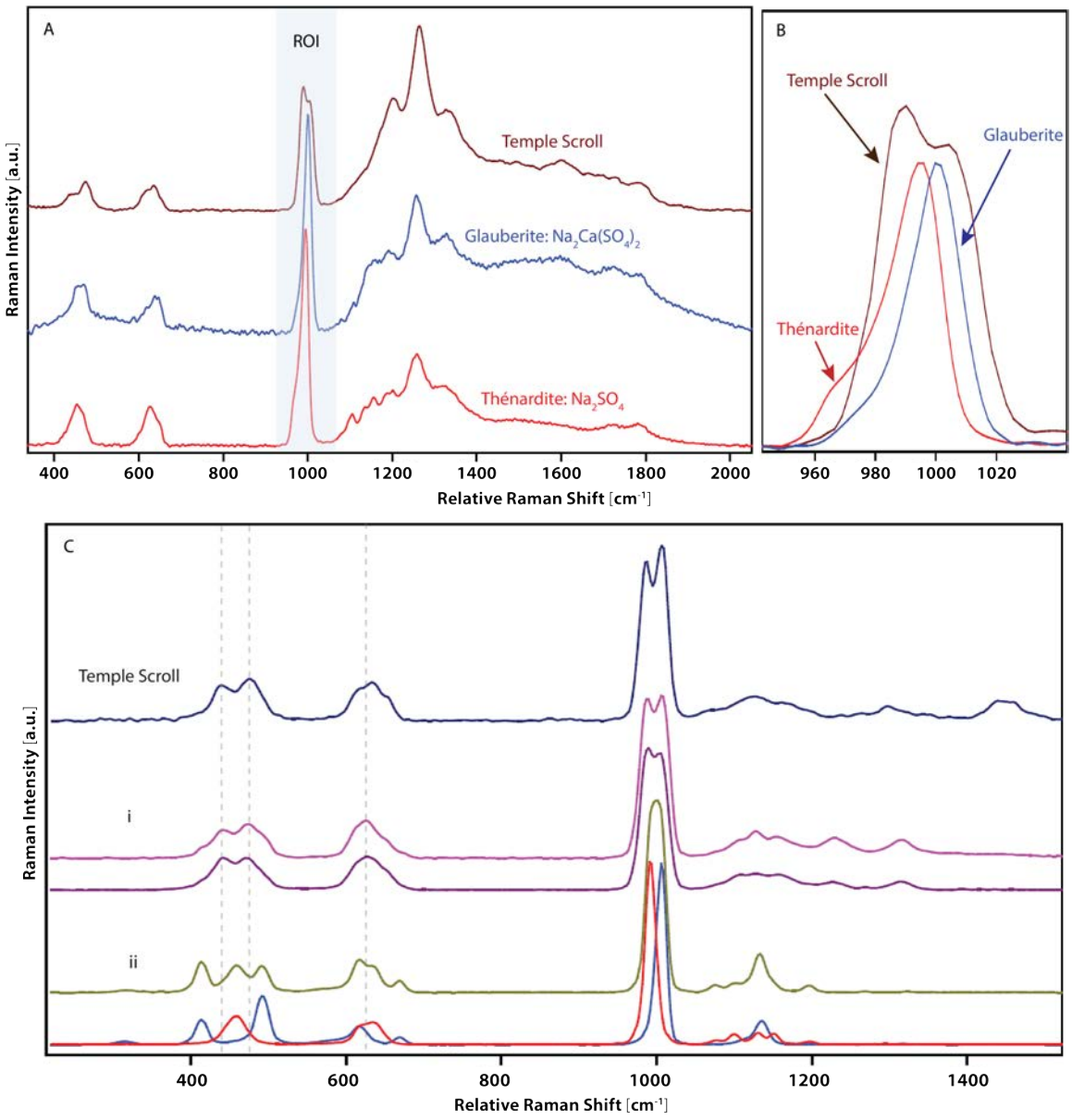

Figure 5-5: **Raman (785 nm) spectra of TS inorganics and related sulfate salts.**

Spectrum III in Fig. 5-4 is associated with very small particles in the inorganic layer that are about 5 to 15 µm in diameter (distribution shown in Fig. 5-4C). These particles showed very intense Raman scattering using an excitation wavelength of 785 nm. The characteristic triplet spectral signature at 1200 cm^{-1}, 1265 cm^{-1}, and 1335 cm^{-1} reflects vibrational units of the type "Na_2X." This triplet is characteristic of sulfates that contain Na and is often detected in the minerals thénardite and

glauberite (Fig. 5-8).

5.3 SEM-EDS ternary diagram study of the Temple Scroll and Cave 4 fragments

A multi-detector EDS system was also used to collect large area elemental maps of ROIs on both the text and the reverse sides of the TS fragment (Fig. 5-6). Backscattered SEM imaging of the brighter text containing side (Fig. 5-6B) and the darker reverse side (Fig. 5-6C) revealed an extremely heterogeneous composition. In the vicinity of a large crack on the text-containing side (Fig. 5-6B), for example, clear differences in electron density could be seen between the inorganic overlayer and the underlying collagenous material.

The major elements present in the fragment (Ca, Cl, Fe, K, Mg, Na, P, S, Si, C, and O) were then quantified by atomic percent. It should be noted that the results from the quantification of C and O are unreliable due to the low energies of their characteristic X-rays and the ambient chamber concentrations of O under the low vacuum conditions under which the data were collected, and as such, these results were excluded from any further analysis. The ratios of the three elements of interest from the aforementioned µXRF, EDS, and Raman studies of the particles within the inorganic layer (i.e., Na, Ca, and S) at each point of the 512px by 512px measured area are shown on ternary axes in Fig. 5-6. Ternary density plots (Fig. 5-6A and Fig. 5-6D) show the relative density of points on the diagrams as described by color bar to the right of Fig. 5-6D. Both ternary plots show that the ratios of calcium to sodium to sulfur at each pixel of the measured areas on both the text side and the reverse side lie between the theoretical ternary diagram locations for glauberite (red dot, measured chemistry: $Na_{1.90}Ca_{1.15}(S_{0.99}O_4)_2$ [87]) and thénardite (purple dot, measured chemistry: Na_2SO_4).

The quantified EDS data were then clustered with respect to a set of the major elements (excluding C and O) using the fuzzy c-means clustering algorithm (Fuzzy

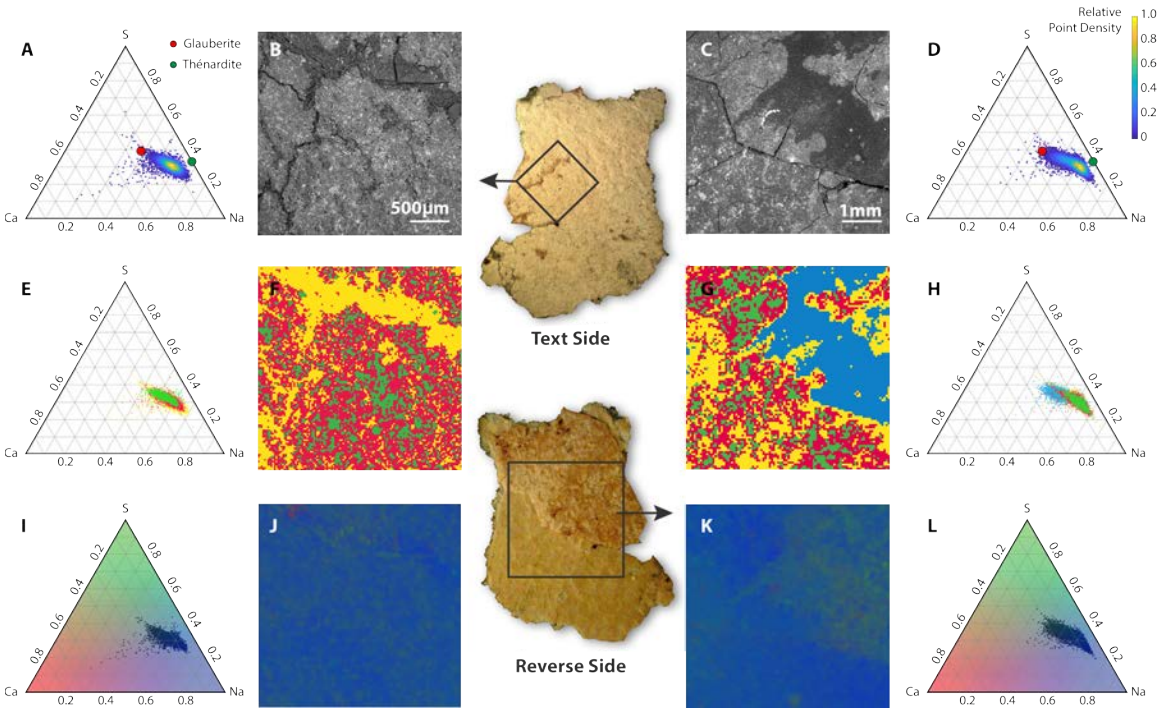

Figure 5-6: **BS-SEM images, ternary diagrams, and phase maps for the text and reverse sides of the TS. A**: Ternary density plot showing Ca-Na-S ratios for a region of the text side, indicated by the box on the optical image (center, top). **B**: BS-SEM image of a cracked region from the text-containing side of the TS, showing both the inorganic overlayer and the underlying collagenous material. **C**: BS-SEM image of a region of the reverse side and **D**: ternary diagram showing the corresponding distribution of Ca-Na-S ratios. Ternary diagrams and phase maps showing the distribution of clustered EDS data for (**E** and **F**) the text side and (**G** and **H**) the reverse side. Ternary diagrams showing the distribution of different Na-S-Ca ratios, colored as RGB combination of the colors at the axes for (**I** and **J**) the text side and (**K** and **L**) the reverse side.

Logic Toolbox, MATLAB R2018a) to visualize the distribution of different phases present on the text and reverse sides of the TS fragment. These results were then used to determine the most likely division of the 5122 data points of each dataset into a predefined number of clusters. The data for the text side were divided into 3 clusters, and the data for the reverse side were divided into 4. The clustering results are reported as both overlapping clusters on ternary axes (Fig. 5-6E and Fig. 5-6H), and as distributions maps (Fig. 5-6F and Fig. 5-6G). The clustering results show the distribution of the dark, organic material on the reverse side of the TS (Fig. 5-6K, blue), and where the cracks in the inorganic later on the text side expose the collagen

layer beneath it (Fig. 5-6J, yellow). Note that the colors assigned to the clusters for the text side do not correspond to colors assigned to the clusters on the reverse side.

To show the distribution of Na-Ca-S ratios, the points on the ternary diagrams were colored as a mixture of three colors (RGB) according to their ternary positions (Fig. 5-6I and Fig. 5-6L), in which the top vertex (sulfur) is green, the left vertex (calcium) is red, and the right vertex (sodium) is blue. The same colors were then used to identify the corresponding pixels in the measured area (Fig. 5-6J and Fig. 5-6K). The resulting blue-green distribution maps demonstrate a high sodium, low calcium, and moderate sulfur content throughout both the text side and the reverse side of the TS.

The same methodology was also used to show the distribution of Na-Ca-S for another region of the text side of the TS fragment and several regions of the front and reverse sides of three scroll fragments obtained from the 4Q cave in Qumran (R-4Q1, R-4Q2, and R-4Q11; Reed's collection) in Fig. 5-7. For each ROI, the BS-SEM image is shown on the left, and the corresponding ternary density plot (relative point density illustrated according to color bar, Fig. 5-7, bottom left-center) to its right. The distribution of Na-Ca-S ratios throughout the ROI are shown to the right of the ternary density plots (according to the colored ternary diagram at the bottom left of Fig. 5-7).

Significantly, only the ternary diagrams and ratio distribution maps for R-4Q1 show a noteworthy overlap with those of the TS. Specifically, the results show ratios for R-4Q1 that correspond with the theoretical Na-Ca-S ratio of glauberite. Raman measurements collected at an excitation wavelength of 785 nm for R-4Q1 show the presence of sodium sulfate, calcium sulfate, calcite, and, in addition, the peaks associated with the resonant "Na_2X" particles, which corroborate the EDS/ternary diagram results (Fig. 5-8). Interestingly, the nitrate peak was not present in the Raman data for the R-4Q1 collagen fibers.

The similarities between the R-4Q1 scroll and the TS are compelling, in that they suggest a potential overlap in their ancient preparation methods, which seem to involve the use of evaporitic salts. Two other scrolls obtained from the same Cave 4Q

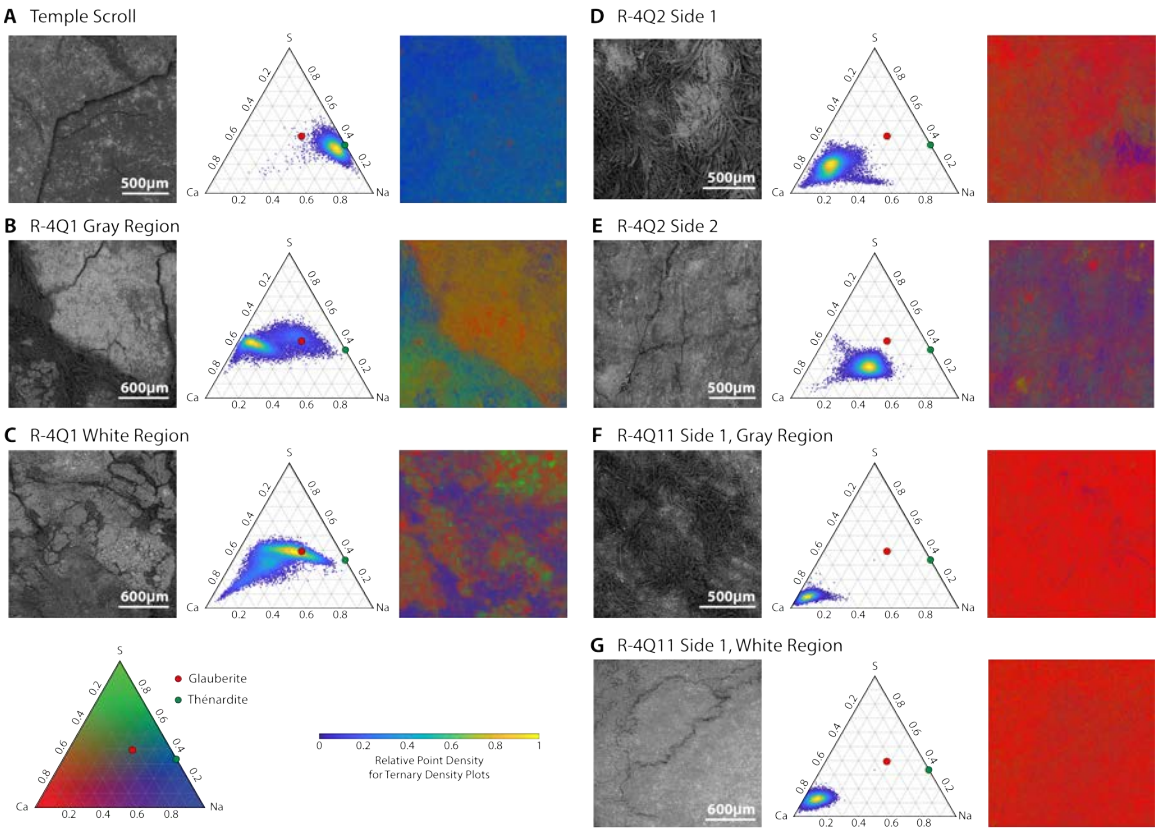

Figure 5-7: **BS-SEM images, ternary density plots, and Na-S-Ca ratio distribution maps for a subregion of the reverse side of the TS and three additional scrolls obtained from the 4Q cave.** Each panel contains the BS-SEM image of the measured regions (left). EDS phase maps were obtained by coloring each pixel according to the ratio of calcium to sodium to sulfur, as indicated by the colored ternary diagram at the bottom left of the figure (center) and ternary density plots, with the relative density of points indicated by the color bar at the bottom left-center of the figure (right).

in Qumran (R-4Q2 and R-4Q11) show ratios of calcium to sodium to sulfur that are significantly different from the TS and the R-4Q1 fragment results, suggesting a different method of production. Although side 2 of R-4Q2 shows a higher concentration of sodium than R-4Q11 and side 1 of R-4Q2, its Na-Ca-S ratios correspond with the ratios of neither glauberite nor thénardite.

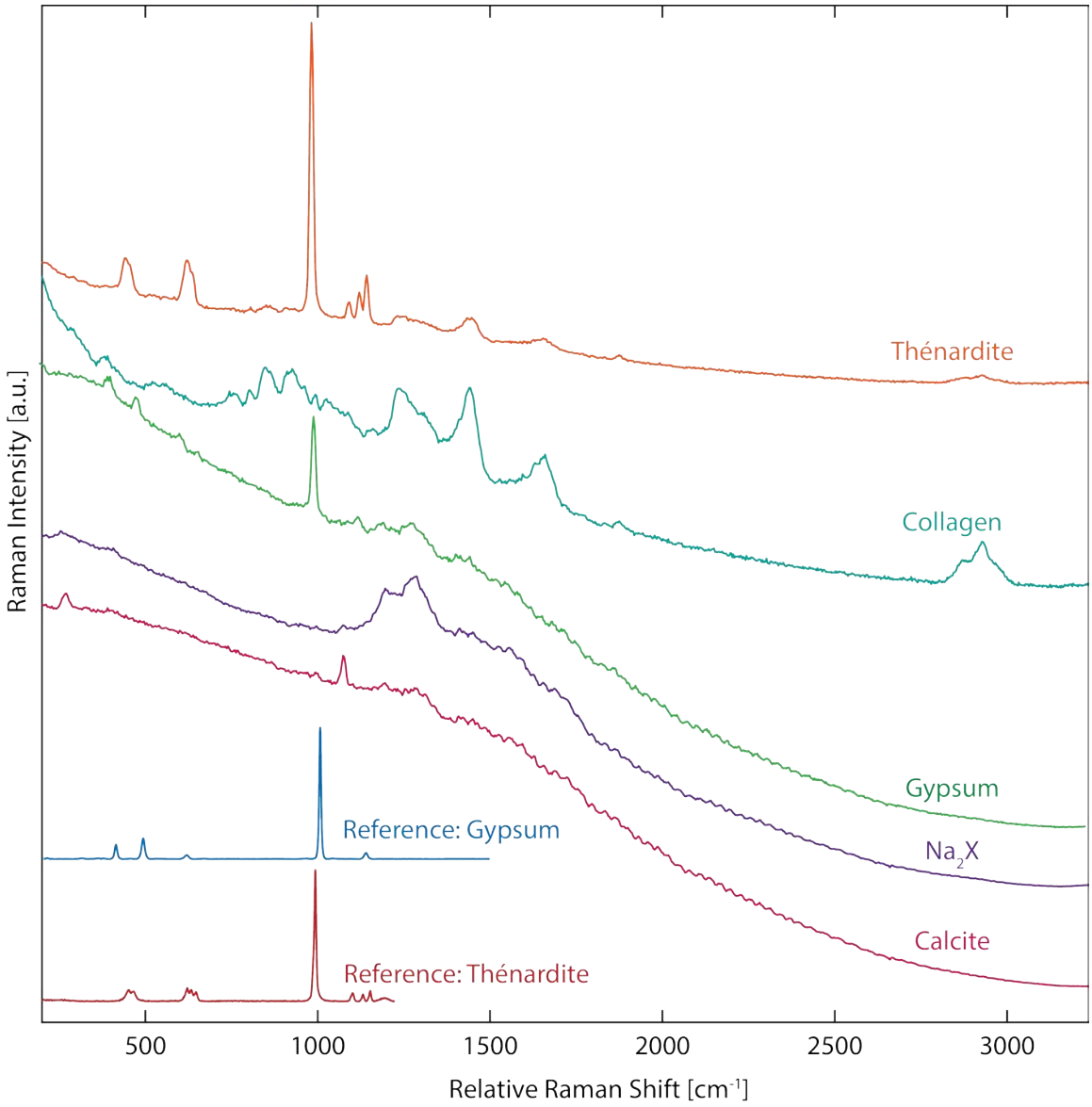

Figure 5-8: **Raman (785 nm) spectra showing the detected components of the R-4Q-1 scroll and reference spectra for gypsum and thénardite.**

5.4 Comparison of Dead Sea Scrolls using ternary diagrams

5.5 Discussion of characterization results

Among the DSS the TS is significant because it comprises several anomalies. Its unusual text appears on the flesh side rather than hair side of the exceptionally

thin ivory-colored parchment. Previous studies have already pointed at the unusual stratigraphy of the scroll: the text sits on the inorganic layer that covers the extremely thin collagenous base. There are several hypotheses that seek to explain the latter, including the suggestion that the parchment was split into two layers before application of the inorganic layer, but no decisive proof has been offered and, therefore, it remains the subject of future research.

5.5.1 Sulfate salts in the inorganic layer

Morphologically, the TS consists of a collagenous organic substrate, and a bright, ivory inorganic layer on which the text was written. The present study focused on the characterization of this unique inorganic layer with the objective of understanding the ancient manufacturing technology used to produce the TS, which differs significantly from the other scrolls of the same collection. Using µXRF and EDS, mineral particles rich in Na, Ca, and S were identified, and by applying Raman spectroscopy, the chemical nature of these minerals was determined. The inorganic layer was found to contain a range of minerals, most of which are sulfate salts. Apart from gypsum and its analogues, glauberite $Na_2Ca(SO_4)_2$ and thénardite Na_2SO_4 were also identified [88]. Although the possibility that some of the evaporitic minerals found on the TS may be degradation products of the original inorganic layer cannot be excluded, it is certain that these minerals do not originate from deposition within the caves. The sulfate-containing layers on the surfaces of all of the investigated fragments found on the floors of different Qumran caves have already been studied [89], and the mineral sediments on the fragments that were laying on the floors do not match the minerals detected in this study. This result clearly demonstrates the inclusion of the identified evaporitic minerals in the scroll production process.

5.5.2 Comparison of EDS data for Temple Scroll and Cave 4 fragments

Using large-area EDS data to plot the ratios of the three major elements in glauberite and thénardite (i.e., Ca, Na, and S) on ternary axes allowed for the fast assessment of whether parchment samples from Cave 4 (i.e., R-4Q1, R-4Q2, and R-4Q11) might contain similar phases to those found on the TS. Indeed, R-4Q1 consisted of many data points with Na-Ca-S ratios corresponding to that of glauberite, and upon further analysis with Raman spectroscopy, the presence of the "Na_2X" phase was confirmed (Fig. 5-8). Ternary diagrams generated for other fragments from Cave 4 show Na-Ca-S ratios that are similar to each other, but different from the TS and R-4Q1. These results suggest that the techniques used to produce the TS may be a part of a larger manufacturing system, and that production strategies for the TS and R-4Q1 may share some common features.

It should be noted that the use of ternary diagrams for characterization purposes is not without its limitations. EDS data, due to the relatively low spectral resolution of the technique, is inherently noisy, and data points representing the ratios of the elements when they are only present in trace amounts would show up as noise in the ternary diagrams. For this reason, it was crucial to plot large sets of data on ternary axes, since the positions of the centers of clusters of points would indicate the average elemental ratios in a given phase. In addition, since ternary diagrams only account for the ratios of three elements, and phases of different chemistries could contain the three elements of interest in the same ratios, it is possible for different phases to occupy the same region of the diagram. This issue could be resolved in a number of ways: the EDS data points could be clustered with respect to several quantified elements (as shown in Fig. 5-6), or the technique could be used in conjunction with complementary characterization techniques, such as Raman spectroscopy, as was done in this study. In any case, the strength of this technique lies in that it allows for the rapid and coarse understanding of the phases present and how they are distributed throughout a sample. In addition, this approach enables the quick comparison of

large sets of samples to determine their similarities and differences (as in Fig. 5-7).

5.5.3 The Temple Scroll production technology

The Dead Sea brine has a relatively low sulfate concentration, and although these evaporitic salts are particularly common in non-marine hypersaline environments [89], glauberite and thénardite are not commonly found in the Dead Sea region [90]. This introduces intriguing questions on the provenance of the TS, which will be the subject of future studies.

Regardless of the origin of the mineral evaporites detected on the TS, their presence in the form of a continuous layer suggests a treatment that differs from the production of other light-colored, untanned (i.e. "Western") parchments of the collection, which are represented in the present study by two fragments from Cave 4: R-4Q1 and R-4Q2. The "Eastern" technology is represented in this study by another Cave 4 fragment: R-4Q11 [83]. The results of the present study suggest that the inorganic layer of the TS is part of a unique production technology that was applied in antiquity; it differs greatly from the "Eastern" group but bears similarities to the "Western" group of parchments. The TS can, therefore, be classified as a "Western" parchment that was modified through the addition of an inorganic layer as a writing surface. Whether these different technologies were equally implemented in the region for parchment production, however, remains unclear. The link between the production provenance and the applied technology would critically inform the understanding and reconstruction of the technological transfer.

5.5.4 Presence of nitrates in collagen layer

The close association of nitrates and ammonia with the collagen fibers throughout the entire TS fragment is either a result of the parchment production process and the salts used therein, or the post-production degradation/diagenesis of the scroll, for example, during the sojourn in the cave. The former would be possible if evaporitic salts containing nitrates were used in production, but this hypothesis is unsupported

by the fact that nitrates were only found in the collagen layer and not in the inorganic mineral layer. We found the degradation/diagenesis hypothesis to be more plausible considering the traditional degradation pathways of collagen within parchments. It is well-understood that artificially-aged parchments that are exposed to high concentrations of NO_x gases uptake NO_2, after which NO_3^- ions form within the collagen fibers [91, 92, 93]. These ions and their associated radicals might promote the oxidative cleavage of the collagen chains, the byproduct of which is NH_4^+ [2]. Combined, these two agents would lead to the formation of ammonium nitrate within the TS collagen. Another potential reason for the diagenetic origin of NH_4NO_3 might be related to the presence of bats in Cave 11, which could have affected the microenvironment of the scrolls. The bat excrements (urea and feces) that were ubiquitous in the cave could have led to nitrate enrichment and the subsequent oxidative cleavage described above.

5.5.5 Potential damage due to the presence of hygroscopic salts

Perhaps most critically to our understanding of the TS was the identification of evaporitic sulfate salts in the inorganic layer of this parchment, which places increased emphasis on the close monitoring of environmental conditions that are employed for the long-term storage and preservation of these ancient manuscripts. Due to the hygroscopic nature of evaporitic salts, the results presented here highlight their potentially unanticipated sensitivity to even small-scale changes in relative humidity, which could induce volumetric changes in the inorganic phase as well as increase the concentration of water in contact with the collagen, which may in turn accelerate its degradation. In addition to providing insight into the potential degradation pathways of the DSS and the development of methods to slow these processes, the high throughput nature of the techniques presented here open the door to the rapid, large-scale screening of the remaining thousands of small, and as of yet, unclassified DSS fragments based on their chemical signatures and associated manufacturing methods.

5.6 Summary

Previous studies conducted by Dr. Roman Schuetz identified the presence of evaporitic salts throughout the inorganic layer of the Temple Scroll. µXRF and SEM-EDS studies showed the presence of particles that were rich in Na, S, and Ca (Fig. 5-3), and further studies using confocal Raman microscopy (Fig. 5-4) showed a double peak at 987 cm^{-1} and 1007 cm^{-1}, which closely matched the Raman spectrum of an aqueous mixture of Na_2SO_4 and $CaSO_4$ that was dried through fast evaporation at 250°C (Fig. 5-5), and the characteristic triplet spectral signature that corresponds with vibrational units of the type "Na_2X," often detected in the minerals glauberite and thénardite. Large-area, high-resolution quantitative element maps collected using low-vacuum SEM-EDS were then used with ternary diagrams to show which of a set of the Dead Sea Scrolls obtained from another Qumran cave (Cave 4) may contain similar phases to those identified in the TS. The results showed that scrolls R-4Q2 and R-4Q11 showed Na-S-Ca elemental ratios that were similar to each other, but notably different from the TS. However, R-4Q2 was shown to have similar Na-S-Ca elemental ratios as the TS in some regions, and upon inspection using Raman spectroscopy, was found to thénardite and a phase that exhibited the characteristic "Na_2X" triple peak.

The use of environmental SEMs in low-vacuum mode is particularly useful in the study of ancient samples that may not be coated due to their inherent cultural value and those that may be easily damaged under high-vacuum conditions. Raman spectroscopy, when conducted using lower incident wavelengths and lower laser powers, may also be used to safely characterize samples, but the long data collection times required for mapping areas of interest make it difficult to study large sets of samples, as in the case of the Dead Sea Scrolls. Due to the high-throughput nature of SEM-EDS, it is possible to collect quantitative elemental data for large regions of a sample at high resolution in relatively short amounts of time. As such, it becomes possible to quickly identify which regions of a mapped area contain elemental ratios that match the stoichiometry of minerals of interest, as was done for glauberite and thénardite in this study. Furthermore, the use of color-coded ternary diagrams (Fig. 5-7), which

illustrate the spatial distribution of the ratios of the elements of interest (here, Na, S, Ca) enables the identification of both regions of a mapped sample area that match elemental ratios of interest as well as similarities across different samples (as for samples R4Q-2 and R4Q-11). Conducting this analysis for large areas at high resolutions is particularly useful in cases such as these, where the minerals of interest may only occur in small sub-regions of samples, for example in the Na-S-Ca particles identified on the Temple Scroll in this study.

Part II

Interfacing chemical characterization data with mechanical modeling techniques

Chapter 6

Background: Mechanical modeling of composites and cementitious materials

In the case of historic materials, such as ancient artifacts, results from chemical characterization aid conservators and researchers by providing information about the constituents of ancient composites, how they behave in various environmental conditions, and how they might react to cleaning or protective substrates. Mechanical characterization of historic materials, such as ancient building materials, allows for the understanding of how structures may deform or deflect under various loading conditions or with the addition of support structures, or whether they will undergo catastrophic damage in the case of a severe dynamic event, such as an earthquake. Although cylindrical specimens for compression testing have been extracted from historic structures, such as in the study of adobe from Aveiro, Portugal [3], it is often more desirable to use small samples to perform mechanical characterization given the cultural value of these materials. As such, other researchers have sought to use less-destructive processes, such as microdrilling using 5mm drill bits, in order to measure the compressive strength of ancient clay bricks without macro-scale compressive testing [4]. The chemomechanical framework presented in this thesis is promising in this regard, since it requires samples that are only a few millimeters in size—just large

enough to capture the features that contribute to the effective properties.

Although they are typically better understood than ancient building materials, modern building materials produced using ordinary Portland cement (OPC), the most commonly used cement in modern construction, also tend to have constituents with properties that cannot be precisely predicted. The elastic properties of hardened cement paste (cured mixtures of OPC and water) and OPC mortars (cured mixtures of OPC, water, and sand) vary depending on many factors, including the water-to-cement ratio used at the time of mixing, the sand-to-cement ratio, age, curing conditions, and the presence of supplementary cementitious materials. For these reasons, modern cementitious composites were chosen for the development and validation for the chemomechanical homogenization framework to be presented. Sample cross-sections that are only a few millimeters in width will be used with BS-SEM, SEM-EDS, microindentation, and finite element modeling to estimate their effective elastic properties.

6.1 Mechanical modeling of composites

6.1.1 Analytical homogenization

Homogenization refers to the process of finding the effective properties of a representative volume element (RVE) of a composite material. There are three major characteristics that affect the elastic properties of a composite: the volume fractions of its constituents, their independent elastic properties, and their geometric arrangement. If the constituent phases' geometric arrangement is neglected, the upper and lower bounds for the bulk elastic properties of a composite may be computed, and if they are narrow enough, they can provide sufficient information about the composite's bulk elastic behavior. If they are not, they may still be used to validate estimates found using other analytical methods, including those based on statistical analyses [94, 95], elastic wave scattering theory [96, 97], or other methods for narrowing the bounds [98].

It must be noted that the Voigt upper bound [99], computed using the equivalent case of loading a composite made of unidirectional, continuous fibers in the axial direction, and the Reuss lower bound [100], computed using the equivalent case of loading that composite in the transverse direction, may be very different if the composite's constituents' properties are notably different [101, 102]. Other bounds include the Taylor [103] and Sachs [104] bounds for nonlinearly behaving composites, and the Hashin-Shtrikman bounds on the bulk and shear moduli of composites [105], which are narrower than the Voigt-Reuss bounds and have since been derived for composites of more than two constitutive phases [106]. Although analytical bounds may be used to estimate bulk elastic properties, such as in the case of the Voigt-Reuss-Hill average of the Voigt and Reuss bounds [107], the true elastic properties will depend on the constituent phases' geometries. In the field of micromechanics, many approaches have been developed for the analytical homogenization of composites of various geometries, such as the self-consistent scheme [108] and the Mori-Tanaka method [109], based on Eshelby's solution for an inclusion embedded in an infinite matrix [110], and for the analytical homogenization on nonlinear elastic composites [111].

6.1.2 Computational homogenization through finite element modeling of composites

Due to the varied sphericity and relatively high angularity of the river sand grains used to produce the mortars in this work, it is difficult to select an analytical model that would accurately estimate the bulk material properties. Computational homogenization techniques are able to account for these irregular geometries and tend to produce sufficiently accurate homogenization results for composites of known microstructure [112]. In some studies of composites, both analytical and computational homogenization techniques have been combined in multi-stage methods to make use of the advantages of both methods. One such study used the Mori-Tanaka method to homogenize the matrix and user-generated two-phase finite element models to simulate the composite [5].

One commonly used computational homogenization technique, finite element modeling, has been shown to be effective in capturing the effects of features that occur in real composites on effective material properties, such as interfacial debonding [113, 114], matrix cracking [114], applied and residual stresses [115], and porosity. Finite element modeling has been used to study the mechanical behavior of composites that display heterogeneity at different scales, including fiber-matrix composites [114], particulate-reinforced alloys [113, 116, 117], piezoelectric composites [118], textile composite beams [119], and nanoporous graphene membranes [120]. It has been previously shown that whereas 3D modeling was necessary to predict non-linear behavior, such as fatigue life, fracture toughness, and strain to failure in particle-reinforced aluminum, 2D models were able to predict the same effective elastic properties as 3D models [117].

Finite element models may be generated using computer-aided design software, especially when studying designed composites with a repeated unit cell geometry [121], but they may also be generated using Monte Carlo-based techniques, which account for interfaces and variations in the size, shape, orientation, dispersion, and spatial distribution of constituents [122], and imaging techniques such as computed microtomography (CT) when phases are distinguishable based on their greyscale intensity values [123, 124]. CT may introduce challenges if the contrast between phases is poor, for example in the study of carbon-carbon composites such as carbon fibers in a carbon matrix, but strategies for data treatment have been developed to address these concerns [125, 126].

6.1.3 Image-based finite element modeling

Finite element models that are produced based on images of a material being studied are particularly useful, since the true geometry, including variations from the ideal case and irregularities in microstructure, may be captured in the model. For this reason the results of image-based finite element modeling tend to show better agreement with experimental data than the unit cell approach [126]. It has also been shown that when compared with theoretical solutions, 2D and 3D finite element models based on

digital image-based meshing are able to predict locally averaged stresses and apparent mechanical properties, for example in the analysis of a 2D compression plate and a 3D circular cantilever beam [127]. Furthermore, work has been done to improve accuracy when simulating local phenomena, such as failure or adaptation, by applying post-processing filtration techniques [128].

Image-based finite element modeling has been shown to be effective in modeling materials and composites with complex geometries, such as trabecular bone [128, 129], dental structures [130], and cement-reinforced bone [131]. For generating 2D models, micrographs may be used with computational tools, such as OOF [132] and OOF2 [133], which segment the micrographs based on their greyscale intensity or RGB values to map the distribution of phases and convert the images into finite element models. 3D image-based FEM is commonly conducted in conjunction with tomographic techniques, such as holotomography [134], X-ray tomography [126], phase contrast X-ray tomography [135], and transmission computed tomography [136], for example in the modeling of carbon-carbon composites, where the distribution of the matrix, fibers, and pore space must be determined [126, 134, 135, 136], or in the modeling of reinforced bone, where the distributions of original bone tissue and bone cement must be determined [131]. Other techniques for generating 3D models include serial sectioning combined with other characterization techniques, such as electron backscatter diffraction (EBSD), in which the spatial distributions and crystallographic orientations of grains may be determined for a polycrystalline material [137].

6.2 Mechanical modeling of cementitious materials

6.2.1 Homogenization of cement, mortar, and concrete

The homogenization of concrete is a multiscale problem, where each of the scales may be homogenized individually [138]. At the 10^{-8} to 10^{-6} m scale, the two types of C-S-H, of which the ratio depends on the water-to-cement ratio, are distinguishable based on their elastic properties [139, 140, 141]. The next scale in the hierarchical

structure is that of cement paste at 10^{-6} to 10^{-4} m, which includes C-S-H gels, calcium hydroxide formed via the hydration of free lime (calcium oxide), water, and unhydrated clinker phases, such as alite (Ca_3SiO_5, or C_3S in cement chemist notation) and belite (Ca_2SiO_4, or C_2S in cement chemist notation). Previous studies in the homogenization of cement paste include the use of the volume fractions of phases along with micromechanics models to perform analytical homogenization [138], and the use of finite element models of the cement paste microstructure obtained using 3D cement hydration models to estimate the effective elastic properties of hydrating cement paste [142]. Another previous study employed nanoindentation grid mapping to obtain statistical information on the mechanical properties of the phases present in hardened cement paste and used those statistics to generate random field models, which were subjected to computational homogenization via finite element modeling [143]. The next scale in the multiscale framework of concrete is that of mortar—the scale of interest in this work—at 10^{-3} to 10^{-2} m, which includes cement paste, sand particles, and the ITZs along the surfaces of the sand particles. The final, largest scale is that of concrete at 10^{-2} to 10^{-1} m, which includes larger aggregates, their ITZs, and mortar homogenized as one phase.

6.2.2 Indentation of cementitious materials

The Oliver-Pharr indentation method was developed to measure the local elastic modulus and hardness of sample regions [144], and over the years, indentation techniques continue to be further refined and modified [145]. The technique was later extended to allow for the measurement of the local creep modulus through the study of the logarithmic creep compliance curve obtained from a minutes-long indent [146]. Such nanoindentation creep experiments have been performed on modern cementitious materials, for example in showing that the creep behavior of calcium silicate hydrates (C-S-H) is indicative of the long-term creep behavior of cementitious materials [146].

An indentation depth of h gives information about the properties of a material at a length scale of $L = 4h$, and the material properties obtained from indentation curves are those of the material homogenized over a volume of L^3. Therefore, the

indentation depth determines the scale at which the resulting mechanical data is valid. Nanoindentation, in which indentation depths are below 0.2 µm [147], is used for testing nanoscale regions, such as thin films [148, 149, 150, 151, 152], regions of bone samples [28] and modern concrete and cement phases [146, 139, 153, 154, 155, 156]. In the study of cementitious materials, it has been used to study very small features, such as interfacial transition zones (ITZ) between crushed red brick particles and the binding phase in ancient mortars [157], as well as the ITZ in reinforced concrete [158, 159], individual clinker phases [160], portlandite [139, 140], and C-S-H gel [139, 140], and it has even been used to distinguish the two types of C-S-H [153]. Microindentation, in which indentation depths are greater than 0.2 µm, is used in this work, since the features being observed (i.e. phases, such as sand particles and cement paste) occur at a larger scale. After assigning mechanical properties to the phases, the maps are used to generate finite element models, which are used to computationally homogenize the samples, the results of which are validated using analytical bounds.

6.2.3 Finite element modeling of cementitious materials

FEM has proven to be effective in estimating the effective elastic properties of cementitious composites like mortars and cement paste, including those that have been leached [161, 162, 163]. Finite element analysis has been used at length to study structural elements under various conditions, such as in the nonlinear analysis of the load-carrying capacity of masonry arches [164], in the modeling of airport pavements at sub-critical temperatures under heavy aircraft gear loading conditions [165], and in the analysis of the high and normal strength reinforced concrete slabs subjected to blast loads [166], concrete beams subjected to impact loads [92], deteriorated orthogonally reinforced concrete panels [167] and concrete slabs with partial depth cracks [168]. At a smaller scale, 3D nonlinear FEM has been used to study damage in foamed concrete cubes under compression [169], and CT scans of hardened cement paste have been discretized based on greyscale intensity value into pore space, unhydrated clinker, and hydrated cement then converted to both 2D and 3D finite element models to perform computational homogenization [170].

Many of the techniques used in image-based finite element modeling rely on the contrast between different phases, but there are cases in which phases may be difficult to distinguish, for example in the study of cementitious materials using CT or BS-SEM, where phases may have similar or overlapping greyscale intensities. This work seeks to address this problem by segmenting chemical images based on chemistry instead of appearance in micrographs. Large-area, high-resolution SEM-EDS is used to quantitatively map the distribution of elements present in sections of a series of cement paste and mortar samples. The data is then segmented using k-means clustering to map the distribution of the phases present. After determining the elastic properties of the identified phases using microindentation and compression testing, the maps are converted to finite element models, which are used to perform computational homogenization and determine the effective elastic properties of the cement and mortar samples. The results are then validated using laboratory compression testing results.

Chapter 7

Large-area high-resolution chemomechanical mapping and computational homogenization of cementitious materials

In this chapter, a chemomechanical framework for the study of composite materials of unknown composition is applied to a series of ordinary Portland cement-based mortars, which bear numerous similarities to ancient Roman mortar. The phase maps are combined with microindentation and compression testing data in order to generate high resolution maps of mechanical properties, which are used as initial configurations for finite element models that are subjected to uniaxial compression and pure shear deformations in order to investigate the microstructure response. The results are then used to estimate the effective Young's modulus, shear modulus, and Poisson's ratio of each sample, and these numerical results are then compared to upper and lower bounds from elastic composite theory and validated using laboratory uniaxial compression testing data. The results of a parametric study of the role of binding phase-aggregate interfaces on the effective elastic properties are also presented.

This framework begins with the high-resolution, large area chemical maps that

were introduced in the Privernum mortar study in Chapter 3. Through the use of k-means clustering or other unsupervised learning techniques, it is possible to assign each pixel to a phase, for which the mechanical properties may then be determined. This may be conducted using one or more of several possible techniques, ranging from the use of literature values when the identity of the phase is known (through vibrational characterization techniques, such as Raman or infrared spectroscopy, for example), to micro- or nanoindentation, which is able to measure the mechanical properties of materials at very short length scales. With the resolution of the resulting maps of mechanical properties being limited only by the resolution of the chemical characterization techniques, it is possible to generate models of the material being studied that reflect the true geometries and arrangements of the constituent phases.

In the following study, this framework is carried out on a series of mortars that were produced using OPC, which is similar to ancient Roman mortars in a number of ways. Both modern and ancient mortars are mixtures of fine aggregate (sand) and hardened cement paste. They also both consist of gel phases in the binding matrix: during the hydration of OPC, C-A-S-H and C-S-H form as hydration products, and through the pozzolanic reaction that occurs during the production of ancient Roman mortar, C-A-S-H is formed. Lastly, they both often contain aluminous and siliceous supplementary cementitious materials (SCMs): in the case of modern mortars, SCMs such as volcanic ash and fly ash are sometimes added to reduce the carbon footprints of the mixtures, and in the case and ancient Roman mortars, volcanic ash and sometimes crushed red brick (cocciopesto) are added to allow for the pozzolanic reaction. However, in contrast to mortars produced using OPC, which reach almost their full stiffness and strength after 28 days of aging, ancient Roman mortars can take upwards of six months to reach a similarly mature state. Furthermore, the low cost of production of modern mortars makes it possible to make and test many different types of mixtures, which is useful for ensuring that the framework yields valid results. By using OPC mortars as proxy samples for extremely valuable ancient Roman mortars, the framework can be tested before it is applied to the homogenization of Roman mortars and other ancient composites of interest.

Sample	OPC [%]	Volcanic Ash [%]	Sand/Cement Ratio	Young's Modulus [GPa]	Strength [MPa]
VA-15	85	15	2.75	29.22 ± 0.14	43.90 ± 3.94
VA-10	90	10	2.75	28.69 ± 0.73	46.32 ± 2.37
VA-05	95	5	2.75	28.17 ± 0.98	44.62 ± 1.38
VA-00	100	0	2.75	28.73 ± 2.92	43.62 ± 3.28
OPC-175	100	0	1.75	30.18 ± 0.60	59.06 ± 4.39
OPC-075	100	0	0.75	26.65 ± 1.13	60.24 ± 3.76
OPC-000	100	0	0	15.60 ± 1.19	50.76 ± 3.05

Table 7.1: Mix proportions, Young's moduli, and strength data obtained via compression testing with the use of strain gauges for the hardened cement paste and mortar samples used in this study. Standard deviations are also given for the Young's moduli and strength data.

7.1 Chemomechanical homogenization of OPC mortar samples

7.1.1 Production and compression testing of mortars

Mortar samples were produced using Portland cement (Quikrete, Atlanta, GA, USA), natural pozzolans (Calchera, Grigno TN, Italy), and fine river sand with a particle size range of 0–500 µm (Calchera, Grigno TN, Italy) in the proportions shown in Table 7.1. A water-to-cement ratio of between 0.350 and 0.485 were used for each sample. Starting with the standard mixture of 100% OPC, 0% natural pozzolans, and a sand-to-cement ratio of 2.75 (sample VA-00), the mixture was modified in two ways. First, the mixture was modified by partially substituting OPC with natural pozzolans by 5%, 10%, and 15% to produce the samples VA-05, VA-10, and VA-15, respectively. Secondly, the sand-to-cement ratio was reduced from 2.75 to 1.75, 0.75, and 0 to produce the samples, OPC-175, OPC-075, and OPC-000, respectively.

Each mortar or cement paste mixture was set in four 2-inch diameter cylindrical molds for 24 hours, then demolded and cured underwater. All samples were aged to at least 28 days before testing. Samples VA-00, VA-05, VA-10, and VA-15 were left to cure for longer than 28 days to account for the retardation of the cement hydration process resulting from the partial substitution of OPC with volcanic ash. Three of

the four cylinders were then capped with gypsum putty and subjected to compression testing according to the ASTM C109 standard for the compressive strength testing of hydraulic cement mortars. The specimens were loaded at a rate of 39 kN/s, and two diametrically opposed averaging clip-on extensometers with a 1-inch gauge length were placed on each sample during loading. The outputs from the two extensometers were averaged to obtain the strain undergone by each sample throughout loading. The compression testing results are presented in the final two columns of Table 7.1.

The experimental result for the shear modulus, G, of each sample was computed using the constitutive relationship relating E, G, and the Poisson's ratio ν for isotropic materials given by

$$G = \frac{E}{2(1-\nu)} \tag{7.1}$$

The Poisson's ratio of the mortar samples was taken to be 0.18 [57]. These elastic properties were used to validate finite element models developed from the cross-sectional characterization of these samples.

7.1.2 SEM-EDS characterization of mortars

BS-SEM and SEM-EDS were used to characterize the samples. A sample was then cut from the fourth cylinder for each mixture using a slow speed water-cooled diamond saw, and each sample was embedded in epoxy, sectioned, and polished. Each polished sample was characterized using a Tescan Vega GMU scanning electron microscope equipped with a Bruker XFlash 5030 X-ray detector. Mapping data were acquired at an analytical working distance of 17 mm and at an accelerating voltage of 16.5 keV. SEM-EDS maps were collected at a magnification of 70x at a resolution of 512 pixels by 512 pixels, resulting in a view field width of about 2200 µm. The SEM-EDS map spectra were then calibrated and the data was quantified using Bruker's ESPRIT 2.1 software using the built-in Linemarker PB-ZAF correction, which corrects for background radiation, atomic number effects, absorption of X-rays by the specimen, and fluorescence. The SEM-EDS element maps were quantified using bins of 2 pixels

by 2 pixels in order to improve the statistics in determining the atomic percentages of each detected element throughout the mapped area, which resulting in quantified maps of resolution 256 pixels by 256 pixels.

For each prepared sample, at least three square-shaped regions were analyzed. Fig. 7-1 shows examples of regions studied for samples OPC-175, OPC-075, and VA-15. The suffixes of the sample names shown in Fig. 7-1A, Fig. 7-1F, and Fig. 7-1K indicate the region of that sample studied (a1 corresponds to area 1, etc.).

Greyscale quantitative Ca, Si, and Al maps are shown for sample regions OPC-175-a1, OPC-075-a1, and VA-15-a2 in Fig. 7-1B-D, Fig. 7-1G-I, and Fig. 7-1L-N, respectively. In these maps, the greyscale intensity at each pixel corresponds to the atomic percentage of that element present at that location of the mapped area. For each of the 256 by 256 pixels of each mapped region, the Ca-Si-Al ratio was computed and plot on ternary axes (Fig. 7-1E, Fig. 7-1J, Fig. 7-1O) as ternary density plots, in which the most densely populated regions of the plots are plotted in yellow and the most sparsely populated regions are plotted in purple, as indicated by the color bar to the top-right of Fig. 7-1E. In each of the ternary density plots in Fig. 7-1, multiple clusters of data points can be seen. This suggests that the data may be grouped into phases, where each phase consists of pixels that are similar in elemental ratios.

7.1.3 K-means clustering of SEM-EDS data to obtain phase maps

To group the 256^2 pixels of each mapped region into chemically distinct phases, k-means clustering was used to partition the quantitative SEM-EDS elemental data. K-means clustering, an unsupervised learning technique, was chosen since the elemental compositions of the phases present in the mortar mixtures were not known a priori. Following Ca, Si, and Al, the next most prevalent element in each sample was found to be Mg, followed by subsets of the following elements in varying quantities: K, Fe, Na, Cl (likely from the resin in which the samples were embedded prior to polishing), and S. Significant amounts of C and O were also detected, but these were excluded from

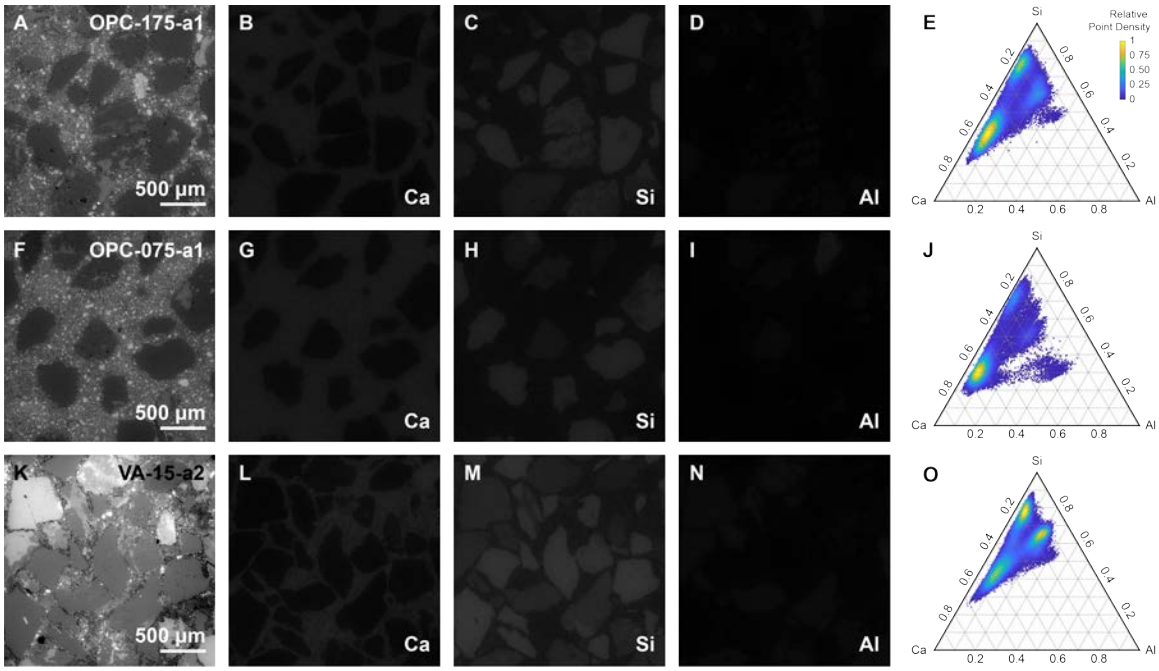

Figure 7-1: **Quantitative SEM-EDS maps and ternary density plots showing the distribution and ratios of calcium, silicon, and aluminum in atomic percent. A**: BS-SEM image of a mortar sample region (OPC-175-a1) with a sand/cement ratio of 1.75 and **B-D**: corresponding quantitative Ca, Si, Al maps. **E**: Ternary density plot showing the ratios of Ca to Si to Al present throughout the pixels of the mapped area. **F**: BS-SEM image of a mortar sample (OPC-075-a1) with a sand/cement ratio of 0.75, **G-I**: corresponding quantified Ca, Si, Al maps, and **J**: ternary density plot. **K**: BS-SEM image of a mortar sample (VA-15-a2) with 15% of the OPC substituted with volcanic ash, **L-N**: corresponding quantified Ca, Si, Al maps, and **O**: ternary density plot.

the analysis since they are difficult to quantify reliably due to the ease of adsorption of CO_2 and O_2 onto the sample surface and surfaces within the SEM chamber. After normalizing the elemental data, clustering was performed with respect to all the elements that could be reliably quantified for each sample area.

The clustering results from this selection process are shown for six examples of sample regions in Fig. 7-2. BS-SEM images of each of the mapped regions are shown in Fig. 7-2A-F. The identified clusters are shown on Ca-Si-Al ternary axes in Fig. 7-2G-J, and the corresponding phase maps showing the spatial distribution of these clusters throughout the mapped area are shown in Fig. 7-2K-P. For cementitious materials, regions of the Ca-Si-Al ternary diagram correspond to particular expected

phases. For example, the hydration product C-S-H theoretically lies along the Ca-Si axis closer to the Ca vertex, while the hydration product C-A-S-H lies further away from the axis due to the incorporation of Al. Due to the scale and resolution of the mapped regions, these are combined in the "cement paste" phase visible in the maps and ternary diagrams (e.g. in red for sample regions OPC-175-a1 and VA-00-a2). For the samples in which pozzolana was incorporated (Fig. 7-2, sample regions VA-05-a2, VA-10-a3, and VA-15-a2), the clusters corresponding to the cement phase lie further away from the Ca vertex due to the presence of the siliceous or siliceous-aluminous volcanic ash particles in the binding phase.

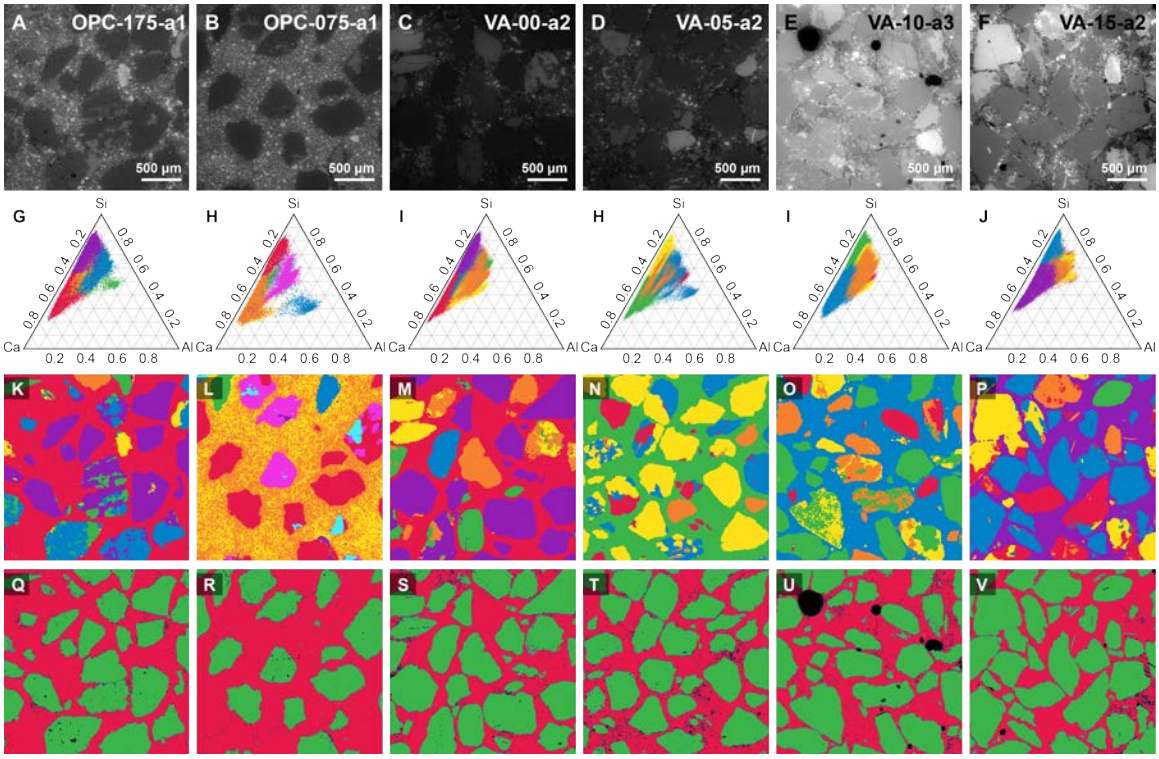

Figure 7-2: **BS-SEM characterization and k-means clustering of quantitative SEM-EDS data of six mortar sample regions.** **A-F**: BS-SEM images of six different sample regions. **G-J**: The corresponding quantitative SEM-EDS data for each region were segmented using k-means clustering, the results of which are shown on Ca-Si-Al ternary axes. **K-P**: Spatial distributions of the chemically distinct phases identified are shown for the mapped sample regions. **Q-V**: Simplified phase maps showing distribution of aggregate (green), binding phase (red), pore space (black), and aggregate-binder interfaces (blue).

The different mineral phases present throughout the aggregate phase are also

distinguishable based on the positions of their clusters on the ternary axes. Grains of quartz (SiO_2) theoretically lie at the Si vertex, but due to the low spectral resolution of SEM-EDS and the resulting noise in the quantitative elemental data, the cluster lies away from the vertex, but is still identifiable as the uppermost cluster on the ternary diagrams (e.g. purple phase for sample regions OPC-175-a1 and VA-00-a2). Other mineral phases typically found in sand include mica and feldspars, which vary in Si, Ca, and Al content; such phases would lie below the quartz cluster on the ternary diagram. For example, aggregate grains that are richer in Al and Ca than quartz are shown in orange for sample regions VA-00-a2, VA-05-a2, VA-10-a3, and VA-15-a2. Another aggregate phase that is even richer in Al than this phase is shown in blue for sample regions OPC-075-a1 and VA-05-a2.

These features highlight the utility of using unsupervised learning to distinguish phases. When supervised learning or classification techniques are used, the stoichiometries of the phases must be known a priori, but in cases such as this, where natural pozzolana of unknown composition is used as a supplementary cementitious material, and sand of unknown mineral composition is used as aggregate, this is not always possible.

Due to the high heterogeneity of the samples being studied, it would be prohibitively challenging to obtain microindentation data for specific sand grains identified using this phase mapping technique. Since the aggregate grains, regardless of their mineral content, would all be considerably stiffer than the binding phase, the complex phase maps in Fig. 7-2K-P were simplified to two-phase maps. Each cluster was labeled as either aggregate or binding phase, and the simplified phase maps are presented in Fig. 7-2Q-V, where green corresponds to aggregate material and red corresponds to the binding phase. For cases in which epoxy-filled void space was identified as a separate phase, these regions were labeled as binding phase for the two-phase models. K-means-based image segmentation was then used to partition the pixels of the BS-SEM images and thereby identify the distribution of pores, bubbles, and other voids present in the mapped regions. The pixels that corresponded to the void space visible in the BS-SEM images were then combined and overlaid onto the

simplified phase maps and are shown in black in Fig. 7-2Q-V. Finally, the interfaces between the aggregate and the binding phase were identified computationally and are colored blue in the simplified phase maps in Fig. 7-2Q-V.

7.1.4 Generation of finite element models

The resulting phase maps were used to generate finite element models of size 256 elements by 256 elements (matching the resolution of the SEM-EDS maps). Due to the varied sphericity and relatively high angularity of the river sand grains used to produce the mortars in this work, it is difficult to select an analytical model that would accurately estimate the bulk material properties. Computational homogenization techniques, such as finite element modeling, are able to account for these irregular geometries and tend to produce sufficiently accurate homogenization results for composites of known microstructure [112].

Nanoindentation is carried out using indentation depths of below 0.2 µm, which equates to the indented material being homogenized over a maximum length scale of 0.8 µm. Microindentation, in which indentation depths are greater than 0.2 µm, is used in this work, since the features being observed (i.e. phases, such as sand particles and cement paste) occur at a larger scale. Each phase map is 2200 µm in width, which means that each of the 256 by 256 pixels is approximately 8.6 µm in width. In the microindentation experiments conducted for this study, indentation depths were approximately 5 µm, which resulted in the indented material being homogenized at a length scale of approximately 20 µm, which is comparable to the pixel size and therefore considered appropriate for this work.

The microindentation measurements were carried out using the Anton Paar Micro Scratch Tester, and the indentations were made using a diamond-tipped Berkovich stylus. Prior to carrying out the indentations, the tip was calibrated in order to obtain its tip area function using a sample of standard borosilicate glass (BK 7) with a Poisson's ratio of 0.2 and a plane strain modulus of 86.4 ± 1.8 GPa. The contact points were manually selected using Anton Paar's proprietary software (Indentation, v. 6.2.9), and the hardness and indentation moduli of the aggregate and binding

phases were computed by the software using the Oliver & Pharr method. The indentation moduli were converted to material Young's moduli using custom MATLAB software. The peak force was selected so that the indentation depths were approximately 5 µm.

The elastic modulus of the aggregate phase was obtained through microindentation. Between three and five aggregate particles from each sample were indented, and the resulting indentation modulus was found to be 96.1 ± 8.5 GPa for the aggregate phase. The aggregate particles were assumed to be isotropic, and the Young's modulus of the aggregate particles was found using the constitutive relationship

$$M = \left[\frac{1-\nu^2}{E} + \frac{1-\nu_s^2}{E_s} \right]^{-1} \tag{7.2}$$

where M is the indentation modulus, E and ν are the Young's modulus and Poisson's ratio of the indented material, respectively, and E_s and ν_s are the Young's modulus and Poisson's ratio of the indentation stylus. The Poisson's ratio of the aggregate particles ν was assumed to be 0.16 [171], and for a diamond tipped Berkovich stylus, E_s and ν_s are 1140 GPa and 0.07, respectively [143]. The resulting Young's modulus for the aggregate grains was calculated to be 102.2 ± 8.4 GPa, and the mean was assigned to all the pixels in the phase maps associated with the aggregate phase.

The Young's modulus of the binding phase was determined in two different ways. In the first method, microindentation was used to determine the Young's modulus of each sample's binding phase, as was done for the aggregate phase. Between 8 and 10 indents were conducted on the binding phase for each sample, and the corresponding material Young's moduli were calculated for each sample using the measured indentation modulus and the constitutive equation (Eqn. 7.2), for which the Poisson's ratio of the binding phase, ν, was taken to be 0.29. The results are shown for each of the seven samples in Table 7.2.

The second way in which the Young's modulus of the binding phase was determined was by using the compression testing result for a cylinder of hardened cement paste. Ordinary Portland cement paste was mixed, molded, and left to cure under

Sample	Indentation Young's Modulus [GPa]	Material Young's Modulus [GPa]
VA-15	31.5 ± 3.2	29.6 ± 3.1
VA-10	27.0 ± 4.8	25.3 ± 4.6
VA-05	24.8 ± 3.7	23.2 ± 3.5
VA-00	34.6 ± 7.6	32.7 ± 7.4
OPC-175	32.8 ± 5.9	30.9 ± 5.7
OPC-075	36.0 ± 2.9	34.0 ± 2.8
OPC-000	34.6 ± 2.7	32.7 ± 2.6

Table 7.2: Indentation and material Young's moduli of the binding phase in each sample, as determined using microindentation. The standard deviations of the results are also provided.

water for 28 days prior to testing. The Young's modulus was found to be 15.6 ± 1.2 GPa. The discrepancy between the compression testing result and the microindentation measurements may be explained by considering porosity in the cement phase at length scales both shorter and longer than that of the microindentation volumes.

Each samples binding phase contains micro-flaws, such as cracks, small bubbles, and other sources of porosity, at scales smaller than the microindentation volumes and smaller than what is visible at the resolution at which the sample regions are being studied. Since the samples were all mounted in epoxy, it is possible that hardened epoxy could reinforce these empty spaces and interconnected voids, thereby stiffening the binding phase, and as such, cause the microindentation-obtained Young's modulus measurements to overestimate the true Young's moduli of the binding phase. This is supported by inspection of the SEM-EDS element maps that show that visible void space is associated with relatively high concentrations of Cl, which is a component of epoxy resin.

There are also many irregularities that lead to porosity at scales greater than that of the indentation volumes in hardened cement paste, both with and without the partial substitution of OPC with volcanic ash. During sample preparation, small bubbles inevitably remain in the cement paste and mortar mixtures, and cracks may form during curing. Such features are captured in the model when they are visible in the BS-SEM images, but the binding phase is selectively indented away from these features in order to avoid issues during testing, such as cracking, that would com-

promise the microindentation measurements. These result in the addition of void space that would not be captured in the indentation volumes and would therefore not be reflected in the elastic properties computed using the indentation moduli. As such, the average Young's moduli obtained using microindentation for the binding phases of each sample, which ranged from 23.2 - 39.2 GPa, were significantly higher than the value obtained through the compression testing of a cylinder of hardened cement paste (15.6 GPa), which provides a lower bound value considering all of the microstructure attributes being omitted by a local indentation approach.

Sand grains, on the other hand, are typically comprised of silicate minerals, such as quartz, feldspar, and mica. Although they may still have porosity that would not be captured in microindentation volumes, the extent to which the sand grains would be porous is less extensive than that of cement paste. As such, the average aggregate Young's modulus computed using the indentation moduli (102.2 GPa) was closer in value to the expected Young's modulus of quartz (97 GPa) [172].

The pore space was assigned a comparatively very small stiffness of 10^{-6} GPa and an arbitrary Poisson's ratio of 0.33. In order to address the interfacial transition zone (ITZ) between the aggregate phase and the binding phase, which is typically associated with increased porosity, and therefore reduced stiffness and strength [19], parametric modeling of the ITZ was conducted. For these simulations, the interfaces between the aggregate phase and the binding phase were assigned a Young's modulus that was 25%, 50%, or 75% of that of the binding phase of that sample. The Poisson's ratio of the interfaces was taken to be the same as that of the binding phase, 0.29.

It has been previously shown that whereas 3D modeling was necessary to predict non-linear behavior, such as fatigue life, fracture toughness, and strain to failure in particle-reinforced aluminum, 2D models were able to predict the same effective elastic properties as 3D models [117]. As such, the resulting maps of elastic properties were then used to generate 2D finite element models, and boundary conditions were set to meet the conditions for two types of elastic deformations: uniaxial compression and pure shear.

7.1.5 Finite element analysis

Custom MATLAB scripts were written to combine the phase maps with the pore space maps and mechanics data and generate input files for the finite element simulations that were carried out in Abaqus/CAE 2017.

Uniaxial compression simulations

For the case of uniaxial compression, the base was pinned in the x- and y-directions at the lower left node, and a roller constraint that limited movement to the x-direction was applied to all the other nodes along the base. A uniform displacement was applied to the top surface by applying a displacement, Δ, to the top left node in the negative y-direction and adding an equation constraint to the top row of nodes. By constraining all the other nodes along the top surface to the same motion in the y-direction as the top left node, the reaction forces along the top surface are summed at the top left node, thereby simplifying the analysis of the results. The boundary conditions are visualized in the schematic in Fig. 7-3A. The reaction force, RF, at the top left node was used to compute the Young's modulus as follows:

$$E = \frac{\sigma_y}{\epsilon_y} = \frac{RF}{d \times L_x} \times \frac{L_y}{\Delta} \tag{7.3}$$

where E is the effective Young's modulus of the model, σ_y and ϵ_y are the stress and strain, respectively, in the y-direction, L_x is the width of the sample area in the x-direction, L_y is the height of the sample area in the y-direction, and d is the depth of the sample into the page. Since the sample area is square, $L_x = L_y$, and since the model is planar with unit depth, $d = 1$. This simplifies Eqn. 7.3 to

$$E = \frac{RF}{\Delta} \tag{7.4}$$

Two uniaxial compression simulations were conducted for each finite element model corresponding to a sample area. First, it was conducted as described to measure the effective Young's modulus in the y-direction, E_y. Secondly, the finite element model was rotated 90°about the x-axis, and the simulation was again conducted as

described to measure the effective Young's modulus in the orthogonal direction to obtain E_x. This was done to confirm the assumption of sample isotropy, and the effective Young's modulus for each model was taken to be the average of E_x and E_y.

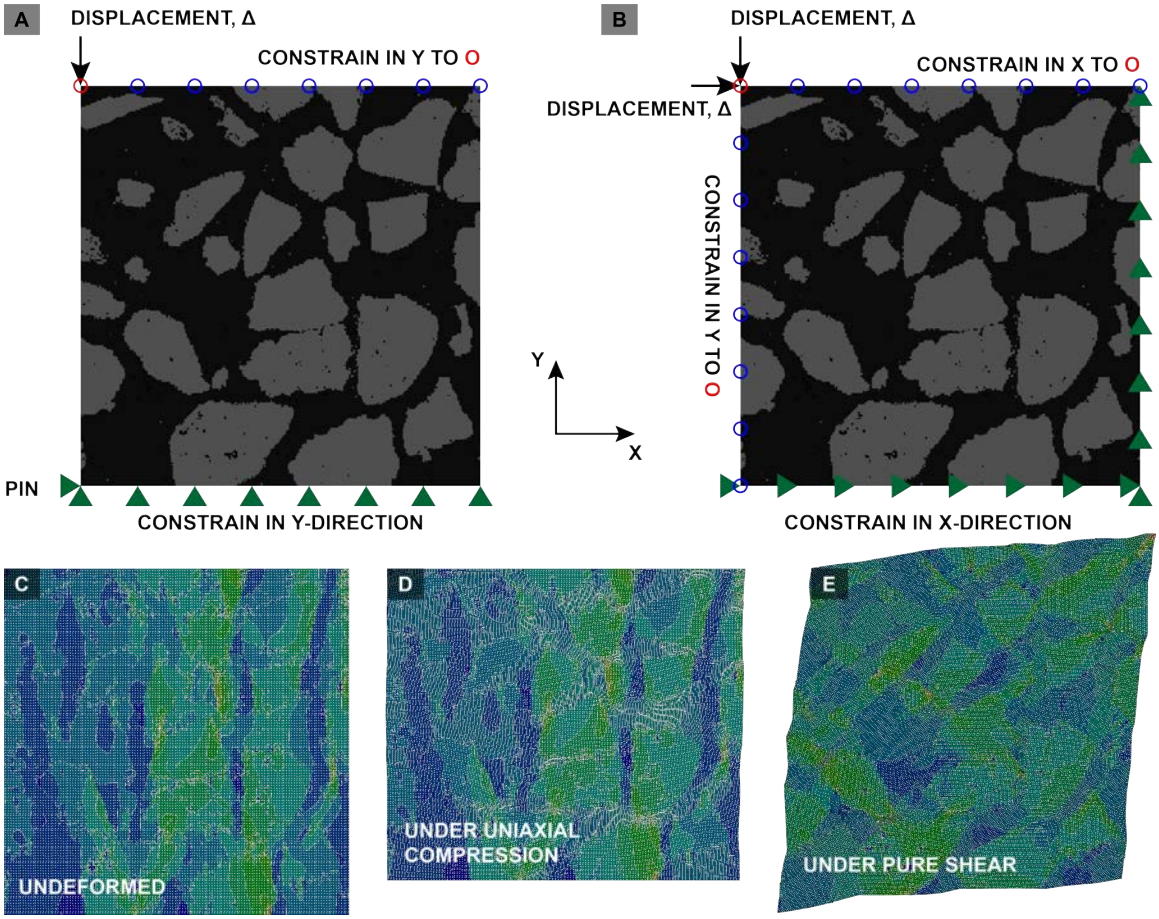

Figure 7-3: **Boundary conditions used in the simulations for uniaxial compression and pure shear.** The boundary conditions and applied deformation(s) used to simulate **A**: uniaxial compression and **B**: pure shear. The von Mises stress map throughout the model following uniaxial compression is shown overlaid onto **C**: the undeformed finite element model and **D**: the deformed finite element model. **E**: The von Mises stress map is shown overlaid onto the finite element model in its deformed state after pure shear deformation.

Pure shear simulations

For the case of pure shear, the lower surface was constrained to move only in the y-direction, and the right surface was constrained to move only in the x-direction. A uniform shear displacement was applied to the top surface by applying a displacement,

Δ, in the x-direction to the top left node and using an equation constraint to constrain all the other nodes along the top surface to the same motion in the x-direction as that node. A uniform shear displacement was applied to the left surface by applying a displacement, Δ, in the negative y-direction to the top left node and using an equation constraint to constrain all the other nodes along the left surface to the same motion in the y-direction as that node. Due to the presence of the equation constraints, the reaction forces along the top and left surfaces were summed at the top left node as RF_x and RF_y, respectively, which simplified the analysis. The boundary conditions are visualized in the schematic in Fig. 7-3B. The shear modulus of the mortar sample was then computed as follows

$$G = \frac{\tau_{xy}}{\gamma_{xy}} = \frac{RF_x}{d \times L_x} \times \frac{L_y}{2 \times \Delta} = \frac{RF_y}{d \times L_y} \times \frac{L_x}{2 \times \Delta} \tag{7.5}$$

where τ_{xy} and γ_{xy} are the shear stress and shear strain, respectively. Since $L_x = L_y$ and $d = 1$, the expression simplifies to

$$G = \frac{RF_x}{2 \times \Delta} = \frac{RF_y}{2 \times \Delta} \tag{7.6}$$

The Poisson's ratio may then be computed using the constitutive equation relating shear stress and shear strain in the xy-plane for materials that are transversely isotropic in that plane:

$$G = \frac{\tau_{xy}}{\gamma_{xy}} = \frac{\tau_{xy}}{2\epsilon_{xy}} = \frac{E}{2(1+\nu)} \tag{7.7}$$

7.1.6 Finite element homogenization results

Uniaxial compression and pure shear simulations were conducted for all sample areas that were characterized using quantitative SEM-EDS element mapping, and the means and standard deviations of the Young's moduli and shear moduli were calculated using the simulation results for each cement or mortar sample. The average Young's moduli, computed by averaging E_x and E_y for each finite element model, are shown in Fig. 7-4A and Fig. 7-4C, and the shear moduli, computed using the results

of the pure shear simulations, are shown in Fig. 7-4B and Fig. 7-4D. For all of the sample regions, E_x and E_y were similar; on average, they differed by 0.21 ± 1.24 GPa for the data presented in Fig. 7-4A and by 0.14 ± 1.42 GPa for the data presented in Fig. 7-4C, which supports the assumption that the samples are isotropic in the x-y plane at the scale at which the sample regions are being observed.

In Fig. 7-4A and Fig. 7-4B, the results are shown for the finite element models for which the binding phase elastic properties were determined using microindentation. Fig. 7-4C and Fig. 7-4D show the results for the models in which the Young's modulus of the binding phase was taken to be the stiffness of hardened cement paste as obtained through laboratory compression testing, that is E_{HCP}^{EXP}= 15.6 GPa. In all four plots, the experimental results for the Young's modulus of each sample (reported in Table 7.1) or the calculated experimental results for the shear modulus of each sample are shown in yellow.

The results show that the simulation results match the laboratory compression testing results more closely when the pore space, obtained through BS-SEM image segmentation, is accounted for. Furthermore, the results show that when E_{HCP}^{EXP} is used for the Young's modulus of the binding phase, the simulation results match the experimental results more closely than when the binding phase properties are obtained using microindentation. Although the microindentation data overestimates the stiffnesses of the binding phases for the reasons previously described, the simulation results presented in Fig. 7-4A and Fig. 7-4B successfully replicate the trends that are seen in the experimental results for the different sample mixtures. Moreover, when E_{HCP}^{EXP}, which captures the porosity that is not represented by the indentation data, is used, the simulation results show close quantitative agreement with the experimental results, further illustrating the utility of using the true microstructures of the mortar samples for modeling.

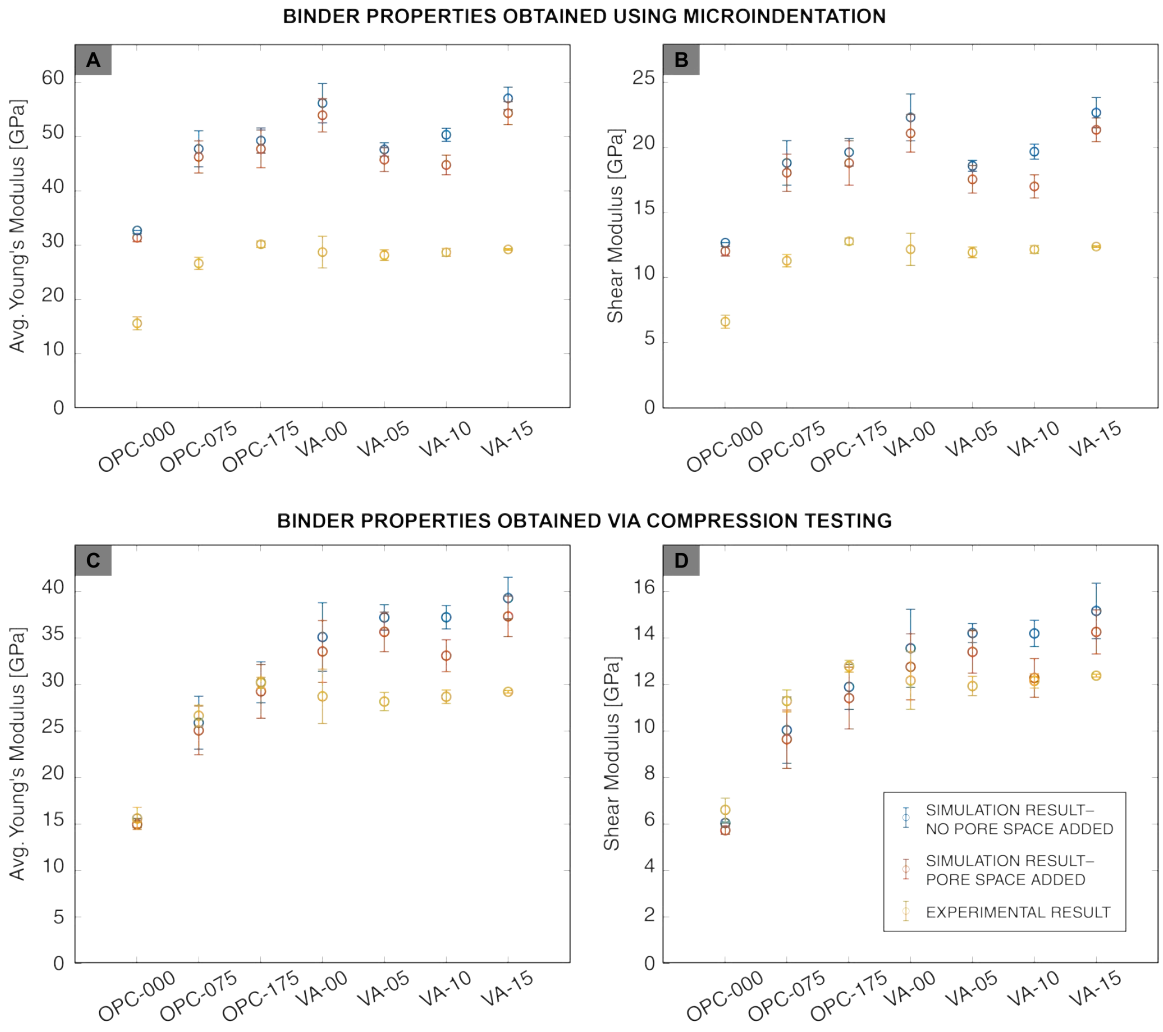

Figure 7-4: **Effective Young's moduli and shear moduli for each sample as determined through finite element analysis.** Each plot shows the experimental result as obtained using compression testing along with the simulation result both with and without the addition of pore space, the distribution of which was determined by segmenting the BS-SEM images. Results are shown for **A**: the average effective Young's modulus and **B**: the effective shear modulus of the models in the which the Young's modulus of each sample's binding phase was determined using microindentation, and **C**: the average effective Young's modulus and **D**: the effective shear modulus for which the Young's modulus of the binding phase of each sample was taken to be E_{HCP}^{EXP}.

7.1.7 Parametric modeling of the effect of aggregate-binding phase interfaces

In order to determine the effect of the aggregate-binding phase interfaces on the effective moduli of the cement and mortar samples, a parametric model of the interfaces

was implemented. After computationally selecting the pixels that lay along the interfaces between the aggregate particles and the binding phase, the Young's modulus at those pixels was set to be a factor (0.25, 0.50, or 0.75) multiplied by the Young's modulus of the binding phase, reflecting the increased porosity and therefore reduced stiffness of the binding phase at the ITZ.

The simulation results are shown along with the experimental results for the cases in which the Young's moduli of the binding phases were determined using microindentation (Fig. 7-5A and Fig. 7-5B) and for the cases in which it was set to E_{HCP}^{EXP} (Fig. 7-5C and Fig. 7-5D). Fig. 7-5A and Fig. 7-5C show the finite element results without the addition of void space, that is for a three-phase composite consisting of the aggregate phase, the binding phase, and interfaces. Fig. 7-5B and Fig. 7-5D show the finite element results for the models in which void space has been added, that is for a four-phase composite, consisting of the aggregate phase, the binding phase, interfaces, and void space.

Fig. 7-5A and Fig. 7-5B show that regardless of the interface factor, all the simulation results continue to overestimate the experimental values for the effective Young's moduli of the samples, due to the microindentation data consistently and significantly overestimating the true stiffnesses of the binding phases. However, the data shows that reducing the stiffness of the binder at the aggregate-binder interface has a measurable effect on the effective stiffnesses of the models, with an interface factor of 25% causing a reduction in the effective average Young's modulus from 12.7-22.8%, depending on the sand-to-cement ratio of the sample.

This considerable effect of reducing the binding phase stiffness at the aggregate-binder interfaces is also seen in Fig. 7-5C and Fig. 7-5D, which show the results of the parametric interface modeling when the binding phase stiffness is set to E_{HCP}^{EXP}. These simulation results show much better agreement with the experimental values, and they indicate that for samples VA-00, VA-05, VA-10, and VA-15, the experimental results mostly lay between the simulation results for interface factors of 50% and 25%, with the experimental results closer to the simulations results for an interface factor of 25% when the visible void space has not been accounted for, but closer to the simulation

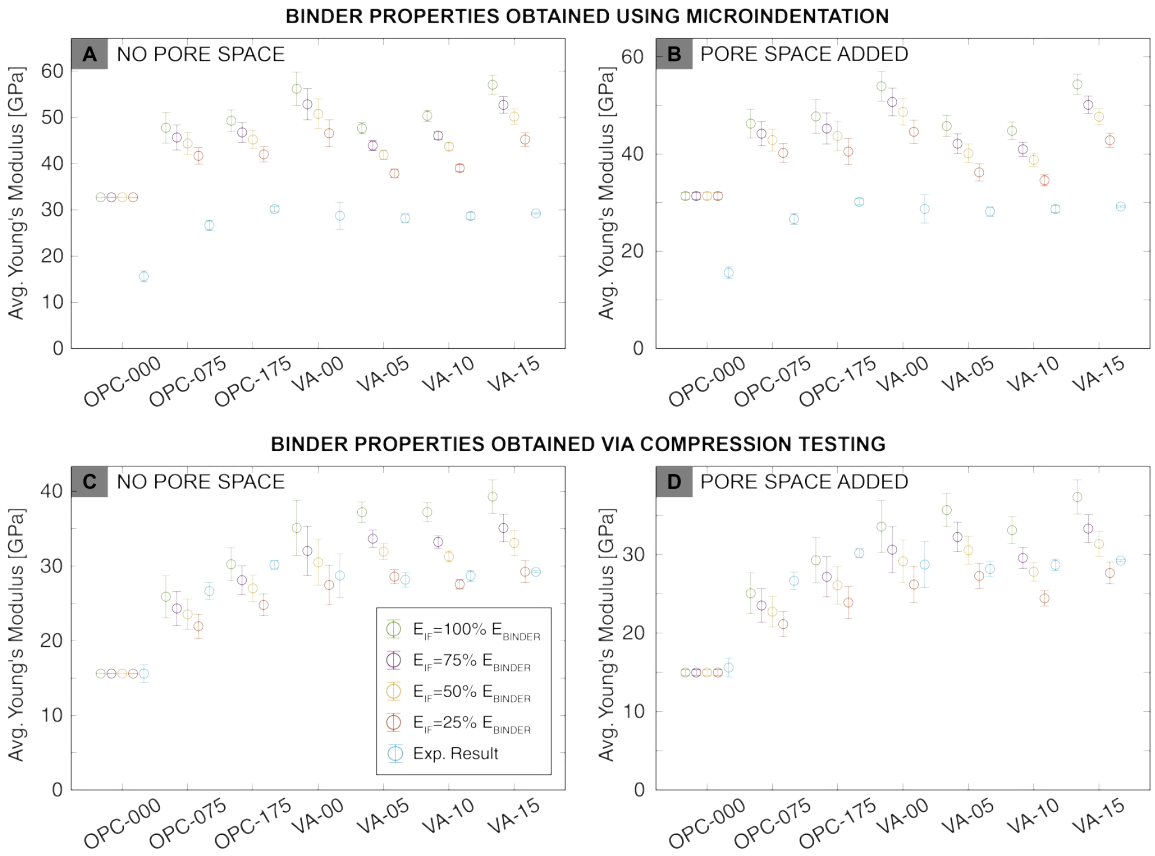

Figure 7-5: **Parametric study of the effect of aggregate-binding phase interfaces on the average effective Young's moduli of cement and mortar samples.** Each plot shows the average effective Young's moduli of each finite element model with aggregate-binding phase interfaces that are 25%, 50%, 75%, and 100% as stiff as the binding phase and the experimental measurements of the Young's moduli of each sample as determined using compression testing. Results are shown for the models in which the binding phase stiffness was determined using microindentation **A**: without the addition of pore space and **B**: with the addition of pore space, and for the models in which the binding phase stiffness was set to E_{HCP}^{EXP}, again **C**: without the addition of pore space and **D**: with the addition of pore space.

results for an interface factor of 50% when the void space from the BS-SEM images has been added to the models. For samples OPC-175 and OPC-075, however, the perfect interface assumption resulted in the simulation results most closely matching the experimental results. Due to the difficulty in knowing the true stiffness of the ITZ, which is highly heterogeneous and has no discrete physical boundaries, and in understanding the bonding between the aggregate grains and the binding phase, it is challenging to choose a specific stiffness for the pixels along the aggregate-binder

interface. By modeling a wide range of possibilities, it becomes possible to observe how the potential range of differences at the ITZ affects the effective stiffnesses of the models.

7.1.8 Validation of effective Young's modulus estimates through comparison with theoretical bounds

In order to confirm the validity of the simulation results, they were compared with the theoretical Voigt upper bounds and Reuss lower bounds for the estimates of the effective Young's moduli of the models. The bounds were calculated using the volume fractions of each of the phases present in each mapped sample region, which were obtained by counting the pixels associated with each phase. When considering a fiber-matrix composite, the Voigt upper bound corresponds to the case of axial loading, that is in the direction of the orientation of the fibers, and is computed using the rule of mixtures:

$$E_{composite} = \sum_{i=1}^{n} f_i E_i \tag{7.8}$$

where f_i and E_i are the volume fraction and the local Young's modulus of each of the n constituents, respectively. On the other hand, the Reuss lower bound corresponds to the case of transverse loading, that is in the direction orthogonal to the orientation of the fibers, and this bound is computed using the inverse rule of mixtures:

$$\frac{1}{E_{composite}} = \sum_{i=1}^{n} \frac{f_i}{E_i} \tag{7.9}$$

For other loading directions and other composite geometries, the true effective Young's modulus lies between these bounds, but when the constituents have notably different Young's moduli, for example in the case of porous mortars, in which the Young's modulus is effectively zero for the void space but is comparatively very large for the aggregate phase, these bounds can be wide. The upper-lower bound ranges

for each sample are shown along with the simulation and experimental results for the cases in which pore space is added and the interfaces are assumed to be perfect (i.e. interface factor = 1) in Fig. 7-6. Fig. 7-6A shows the bounds and results for the case in which the binding phase Young's moduli were obtained via microindentation, and Fig. 7-6B shows the bounds and results for the case in which E_{HCP}^{EXP} was used. In the case shown in Fig. 7-6A, it is shown that although the simulation results significantly overestimate the experimentally obtained effective Young's moduli, they provide much closer estimates than the rule-of-mixtures estimates. Fig. 7-6B shows that when E_{HCP}^{EXP} is used, the bounds are narrowed and the rule-of-mixtures estimates are more accurate than they are in Fig. 7-6A, but the finite element simulation results match the experimental results even more closely.

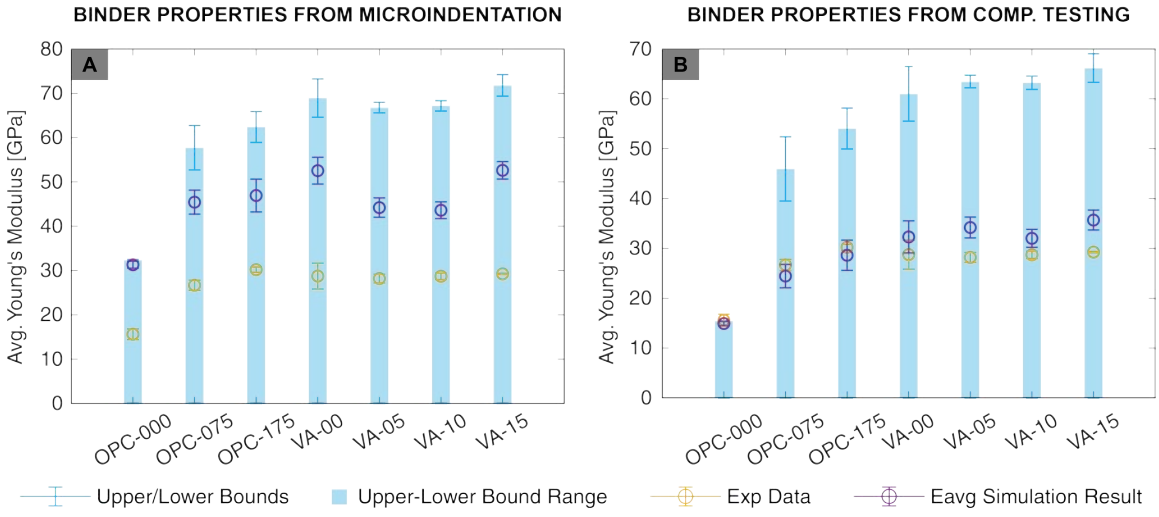

Figure 7-6: **Voigt upper bound-Reuss lower bound ranges shown along with finite element simulation estimates and experimental measurements for the effective Young's modulus of each sample.** Simulation results and bounds correspond to the cases in which pore space is added and the interfaces are assumed to be perfect. The blue error bars show the standard deviations of the bounds calculated using the various sample regions mapped for each mortar mixture. Results are shown for cases **A**: in which the binding phase Young's moduli were determined using microindentation and **B**: in which the binding phase Young's modulus was taken to be E_{HCP}^{EXP}.

7.2 Chemomechanical homogenization of Privernum mortar sample

Although the framework presented in this chapter was applied to the study of modern cementitious materials, it has the potential to be applied to composite materials in general. To demonstrate this, it was used to estimate the elastic properties of a mortar sample from the Privernum archaeological area (previously presented in Fig. 4-8).

7.2.1 Phase mapping and identification using SEM-EDS

In the clustering result presented in Fig. 4-8, it was shown that the optimal number of clusters was 7. However, in an attempt to separate the Fe-rich grain (bright grain on the right edge of the map) from rest of the purple phase previously shown in Fig. 4-8F-G, the clustering result showing nine phases was used. The nine-phase map along with the corresponding Ca-Si-Al ternary diagram and BS-SEM image is presented in Fig. 7-7.

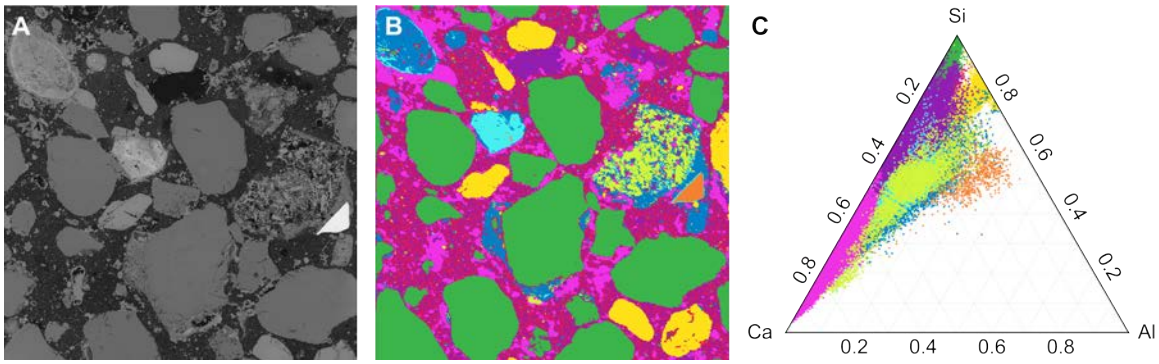

Figure 7-7: **Nine-phase k-means clustering result for the cross-section of a sample of ancient Roman mortar from the Privernum archaeological area** **A**: BS-SEM image, **B**: spatial distribution of clusters, and **C**: their positions on Ca-Si-Al ternary axes.

In order to determine the identities of each of the nine phases, their elemental ratios were studied. The atomic percentage of each of the elements present in various regions throughout the mapped regions (Fig. 7-8) is presented in Table 7.3. Due to the proximity of the green phase to the Si vertex of the ternary plot, it was deduced

that it would be siliceous sand (potentially a combination of the polymorphs of SiO_2, mostly quartz). Given the observed elemental ratios of the yellow phase, it was determined to be potassium feldspar [$KAlSi_3O_8$]. The fuschia phase, due to its very high Ca-content, was determined to be calcite [$CaCO_3$], which has been previously identified in the Privernum mortar samples through Raman microscopy [67]. The high Fe-content of the orange phase suggests that it is an iron-rich mineral, such as magnetite [Fe_3O_4] or hematite [Fe_2O_3].

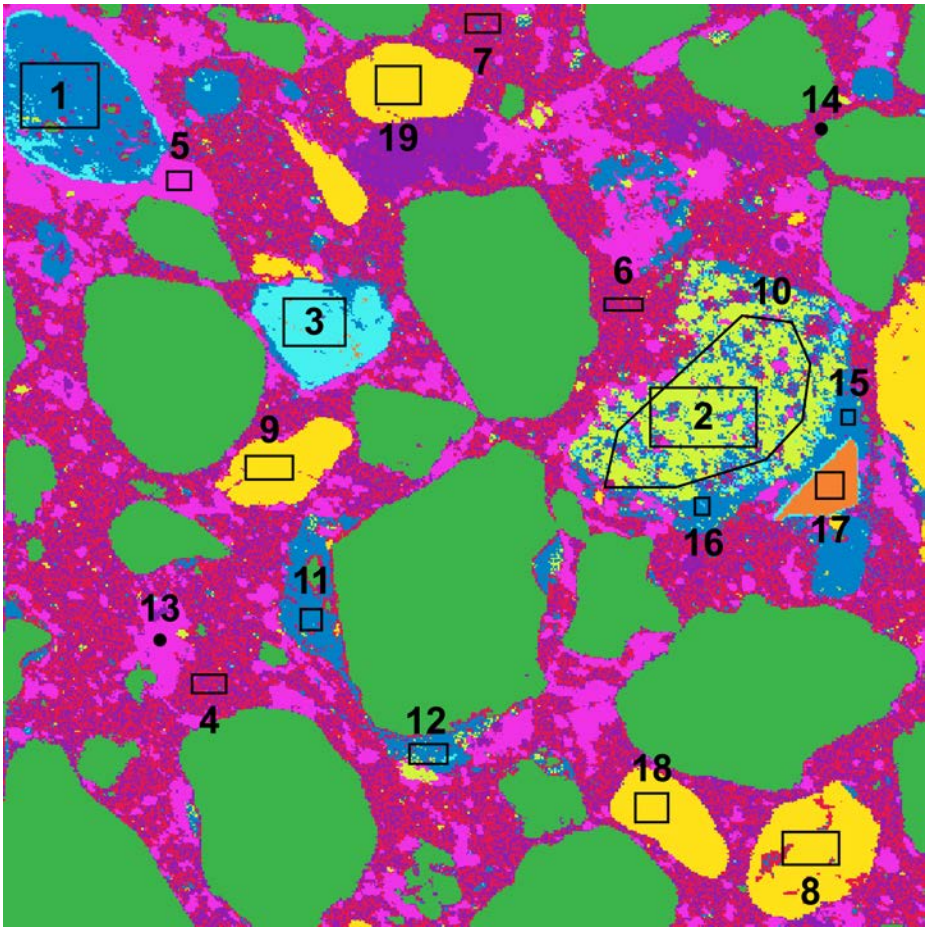

Figure 7-8: **Phase map showing regions for which quantitative element data was collected.** Quantitative data for entire map and each numbered region are presented in Table 7.3.

The phases colored blue, cyan, and lime green were determined to be scoria, due to their appearance in the BS-SEM image (Fig. 4-8 and Fig. 7-7) and their complex elemental compositions, which include Mg, Al, Si, Ca, Fe, and Mn. Scoria is a

Element	C	O	Na	Mg	Al	Si	P	S	Cl	K	Ca	Ti	Mn	Fe
Map	43.65	37.89	0	0.1	1.09	12.92	0	0	0.24	0.31	2.9	0.02	0.06	0.82
1	0	61.5	0	0.5	6.02	15.03	0	0	0	0.4	6.75	0.27	2.74	6.78
2	42.77	34.54	0	2.09	1.97	8.13	0.03	0	0.21	0.27	6.27	0.23	0.02	3.47
3	0	58.67	0	0.32	4.67	12.32	0.15	0	0	0.24	6.04	0.27	0.35	16.97
4	64.53	24.99	0	0.16	1.07	5.79	0	0	0.76	0.11	2.3	0.02	0.01	0.26
5	27.53	48.65	0	0	0.17	2.71	0	0	0	0.04	20.61	0	0.02	0.28
6	64.76	24.43	0	0.2	1.22	5.82	0	0	0.71	0.16	2.23	0.04	0.03	0.4
7	60.48	27.13	0	0.18	1.54	6.57	0	0	0.67	0.17	2.72	0.03	0.01	0.48
8	19.46	49.01	0.71	0	5.86	19.12	0	0	0	5.27	0.48	0.01	0.01	0.06
9	26.61	44.54	0.5	0	5.35	17.51	0	0	0	4.56	0.7	0.07	0.01	0.14
10	47.02	32.29	0	1.72	1.76	7.59	0.03	0	0.27	0.19	5.67	0.2	0.06	3.19
11	28.83	46.93	0	0.64	4.15	10.51	0	0	0.04	0.36	5.36	0.38	0.07	2.72
12	34.53	42.9	0	0.91	3.77	9.84	0	0	0.13	0.33	4.81	0.16	0.05	2.59
13	29.6	47.07	0	0	0	2.9	0	0	0	0	20.37	0.06	0	0
14	52.69	31.57	0	0.18	0.99	6.82	0	0.04	0.64	0.45	5.9	0.14	0	0.57
15	29.21	45.63	0	0.77	4.62	10.26	0	0	0.06	0.58	5.48	0.14	0.04	3.21
16	32.61	43.37	0	0.86	3.99	9.68	0	0	0.06	0.31	5.05	0.2	0.07	3.79
17	18.05	38.47	0	1.14	2.22	3.34	0	0	0	0	0.73	1.48	0.09	34.49
18	0	57.68	0.13	0	7.7	25.92	0	0	0	7.76	0.65	0.05	0.02	0.09
19	26.84	44.29	0.63	0	5.54	17.24	0	0	0	4.54	0.68	0.07	0.01	0.13

Table 7.3: Quantitative element data in atomic percent for regions shown in Fig. 7-8.

highly vesicular volcanic rock that is higher in density than pumice and is of varying chemical composition. The Young's modulus of scoria was taken from [173], in which the material properties of a large collection of scoria samples from the Mount Fuji area were measured using triaxial compression. Like Mount Fuji, Mount Vesuvius, which is only 80 miles from Privernum and a likely source of the volcanic ash used, is a stratovolcano that erupts similarly. Therefore, it was assumed that the scoria in the Privernum sample would have similar elastic properties as the scoria from the Mount Fuji area. Since scoria sometimes contains crystals, as shown near markers 2, 11, 12, 10, 15, and 16 in Fig. 7-8, which would increase its Young's modulus, the lowest Young's modulus for the collection of small-grain scoria samples in [173] was used.

7.2.2 Finite element modeling

The Young's moduli and Poisson's ratios for all the phases shown in Fig. 7-8 that were used to generate the finite element model are presented in Table 7.4. For the binding phase, the average of the three sources cited was used.

The finite element model was then subjected to uniaxial compression in orthogo-

Color	Phase	Young's Modulus, E [GPa]	Poisson's Ratio, ν
deep pink/red	binder	3.40 [157, 25, 13]	0.20 [5]
green	siliceous sand	70.00 [5]	0.17 [5]
yellow	feldspar	85.00 [174]	0.17 (matched sand)
blue	scoria	18.23 [173]	0.28
orange	magnetite	223.00 [175]	0.37 [175]
purple	resin-filled pores (assigned binder)	3.40	0.20
cyan	scoria	18.23	0.28
fuschia	calcite	85.19 [174]	0.32 [174]
lime green	scoria	18.23	0.28

Table 7.4: Young's moduli and Poisson's ratios for each of the identified phases used to generate Privernum sample finite element model. Colors correspond to the phase colors in Figs. 7-7 and 7-8. The Poisson's ratio of scoria was taken to be 0.28.

Property	Value
Young's Modulus, x-Direction [GPa]	13.45
Young's Modulus, y-Direction [GPa]	12.11
Average Young's Modulus [GPa]	12.78
Shear Modulus [GPa]	4.93
Poisson's Ratio	0.30

Table 7.5: Finite element estimates for the Young's modulus and Poisson's ratio of the Privernum Roman mortar sample.

nal directions and pure shear deformation. The resulting estimates for the Young's modulus in orthogonal directions, the average of those Young's moduli, and the shear modulus are presented in Table. 7.5. The Poisson's ratio, which was computed using the average Young's modulus and the shear modulus using Eqn. 7.1, is also presented in Table. 7.5.

7.3 Further Discussion

7.3.1 On the selection of appropriate composites for this framework

The results of this homogenization framework showed that when microindentation-obtained values are used with the phase maps to computationally homogenize the samples, the simulation results provide better estimates of the experimentally ob-

tained effective Young's moduli than the rule-of-mixtures (Voigt model) estimates. However, these simulation results still significantly overestimate the experimentally obtained effective moduli, since the microindentation data overestimates the true Young's moduli of the binding phases. That the material moduli of the aggregate phases computed using microindentation data match the theoretical values for silicate minerals such as quartz more closely suggests that when microindentation-obtained values are used, the framework is better suited for materials that have constituents that are both homogeneous at scales similar to that of the indentation volumes and unlikely to contained interconnected pores at scales smaller than what is observed that may become filled with the mounting medium during sample preparation.

Cementitious composites, such as OPC-based mortars, are incredibly complex and highly heterogeneous, both chemically and mechanically. The good quantitative agreement between the results of this chemomechanical framework and the experimental data indicates that this framework would be expected to work for a multitude of other systems, many of which would be simpler than OPC-based mortars. This framework would also be particularly useful in the study of composites with constituents of known elastic properties, since the estimates generated using the framework matched the experimentally obtained results most closely when E_{HCP}^{EXP} was used for the stiffness of the binding phase. One such application could be in the study of multi-mineral rocks, where the phases could be mapped using quantitative SEM-EDS element mapping and k-means clustering, then identified using high-resolution vibrational spectroscopic techniques, such as Raman or infrared microscopy. The known elastic properties of the identified minerals could then be assigned to the mapped phases prior to the generation of finite element models and computational homogenization.

7.4 Summary and Conclusions

In this work, a chemomechanical homogenization framework that may be generally applied to composites made up of chemically distinct phases was presented. Quan-

titative SEM-EDS data was used with k-means clustering to map the constitutive phases present in various cement and mortar samples, and BS-SEM image segmentation was used to map the distribution of visible void space present. These phase maps were then converted to linear elastic finite element models by determining the Young's modulus of the aggregate phase using microindentation and by determining the Young's modulus of the binding phase of each sample in two ways: (1) using microindentation and (2) using the Young's modulus of a sample of hardened cement paste, which was obtained through compression testing. The models created using the latter method showed better agreement with experimental results, likely due to the presence of porosity, cracks and other defects present in the binding phases at scales greater than that of the indentation volumes, but the results of both methods provided better estimates than an analytical rule-of-mixtures estimates. Parametric modeling of the aggregate-binder interfaces showed that reducing the stiffness at these interfaces had a measurable impact on the effective elastic properties of the models. Finally, the framework was used to homogenize a sample of mortar from the Privernum archaeological area using phase properties from the literature. The framework presented in this work shows great potential, particularly in the study of composites that have constituents that are homogeneous at the scale of the microindentation volume, in the study of composites that have constituents of known elastic properties, in the design of new composite materials, and in the modeling of composite material properties apart from elasticity.

Chapter 8

Summary and Future Work

8.1 Summary of Contributions

8.1.1 Chemical characterization of ancient Roman mortar

In this thesis, a chemomechanical framework for the characterization and modeling of composite materials of unknown composition was presented. Three-dimensional surface confocal Raman microscopy was used along with multi-detector SEM-EDS to map the phases present both in the cross-sections on the fracture surface of samples of ancient Roman mortar obtained from the Privernum archaeological area. The results showed that the binding phase present on the fracture surface differs in elemental composition from the binding phase present throughout the cross-section. Since the samples would be expected to fracture along the weakest parts of the binding phase and the low-Al binding phase was found in the cross-section but not on the fracture surface, it was inferred that the low-Al component of the binder was of higher strength than the higher-Al binding phase components. Further investigation, perhaps through microindentation experiments, would be necessary to confirm this.

When the ratios of the three major elements of interest for cementitious materials: Ca, Si, and Al were plot on ternary axes, it was shown that data points from the mapped sample regions corresponding to unique phases, such as quartz aggregate and aluminosilicate aggregate, were present as clusters in the ternary diagrams. When

particular regions of the ternary plots were selected and plot onto the original mapped area, it could be seen that particular elemental ratios corresponded to distinguishable phases. Given this observation, the SEM-EDS data was partitioned using unsupervised learning. Fuzzy c-means clustering was used with quantitative SEM-EDS data to show the variation in chemistry within and around remnant lime clasts, which are often found in ancient Roman mortar and concrete samples.

The procedure for segmenting chemical images based on quantitative SEM-EDS data was then refined to make it suitable for quantifying heterogeneous materials of unknown composition in general. After excluding certain elements that are difficult to quantify reliably and normalizing the SEM-EDS data, k-means clustering was used to assign each pixel of the mapped regions to a chemically distinct phase. Model selection was then performed using the Calinski-Harabasz method, which determined the most likely number of phases present. This method of analysis is particularly useful in the study of highly heterogeneous materials of unknown composition since it (1) does not require that the phases present are known by the operator, as is necessary with supervised learning/classification techniques that have previously been used to map the phases present in hardened cement paste samples, and (2) does not require that the number of phases present be known *a priori*.

8.1.2 Identification of a unique production stream for the Dead Sea Scrolls

When generated for the same types of mortar samples, Ca-Si-Al ternary plots were similar in appearance due to the similar distributions of their data points; this observation was particularly useful in the study of the Dead Sea Scrolls. Na-S-Ca particles were identified on the surface of a fragment of the Temple Scroll, and upon further investigation with µXRF, SEM-EDS, FT-Raman, and confocal Raman microscopy, they were found to consist of a mixture of evaporitic salts. The hygroscopic nature of these evaporitic salts was critical, since it suggests that the parchment would be particularly sensitive to changes in or relatively high levels of humidity.

The chemistries of three other scroll fragments obtained from Cave 4 were compared to the chemistry of the Temple Scroll, which was obtained from Cave 11, using ternary diagrams, in which the elemental ratios of the three elements of interest (Na, S, Ca) were shown. The ternary plot for one of the scrolls was found to consist of a cluster of data points that extended between the theoretical positions for two of the evaporitic salts of interest: glauberite and thénardite. Upon further inspection of this scroll fragment using Raman microscropy, it was found to contain the evaporitic salts thénardite and gypsum. The presence of these salts—which do not match the sediments found on fragments that were laying on the cave floors—on multiple Dead Sea Scrolls suggests a previously unidentified production process, in which these salts were included. The fact that these salts are also not commonly found in the Dead Sea region introduces questions regarding the provenance of these scrolls, which remains the subject of future work.

8.1.3 Interfacing with mechanics for the elastic homogenization of modern and ancient cementitious materials

By combining the chemical data obtained using SEM-EDS with k-means clustering and model selection, it was possible to segment the large area, high resolution chemical maps into spatially resolved phases. It was demonstrated that when these phases were assigned elastic properties, which were obtained using microindentation or laboratory compression testing, the resulting high resolution maps of mechanical properties could be converted to finite element models that reflected the true microstructures of the mortar samples being studied. The finite element models were then used with uniaxial compression and pure shear simulations to perform computational homogenization and obtain estimates for the elastic properties for each of the samples studied. When the binding phase stiffness was obtained using compression testing, the porosity at scales both shorter and longer than the length scales of the microindents was captured, and the resulting estimates for the effective elastic properties of the mortar samples showed strong numerical agreement with the ex-

perimental compression testing data. The framework was then applied to an ancient Roman mortar sample from the Privernum archaeological area to estimate its elastic properties using phase properties from the literature.

This homogenization framework was primarily applied to mortars that were produced using ordinary Portland cement, and these mortars are notoriously highly heterogeneous across length scales, from the nanoscale to the centimeter-scale. Most composites of unknown composition would be simpler in structure and composition than OPC and ancient mortars, and as such, the framework would be expected to work well in the study of those materials as well. Furthermore, the phase maps were converted to linear elastic finite element models in this thesis as a proof of concept, but one could model other phenomena apart from elasticity. As long as there is a method for assigning the relevant properties to the pixels of the phase maps, this framework has the potential to model a wide range of material properties. Therefore, this framework should be considered to be a starting point for interfacing chemistry with material properties of interest in general.

8.2 Avenues for future work

8.2.1 For studying the effect of interventions on bulk properties

Once the chemomechanical framework presented in this thesis is applied to the homogenization of ancient Roman mortar, it may be applied repeatedly to observe the effect of various interventions before they are actually executed. There are many empirical equations relating concrete's elastic modulus to its compressive strength, with a universal equation having been proposed by the Architectural Institute of Japan (AIJ) [176]. As such, changes in stiffness induced by various intervention strategies, for example by filling pores with added material such as gypsum or epoxies, can be related to equivalent changes in strength. The efficacy of invasive interventions may therefore be more well-understood before they are actually applied.

8.2.2 In the design of bio-inspired composite materials

This framework also proved to be effective in detecting trends in and differences between the effective Young's moduli of the different types of samples, which suggests utility in the design of composites. With the use of finite element models, it is possible to quickly compare composites with constituents that vary in volume fractions, local elastic properties, and geometries. As an example, in the field of bio-inspired design, a biological composite could be used as a model material. After performing chemical characterization, phase mapping, and computational homogenization on the model material using this framework, the model could be altered in a number of different ways, such as in local phase properties or geometric arrangement, before performing homogenization again. In this workflow, it would be possible to quickly study the effects of these changes on the effective properties of the bio-inspired composite without the need for rapid prototyping or other forms of sample production, which would save time and cost in the design process.

Furthermore, current approaches for bio-inspired design, particularly when conducted in conjunction with rapid prototyping, involve using CAD to generate geometries that approximate the true geometries of composite materials. By using a chemical mapping technique with data clustering to obtain phase maps before using those phase maps to generate models, subtleties in the geometries of natural materials may be captured, and the effect of simplifying the true geometries may be carefully studied.

8.2.3 Modeling of non-linear mechanical behavior, non-mechanical behavior

Finally, the microstructural maps that are obtained by clustering the chemical data may be used to model phenomena besides elasticity. This study focused on obtaining the effective Young's moduli and shear moduli of cementitious composites, but other properties that may be studied using finite element analysis or other techniques include non-linear mechanical properties, such as strength and fracture, as

well as non-mechanical material properties, such as heat transfer. For some composite properties, it may be necessary to extend the model to three dimensions, but three-dimensional chemical data, such as 3D confocal micro X-ray fluorescence, could be used with this framework to obtain three-dimensional phase maps. The capabilities of the chosen modeling approach would be limited only by how well understood the relevant properties of the constituent phases are.

If this work were to be used to study the fracture resistance of concrete, which is of more relevant interest than elasticity in the modeling of modern cementitious materials, the models could be used with extended formulations of the finite element method, such as the continuum phase field model for fracture [177] or the extended finite element method (XFEM) [178], which address the continuity assumption made in traditional finite element modeling that does not hold in the case of fracture. Other avenues for the exploration of fracture resistance could involve the use of other recently developed discrete methods, such as lattice type fracture models [179] and potential-of-mean-force (PMF) approaches [180].

8.2.4 Extension to 3D through the use of random field models

Whereas 2D models tend to be sufficient for the elastic homogenization of isotropic materials, 3D models tend to be necessary for modeling non-linear phenomena, such as plasticity and fracture. 3D chemical characterization techniques, such as CT or µ-XRF, may be used, but these characterization methods tend to be costly or difficult to access. Previously, random field models have been generated using statistical information about the constituent phases of hardened cement paste samples obtained using nanoindentation grid mapping [143]. 3D random field models may be similarly generated for the mortar samples presented in Chapter 7 using the high resolution phase maps to obtain accurate statistical information. These 3D models may then be used with the finite element method or other techniques to more accurately model non-linear mechanical behavior.

Appendix A

Case study in cultural heritage: the freestanding multi-drum columns of Pompeii

In this chapter, a case study that highlights the need for mechanically characterizing ancient construction materials is presented. Here, the freestanding multi-drum columns of Pompeii are introduced in a study that focuses on structural stability. The study involved the numerical analysis of the geometries of the three columns and their constituent drums to predict (1) their most probable collapse mechanisms and (2) the equivalent lateral ground accelerations necessary to cause them. The results of the numerical analysis were then corroborated for two of the three columns of interest using 3D printed scale model collapse experiments. These results were then compared with seismic hazard maps to assess the risk of structural collapse in the next 50 years. Finally, material point method (MPM) models were then used to numerically predict the failure behavior of the capital drum of one of the columns under various ground-impact scenarios, which indicated catastrophic failure in all cases. This chapter demonstrates a generally applicable methodology for the study of historic masonry structures and the identification of failure modes that may be addressed in the design of preservation strategies, but they also illuminate a significant gap in our understanding of their behavior. For the MPM simulations, it was necessary to

use assumed mechanical properties since the true properties were unknown. Should we need to properly assess the true behavior of the drums in the event of collapse, it would be necessary to perform mechanical characterization to obtain their actual material properties.

A.1 Introduction

The city of Pompeii, likely founded by the Osci of Campania and Latium Novum in the 6th or 7th century BCE, was conquered by the Roman Empire in the 4th century BCE and became a Roman colony in the year 80 BCE. Due to its location in the Bay of Naples, Pompeii was a popular destination for wealthy Romans, and as such, was occupied by tens of thousands of people. In fact, it is believed that at the time of the catastrophic volcanic eruption of Mount Vesuvius in 79 CE, approximately 20,000 people occupied the city [181]. The resulting pyroclastic flow from Mount Vesuvius killed the occupants, and the city was buried under a total of approximately 25 m of tephra. The location of the city of Pompeii was, therefore, unknown for centuries until construction workmen repeatedly discovered evidence for the existence of a buried city throughout the 18th century. Upon the discovery of a dedicatory inscription, the buried city was identified as Pompeii [182], and intentional excavations led by the Spanish military engineer Rocque Joaquin de Alcubierre began in 1748.

Being buried under meters of pumice and volcanic ash restricted Pompeii's exposure to air and moisture, thus preserving the ruins for centuries. Since Pompeii's excavation, however, exposure to natural and man-made destructive conditions has rapidly increased the rate of deterioration of the ruins. The excavated site of Pompeii is now a major tourist attraction that spans over 3 square kilometers, but a dearth of funding and the scale of the ruins has led to difficulties in ensuring consistent sufficient maintenance, and the constant exposure of the structures to the elements and human interaction due to tourism has led to the rapid decline in their structural health [183]. The ruins of Pompeii provide a unique opportunity for data collection for cultural heritage research, because although they are approximately 2000 years

old, they have been well preserved for much of it, with the most significant deterioration only occurring over the last few centuries. Multiple structural collapses have inspired researchers and conservation scientists to intervene to protect the site, and in 2013, the European Union initiated a conservation project, titled The Great Pompeii Project, with the intention of conserving the rich cultural heritage in the site [184].

This work focuses on one type of structure found throughout Pompeii and many other cultural heritage sites around the world: the freestanding multi-drum column. A methodology for studying its stability and estimating the magnitude of seismic activity necessary to cause its collapse is presented. This methodology was applied to three freestanding multi-drum columns that are situated amongst the ruins of one of the oldest temples in Pompeii, the Tempio di Apollo, which dates back to the 8th or 7th century BCE (Fig. A-1). The Tempio di Apollo was redesigned in the 2nd century BCE and was damaged prior to the eruption of Mount Vesuvius during the Pompeii earthquake of 62 CE. At the time of the eruption in 79 CE, the temple was still under renovation. The three columns studied in this work are the Corinthian columns 1 and 2 (Fig. A-1B and Fig. A-1C), which were carved from tuff, and the Ionic column 3 (Fig. A-1D), which was used to support a sundial. Each of the columns is comprised of carved drums, which are held together by mortar.

The collapse of the freestanding column is considered here to be a purely geometric problem, resulting from kinematic instability and not from material failure. This can be assumed when the following three assumptions for the analysis of masonry structures are valid: (1) crushing failures are not likely due to the low average stresses present in the structure relative to the crushing capacity of the drums, (2) sliding failures are not likely due to the high coefficient of friction between the drums, and (3) the stresses in the structure are purely compressive—if there were tensile forces, the mortar would have failed since it has very little strength in tension [185, 186]. Such assumptions have been made in the determination of the safety of masonry arches under point loads and traveling loads [187, 188, 189] as well as stone spires and pinnacles [190, 191, 192].

A structure's risk of collapse is therefore related to its geometry and the ground

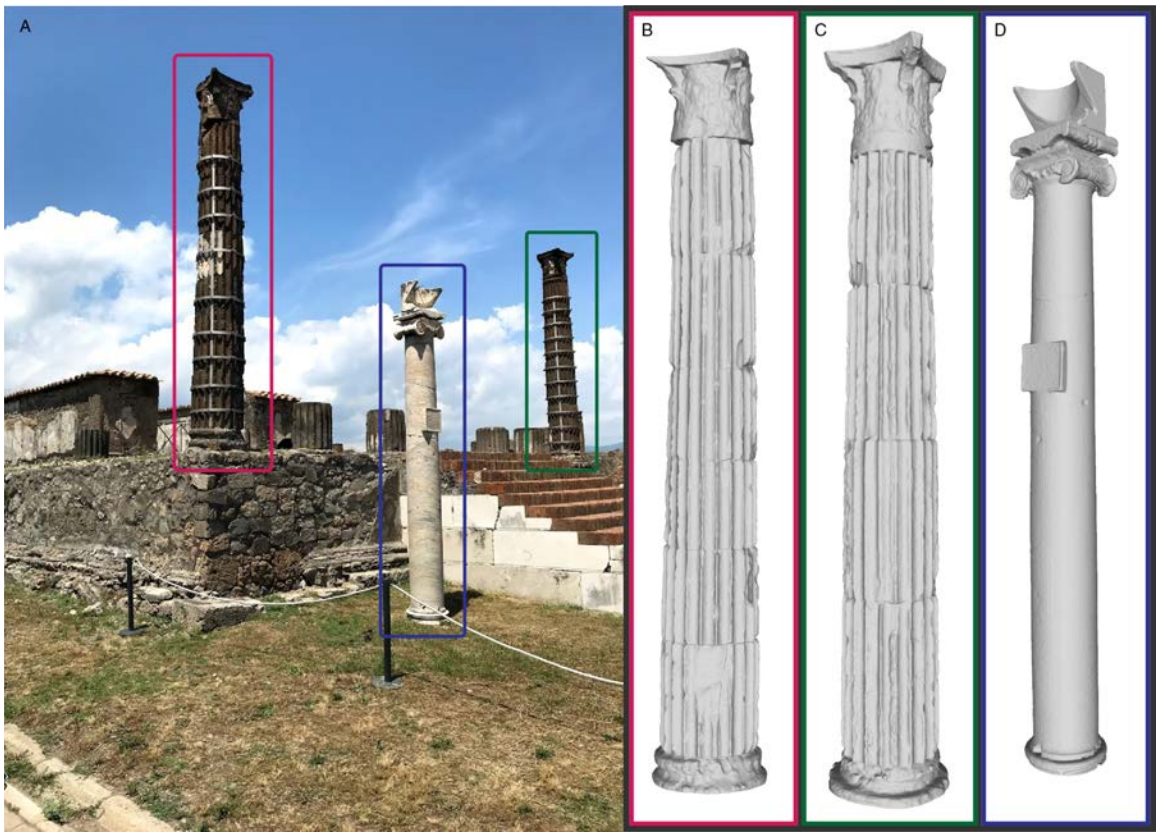

Figure A-1: **The three columns of interest from the Tempio di Apollo (Pompeii, Italy). A**: Photograph of the three columns in the Tempio di Apollo. 3D models of **B**: Column 1 (**A**, left). **C**: Column 2 (**A**, right). **D**: Column 3 (**A**, middle).

acceleration that may be experienced at its location. The freestanding column may be modeled as a set of stacked blocks that may be assumed to be rigid, since elastic deformation during collapse mechanism formation is negligible. The dynamic response of the rigid block has been extensively studied, starting with the modeling of tall slender structures [192], and the rocking response has been studied for freestanding rigid blocks under various types of forcing, including horizontal and/or vertical accelerations [193, 194], harmonic forcing [195, 196, 197], Gaussian white noise excitation [198], and cycloidal pulses [199].

The nonlinear equations of motion describing the dynamic behavior of a stack of two rigid blocks have been rigorously derived, and they show that the response modes of the system are poorly-conditioned, that is, small changes in input result in very large changes in the dynamic response [200, 201, 202]. Analytical solutions have also

been derived to describe the motion of rigid body assemblies, such as masonry arches, under dynamic forcing [203] and after the formation of a collapse mechanism [204]. Furthermore, numerical methods, including discrete element modeling (DEM), have also been used to study the responses of assemblies, such as freestanding columns and other complex masonry structures under dynamic forcing [205, 206, 207, 192, 208, 209, 210, 211].

Whereas in situ frequency response experiments have been used to evaluate the seismic behavior of ancient columns such as the Column of Trajan and the Column of Marcus Aurelius [212], scale model shake table experiments have been more commonly implemented to observe the dynamic response of rigid bodies and rigid body assemblies [213, 214]. However, applying this technique to real structures in a reliable way presents a number of challenges, one of the most significant of which is that small changes in the geometry or forcing could lead to large changes in the dynamic response [199, 197]. Furthermore, due to the wide range of reasons that could lead to ground acceleration, such as tectonic faults or the movement of magma, generating a representative dynamic forcing function to use with a model is difficult.

It has been previously shown that whereas the rocking of larger blocks is more susceptible to high-acceleration, short duration pulses, the toppling of smaller blocks, like those in the Pompeian columns of interest in this study, is more sensitive to the peak ground acceleration [215]. Since the value of interest is the horizontal ground acceleration that would lead to collapse and the aforementioned assumptions for geometrically analyzing masonry structures are valid for the freestanding columns of interest, it is possible to estimate the effects of lateral ground accelerations by using the equivalent static analysis: tilt analysis, i.e. the first order approximation of the true dynamic case [205, 206, 216, 217].

To verify the accuracy of the numerically obtained results, physical experiments using 3D printed gypsum scale models were performed. Scale model experiments are particularly valuable in studying the collapse of masonry structures with complex geometries where the collapse mechanism may be challenging to predict analytically or numerically, such as in the study of unreinforced masonry domes, vaults, arches

and buttresses [218, 219, 217]. Such experiments have even proven useful in identifying unexpected collapse modes that were unaccounted for in analysis models [220]. Whether the tilt analysis is conducted numerically or with the aid of scale models, the identified tilt angle that causes instability may be used to compute an estimate of the equivalent critical lateral ground acceleration that would lead to structural collapse [216].

The rich history of the Tempio di Apollo imparts unquantifiable value to the structures held within it, and as such the preservation of these structures is critical. To assess the extent of damage that could be sustained by the drums of the columns, the outcomes of a variety of collisions between them and other surfaces were studied using material point method (MPM) models [221]. This technique has previously been implemented to simulate snow [222], study hydraulic fracture in geomechanical problems [223], failure in soil slopes [224], and fracture and failure in brittle materials [225], as well as damage in aggregate materials [226]. The variety of applications of the technique made it a suitable choice to model the damage of the drums during collisions with both soil-like and rigid materials.

The methodology presented in this work has been applied to one particular type of historic structure, but modifications may be made as needed depending on the particular masonry structure of interest. The results of this methodology may be used to assess the level of risk of unreinforced masonry structures, prioritize interventions, which is of particular value for sites such as Pompeii which are responsible for a large number of valuable structures, and assess the efficacy of existing interventions.

A.2 Numerical predictions for collapse mechanisms and critical peak ground accelerations

A.2.1 Procedure

Three-dimensional scans of the multi-drum columns were collected, and the resulting models were divided into individual drums. The material from which the drums

were made was assumed to be isotropic and homogeneous, which is supported by the knowledge that they were carved from single blocks of tuff (at least for columns 1 and 2). Each drum's mesh was converted to a cloud of surface points, which were then used to complete the analysis. The centroid of each drum was found by: (1) removing the top and bottom surfaces of its surface point cloud, (2) grouping the remaining surface points into stacked layers by rounding their z-coordinates (parallel to the column's axis), (3) finding the centroid and area of each layer, then finally, (4) using the centroid and area of each layer to compute the centroid of the entire drum. Since the 3D models were dimensionless, the rounding parameters were dependent on the particular model being analyzed.

To find the centroid and area of a particular layer, the surface points throughout the x-y plane were sorted into clockwise order (clockwise about the average position of all the surface coordinates) then used with the standard equations for finding the area (Eqn. A.1) and centroid (Eqn. A.2 and Eqn. A.3) of an arbitrary non-self-intersecting closed polygon, where $x_n = x_0$ and $y_n = y_0$.

$$A = \frac{1}{2}\sum_{i=0}^{n-1}(x_i y_{i+1} - x_{i+1} y_i) \tag{A.1}$$

$$x_c = \frac{1}{6A}\sum_{i=0}^{n-1}(x_i + x_{i+1})(x_i y_{i+1} - x_{i+1} y_i) \tag{A.2}$$

$$y_c = \frac{1}{6A}\sum_{i=0}^{n-1}(y_i + y_{i+1})(x_i y_{i+1} - x_{i+1} y_i) \tag{A.3}$$

The z-coordinate of the centroid of the layer was taken to be the value to which the surface points were rounded. The thickness of each layer was found using the mid-z-coordinates between the centroid of each layer. The centroid of the drum, $r_{c,drum}$, was then found using the centroid, r_i, and volume, V_i, of each layer as:

$$r_{c,drum} = \frac{\sum_i^n V_i r_i}{\sum_i^n V_i} \tag{A.4}$$

For a given column, the number of possible collapse mechanisms for the static

analysis is equal to its number of drums. This is because during tilting, the top $n = [1, \ldots, N]$ drums could topple to cause structural collapse. The most likely collapse mechanism is therefore identified as the one that is caused by the smallest column tilt angle. To find this mechanism, the collapse angle was found for all N possible collapse mechanisms, and the minimum was chosen.

For each collapse mechanism, the critical column tilt angle, or the collapse angle, is that which causes the center of mass of the set of collapsing drums to lie directly above the tipping point, chosen to be the leftmost point of the base of that set of drums when observing collapse from right to left, or conversely, the rightmost point of the base when observing collapse from left to right. The assembly was then rotated by 1° 360 times to allow for the identification of (1) the most vulnerable collapse direction by searching for the smallest critical column tilt angle and (2) the tilt angle and corresponding peak ground acceleration for the direction of the most likely seismic impulse: northeast to southwest.

A.2.2 Results

The critical tilt angle, θ_c, for each collapse mechanism was identified as the tilt angle that caused the center of mass of the top n drums, where $n = [1, \ldots, N]$, and N is the total number of drums in that column, to lie directly above the tipping point of those drums (Fig. A-2A). As an example, Fig. A-2A shows the determination of the critical tilt angle for the collapse of column 1's top 4 drums from left to right. To find the most likely collapse mechanism for a given column, this analysis was repeated for all N potential collapse mechanisms, and the collapse mechanism with the smallest critical tilt angle was identified.

The locations of the centroids for the sets of the top $[1, 2, \ldots, N]$ drums of each column are shown from top to bottom along each column's axis in Fig. A-3. The plot to the right of each column shows the critical column tilt angle that causes that collapse mechanism. The smallest critical tilt angle, which corresponds with the most likely collapse mechanism, is indicated by dashed red vertical lines. For the orientation of the columns as viewed from northwest (matching the orientation of

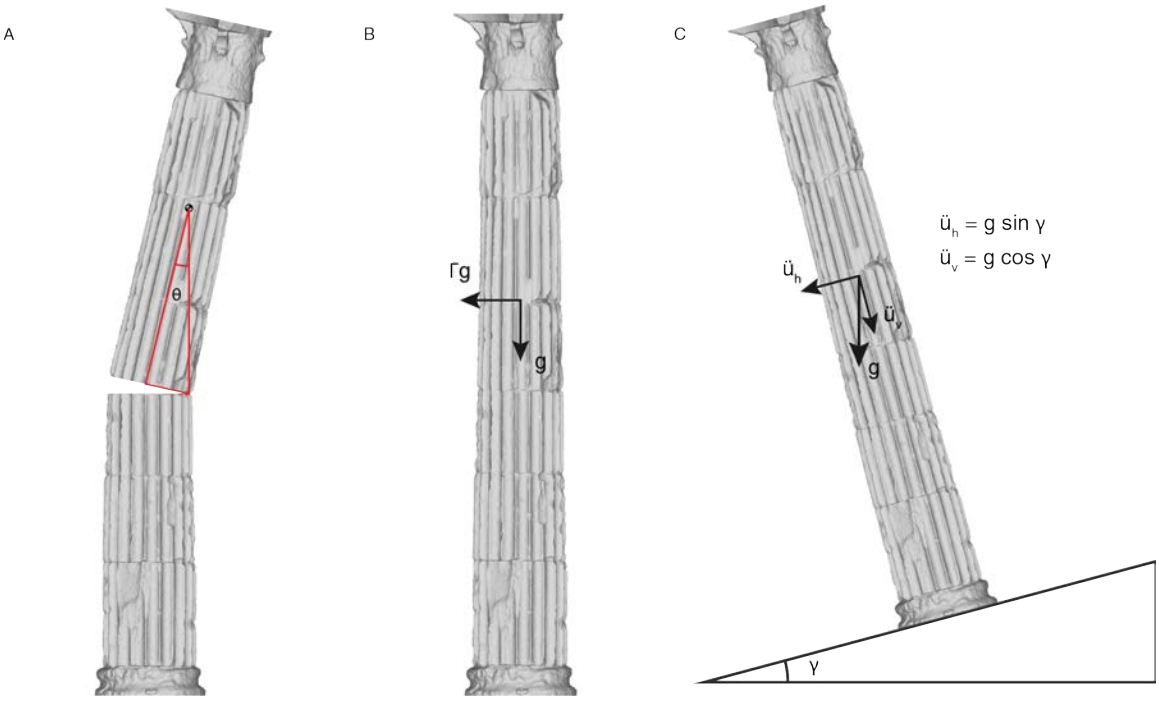

Figure A-2: **Determining the collapse mechanism and the corresponding necessary ground acceleration. A**: The centroid of the top 4 drums determines the tilt angle that causes the top 4 drums to collapse. The set of drums that has the smallest collapse angle is the most likely collapse mechanism. **B**: For the vertically-oriented column, there would be two accelerations: the lateral ground acceleration and the acceleration due to gravity. **C**: For the static tilted column, the local vertical and lateral accelerations are functions of the tilt angle.

the columns in the videos of the scale model experiments), the following critical tilt angles were identified: column 1: 7.19°, column 2: 8.32°, and column 3: 6.83°. For all three columns, their bases remained standing while all their other drums toppled. The models of the columns that are shown in Fig. A-3 are included for illustrating the collapse mechanisms and do not match the view from northwest.

Converting these critical column tilt angles to equivalent lateral accelerations may be understood by comparing the accelerations on the column for the dynamic case (an applied constant lateral acceleration) and for the static case (static tilting), the latter of which is the first order approximation of the former. If a constant lateral acceleration is applied to the upright column, there are two accelerations acting on it: (1) the constant lateral acceleration, Γg, where Γ is an arbitrary constant, which acts perpendicular to the axis of the column, and (2) the acceleration due to gravity, g,

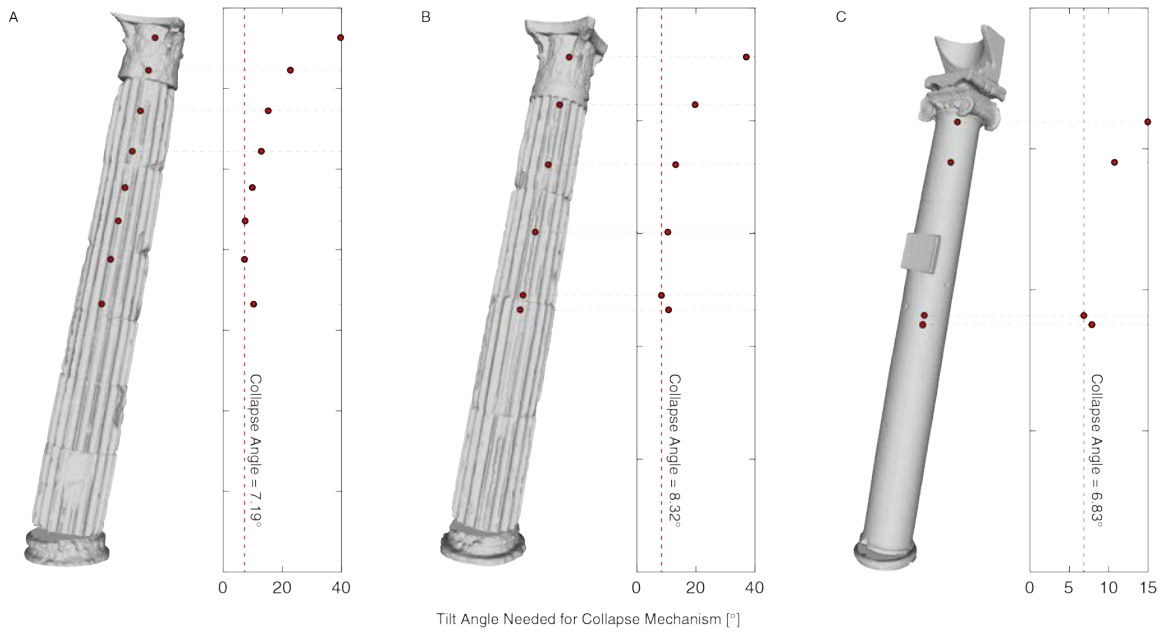

Figure A-3: **Angles for each collapse mechanism for each column.** The columns were rotated such that the front corresponded to the view from the south-east, and each red dot on each column shows the location of the center of mass for each set of the n top drums, where n = [1,..., N], and N = total number of drums. The smallest collapse angle indicates the most likely collapse mechanism, illustrated to the left of each plot. Results are shown for **A**: column 1, **B**: column 2, and **C**: column 3.

which acts parallel to the axis of the column (Fig. A-2B). When the column undergoes static tilting, the only acceleration experienced by the column is the acceleration due to gravity, which acts at an angle (the tilt angle) to the axis of the column (Fig. A-2C). This acceleration due to gravity may be decomposed into two components: a component parallel to the axis of the column, $\ddot{u_v} = g\cos\gamma$, and one perpendicular to it, $\ddot{u_h} = g\sin\gamma$.

Since the static tilting case in Fig. A-2C is a first order approximation of the case in Fig. A-2B, the ratios of the accelerations perpendicular to the axis of the column to the accelerations parallel to the axis of the column are equivalent (Eqn. A.5).

$$\frac{\Gamma g}{g} = \frac{\ddot{u_h}}{\ddot{u_v}} = \frac{g\sin\gamma}{g\cos\gamma} \tag{A.5}$$

It therefore follows that the multiplicative factor for the equivalent lateral acceleration, Γ, is the tangent of the tilt angle that causes collapse (Eqn. A.6).

$$\Gamma = \tan \gamma \tag{A.6}$$

The analysis was repeated for all possible collapse angles from 0-360° with a resolution of 1° starting with the view of the columns from the south (Fig. A-4). This was done to account for the randomness of seismic activity, which could vary in nature, e.g. tectonic earthquakes vs. volcanic earthquakes. The peak ground acceleration associated with an earthquake could also cause collapse in any direction, so this analysis allowed for the identification of the least stable collapse direction as well as the corresponding equivalent lateral acceleration.

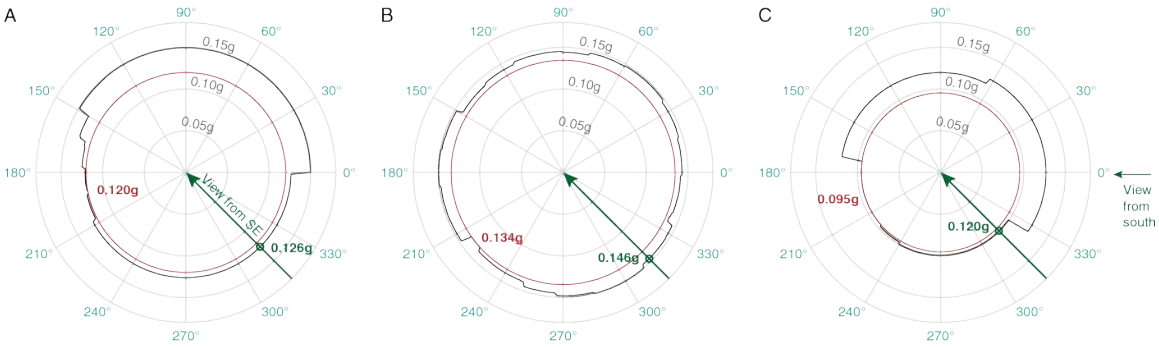

Figure A-4: **Equivalent lateral acceleration for all collapse directions.** The numerical analysis was conducted for all collapse directions from 0-360° with a resolution of 1° for **A**: column 1, **B**: column 2, and **C**: column 3. 0° corresponds to structural collapse from right to left (i.e. from east to west). The red circle corresponds to the minimum collapse angle i.e. lowest equivalent lateral acceleration that would cause structural collapse. The green arrow corresponds to the view from southeast and a collapse from right to left (i.e. from northeast to southwest), which corresponds with the left-to-right collapse of the columns when they are viewed from northwest (also collapse from northeast to southwest) in the scale model collapse videos.

A.3 Corroboration of numerical predictions with scale model experiments

A.3.1 Procedure

Gypsum scale models of the drums of the Corinthian columns, columns 1 and 2, were 3D printed then coated with polyurethane for use in the scale model experiments (Fig. A-5). The polyurethane coating was added to limit damage caused to the drums during collapse experiments and to give the drums coefficients of friction that more closely approximate that of stone. Previous experiments have shown that this process leads to surfaces with coefficients of friction of approximately 0.7 [219], and this value is consistent with the coefficient of friction of stone [227]. The scale models were oriented with the camera facing each column to match the view from the northwest, so that tilting to the right would correspond to tilting in the most probable direction of a seismic impulse, northeast to southwest. Controlling the orientation of the columns in this way also allowed for the direct comparison of the experimental results with the corresponding numerical results. The oriented scale models were placed on a tilt table equipped with a motor which slowly increased the angle of the tilting surface when turned on (Fig. A-5), and slow-motion videos of the collapse were recorded using an iPhone 7 in "Slo-mo" mode. For each experiment, the column was tilted until collapse occurred, then the motor was turned off. Video analysis software (Tracker v5.1) was then used to identify the frame where collapse occurred and measure the corresponding tilt angle that caused collapse. The scale model collapse experiment was conducted three times per column.

A.3.2 Results

The collapse angles measured using video analysis software for each column were converted to equivalent lateral accelerations using Eqn. A.6. The predictions from the numerical analysis and the experimental results from the scale model experiments along with their standard deviations for collapse from northeast to southwest are

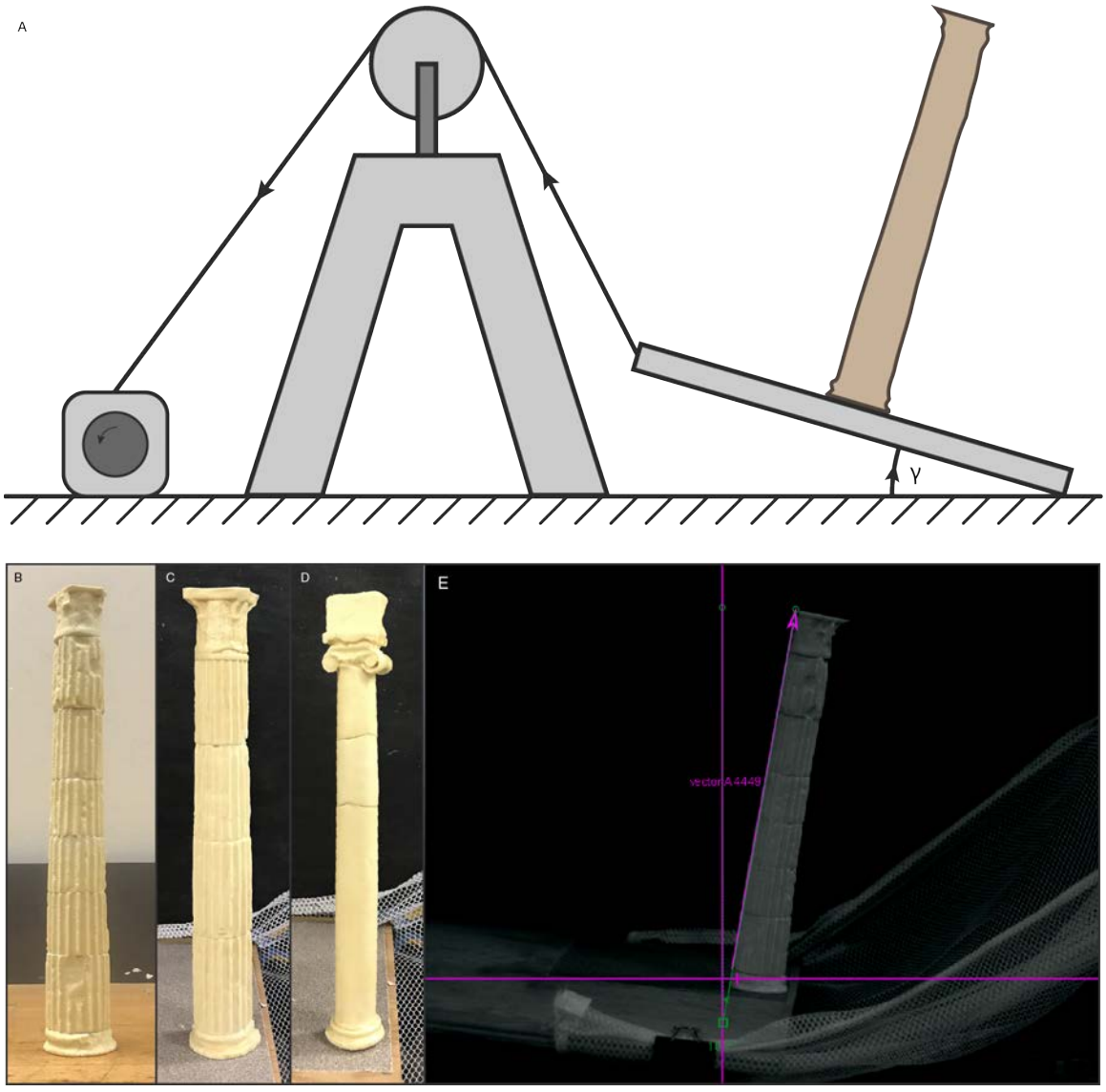

Figure A-5: **Tilting scale model collapse analyses of 3D printed models of columns.** **A**: Tilt table setup showing placement of 3D printed model of column during scale model tests 3D printed models of: **B**: Column 1, **C**: Column 2. **D**: Screenshot of video analysis software used to measure the angle of collapse.

presented in Table A.1 and shown graphically in Fig. A-6E. The average scale model collapse measurements were within 1° of the numerical predictions from the geometric analyses for both columns 1 and 2. The larger disparity was seen in the results for column 2, where the average experimental result was 0.84° lower than the predicted value, which corresponded to a difference in equivalent peak ground acceleration of 0.015 g.

Numerical Predictions		Experimental Results	
Collapse Angle	Equivalent Acceleratiogn	Collapse Angle	Equivalent Acceleration
7.19°	0.126 g	7.80° ± 0.34°	0.137 ± 0.006 g
8.31°	0.146 g	7.47° ± 0.27°	0.131 ± 0.005 g
5.66°	0.099 g	-	-

Table A.1: Average measured collapse angles, numerically predicted collapse angles, and equivalent lateral accelerations for each column.

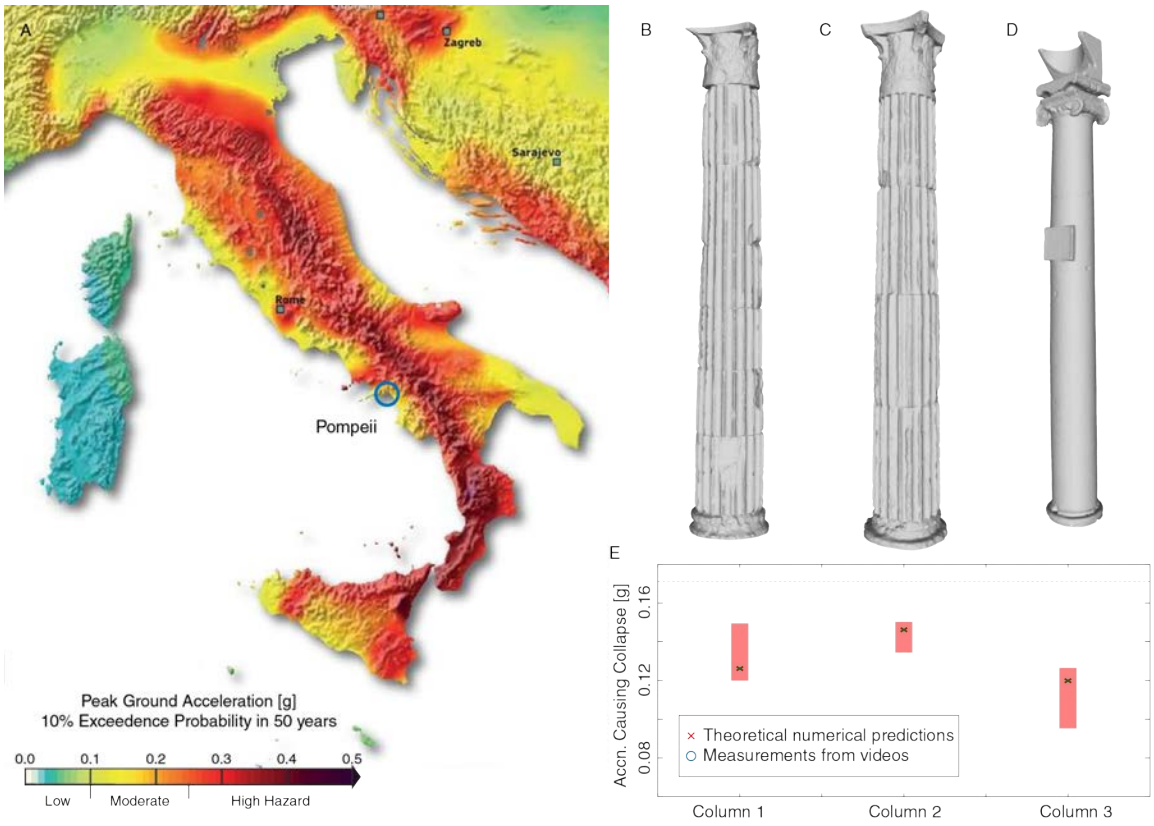

Figure A-6: **Seismic hazard map of Italy and collapse analysis results for columns. A**: Seismic hazard map of Italy, adapted from (Giardini et al., 2013). 3D models of **B**: column 1, **C**: column 2, **D**: column 3. **E**: Plot showing the theoretical and experimental equivalent ground accelerations that lead to the structural collapse of the three columns.

A.4 Material Point Method for exploring failure of elements post-collapse

In order to understand and quantify the consequences of structural collapse on the elements of the columns, the material point method (MPM) was used to simulate

Property	Value
Column Bulk Modulus [GPa]	3.31
Column Shear Modulus [GPa]	2.48
Column Density [kg m^{-3}]	1540
Soil Bulk Modulus [MPa]	58.33
Soil Shear Modulus [MPa]	26.92
Soil Density [kg m^{-3}]	2100
Initial velocity (v_x,v_y) [m s^{-1}]	(14.18, -9.5)

Table A.2: Properties used for MPM simulations.

impact between the capital of column 2 and the ground under a variety of conditions. MPM discretizes a body in a similar manner to other particle-based methods, such as smoothed particle hydrodynamics [228] and the discrete element method [229]. A geometry of interest is divided into small mass elements i.e. material points, which are then assigned state variables, including stress, strain, position, velocity, and mass. The internal stresses that are generated throughout the material are solved for then used to quantify the amount of damage resulting and observe the failure patterns that develop. The MPM results presented in this section were generated by Dr. Samuel Raymond.

For each simulation, the capital drum was initialized with a rotation of 60°, 75°, or 90° about the out-of-the-page direction from its original orientation. The MPM simulation was conducted in two dimensions using the cross section of the capital, which was generated by the MPM simulation engine using the mesh, then discretized into 263,548 material points. Collision of the drum with two kinds of surfaces was modeled: (1) a rigid surface that develops no internal stresses and perfectly reflects all impact energy and (2) a typical soil. The properties used for the drum, rigid surface, and soil-like material are shown in Table A.4. Also included in Table A.4 are initial horizontal (v_x) and vertical (v_y) velocities immediately preceding impact, which were found by integrating approximate equations of motion.

The results of the MPM simulations are shown in Fig. A-7. Collisions with the rigid surface are shown on the left and collisions with the softer, more soil-like material are shown on the right. Each simulation was initialized with a rotation angle of

60°, 75°, or 90° from the vertical. In every case presented in Fig. A-7, the capital undergoes significant damage, expectedly to a lesser extent in the cases of collision with the soil-like material, which is able to dissipate some of the energy from the collision. In each case, parts of the capital become separated from its main body, and in the rigid-surface collisions, the fracture patterns extend throughout the entire cross-section. For collision angles of less than 90°, the flared region at the base of the capital approaches the collision surface first, and as a result, more extensive damage is sustained there in these cases, and for collisions at 90°, the damage is more uniformly distributed along the axis of the capital.

A.5 Comparison of estimates for critical peak ground accelerations with seismic hazard maps

The structures in Pompeii are unique in that for much of their history, they were protected from moisture, environmental changes, and structural collapse by the layers of tephra that were deposited onto the city during the eruption of Mount Vesuvius in 79 CE. Thus, the structures in Pompeii are of very few from the ancient world that have been so well-preserved for such a long time, and as such, hold tremendous historical and cultural value. The three freestanding columns of interest from the Tempio di Apollo, which dates back to the 8th or 7th century BCE, are over 2000 years old and are of immense cultural value.

MPM simulations of collisions between the capital of column 2 and both a rigid surface and a softer, soil-like material represent the extreme cases of what could result from the drums hitting the ground, and all of the presented simulation results indicate that the drums would sustain catastrophic and irreversible damage in the event of structural collapse. The extent to which each of the columns is at risk of structural collapse was studied by estimating the peak ground acceleration that would lead to each column's collapse. This was conducted using numerical geometric analysis and tilt experiments, which approximate lateral acceleration to first order.

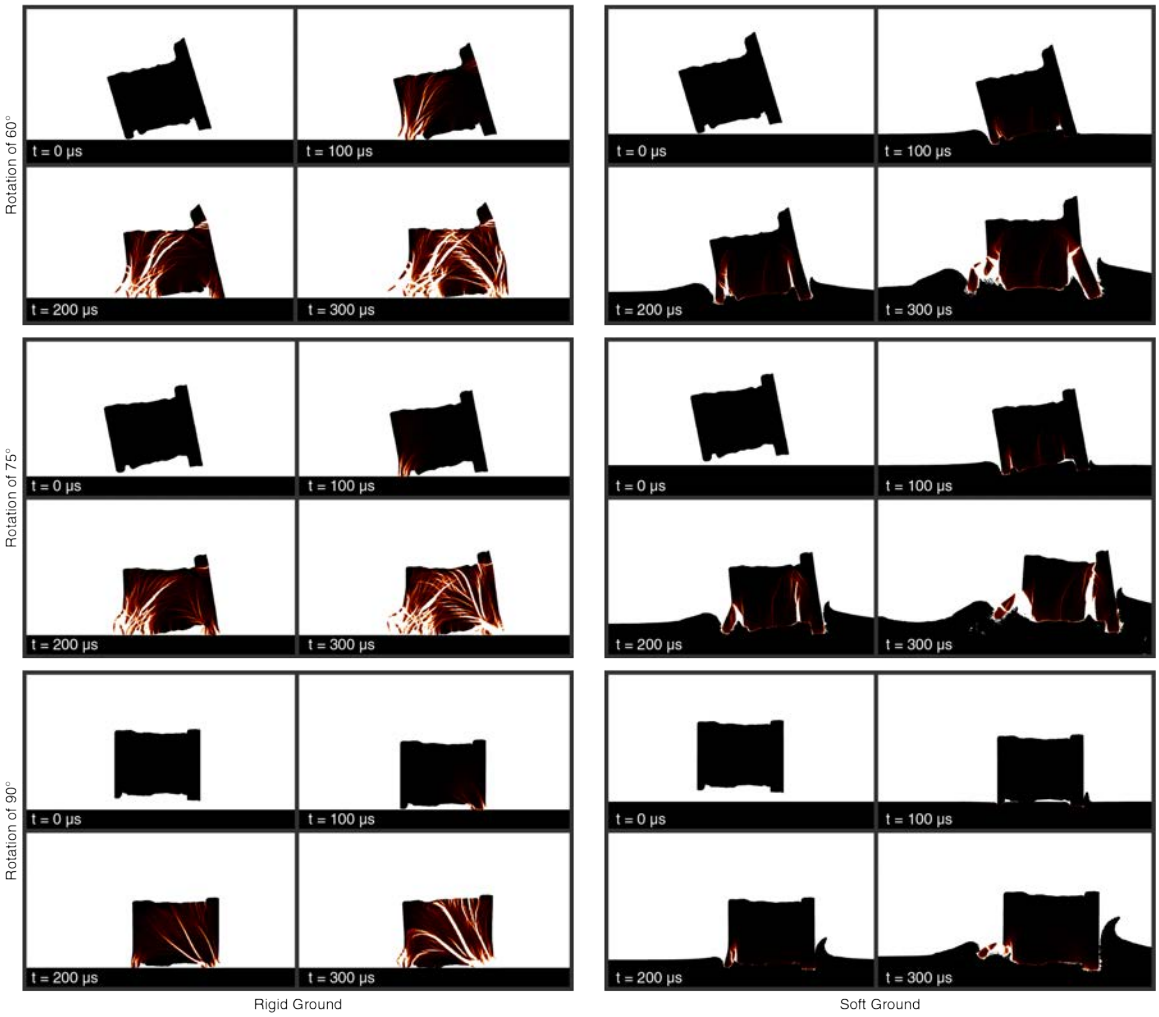

Figure A-7: **Fracture analysis of 2D cross-sections of the capital of column 2.** Each 4-part box shows the state of the capital at 0 µs, 100 µs, 200 µs, and 300 µs into the simulation. Left set of results: states of capital during collision with rigid ground. Right set of results: states of capital during collision with soft, soil-like ground. The collision was simulated using three initial angles: 60°, 75°, and 90° from the vertical. The color relates to the amount of damage sustained from black, indicating zero damage, to yellow, indicating maximum damage.

The tilt angles that led to structural instability were found numerically by analyzing the 3D models of each structure (Fig. A-2), and these numerical predictions were corroborated using scale model collapse experiments for two of the three columns, which were 3D printed in gypsum and coated with polyurethane. There was a small disparity of less than 1° between the numerical predictions and the scale model measurements, which could be a result of a number of experimental factors. In preparing

the drums for 3D printing, the meshes were refined by 1.4% to avoid printing excessive amounts of detail, and after printing the drums were sanded to remove artifacts from printing, and the drums were coated with a protective layer of polyurethane. All of these steps were necessary but would also slightly alter the geometries of the drums.

Another potential reason for this difference could be a result of human error in orienting the columns to match the view from northwest before conducting the experimental collapse analyses. To address this source of error, the drums were marked in an effort to ensure the repeatability of the experiments, and three videos were collected for the collapse of each column, the results of which were averaged. However, even with the measures taken, the orientations in the videos could have still differed slightly from the true desired orientations, which were much more easily matched in the numerical geometric analyses.

Regardless, the results obtained from the scale model experiments were very similar to the numerical analysis predictions, and as such did corroborate those estimates. The larger discrepancy (seen in the results for column 2) show an underestimation of only 0.015 g.

The risk of the columns collapsing in a seismic event was then evaluated with the use of a seismic hazard map. Seismic hazard maps are used for visualizing the likelihood of various peak ground accelerations throughout a given geographical area. A seismic hazard map of Italy, extracted from the seismic map of the Euro-Mediterranean region that was produced by the Seismic Hazard Harmonization in Europe multidisciplinary collaborative project in 2013, with the position of Pompeii indicated by a blue circle, is shown in Fig. A-6A [230]. In this seismic hazard map, color is used to indicate the peak ground acceleration (PGA) that will be reached or exceeded with a probability of 10% over the course of the next 50 years, as indicated by the color scale at the bottom of Fig. A-6A [230].

The scale model experimental results and the geometric analysis results are presented graphically in Fig. A-6E below the three-dimensional models of the three columns of interest (Fig. A-6B, Fig. A-6C, and Fig. A-6D). The numerical predictions for the critical lateral accelerations for each of the three columns are indicated

by red crosses, and the corresponding scale model experimental results for columns 1 and 2 indicated by blue circles with error bars showing the standard deviations (Fig. A-6E). The partially transparent red rectangles indicate the range of possible collapse angles for each column, which were obtained by repeating the numerical geometric analysis at every orientation by rotating each column from 0°-360° at a resolution of 1°. The lower bound of the ranges indicated by these red rectangles correspond to the minimum collapse angles (which correspond to the least stable collapse directions), which are indicated by the red inner circles in Fig. A-4.

The horizontal green dashed line in Fig. A-6E corresponds to the PGA with a 10% exceedance probability in 50 years for Pompeii, extracted from the seismic hazard map using the color bar in Fig. A-6A, which was found to be approximately 0.17g. This value exceeds both the numerical and experimental predictions for the critical peak ground accelerations for each column presented in this work. This suggests that should they be left without intervention, all three of these columns could collapse in the next 50 years, since each column's critical peak ground acceleration would be exceeded with at least a 10% probability in that time period. In this event, the drums (particularly the capitals, which would fall the farthest) would be expected to undergo irreversible damage based on the MPM simulation results.

However, it must be noted that the presented analysis for the estimation of the critical peak ground accelerations required to cause structural collapse is only reliable to first order. In reality, in the event of significant seismic activity, the columns would become part of a complex dynamic situation, that could arise from plate movements or the movement of magma beneath the surface of the earth. The accelerations could vary in time, and the lateral accelerations on the columns could be a superposition of accelerations from a number of directions. Therefore, it is difficult to say definitively whether the columns will or will not collapse in the next 50 years based on the presented analysis.

The presented analysis is better suited as a tool for the prioritization of structural interventions. Many sites already implement interventions to protect freestanding multi-drum columns in the event of seismic activity, but where there is a large number

of these columns, for example in the case of Pompeii, deciding which columns should be protected most urgently may pose a challenge for the site. The tools presented in this work would be helpful in quickly identifying which columns have the lowest critical collapse angles (for any collapse direction) and are therefore at the greatest risk of collapse.

Although the specific geometric analysis used in this work would not necessarily work for all geometries of masonry structures, the procedure for conducting scale model collapse analyses could be applied to any particular type of masonry structure of known geometry to evaluate its risk of collapse in the event of seismic activity, aid in the design of support structures, and prioritize structures for structural interventions.

A.6 Conclusions: The critical need for knowing the true mechanical properties of historic building materials

In this work, a case study on the structural stability of three freestanding, multi-drum columns from the Tempio di Apollo in Pompeii was presented. Numerical geometric analyses were performed to assess the stability of the columns via the determination of the critical column tilt angle and therefore the critical peak ground acceleration of each column from all directions. These results were then corroborated using scale model experiments conducted for two of the three columns in the direction of the most likely seismic impulse: northeast to southwest. MPM simulations were then used to demonstrate the irreversible damage that would be sustained by the drums in the event of structural collapse, which could occur in the future since the earthquake peak ground acceleration that has a 10% probability of being exceeded in the next 50 years in Pompeii is greater than the critical peak ground accelerations found for all three columns studied.

Appendix B

K-means clustering of kidney stone SEM-EDS data

In Chapter 4, it was demonstrated that unsupervised learning techniques, such as fuzzy c-means clustering and k-means clustering, can be applied to N-dimensional quantitative SEM-EDS data to determine the spatial distribution of chemically distinct phases. Using this approach, it was possible to maps the phases present in ancient Roman mortar, and in the study of the remnant lime clasts in ancient Roman concrete, it was possible to distinguish the higher-Ca remnant lime clast cores from their lower-Ca perimeters and observe the recrystallized C-A-S-H like phase that extended from the clasts into the binding matrix.

This section shows the results of applying the presented clustering and model selection procedure to another composite material of unknown composition: human kidney stones. The phase maps are then compared with the average chemical compositions of the stones, obtained using clinical infrared spectroscopy.

B.1 Clinical infrared spectroscopy data

Prior to being embedded in epoxy, sectioned, and polished for imaging, the average chemical compositions of the following three kidney stones were measured using infrared spectroscopy (IR), the results of which are presented in Table B.1.

Sample	COM	COD	HA	CA	UA	PTN	Clustering Elements
B04	85	10	3	-	-	2	Ca, Cl, Mg, P, S
B12	55	30	10	3	-	2	Ca, Cl, F, P
B13	27	-	-	-	70	3	Ca, Cl, Si, S

Table B.1: Average chemical compositions of three kidney stones as obtained using IR spectroscopy. COM: calcium oxalate monohydrate, COD: calcium oxalate dihydrate, HA: hydroxyapatite, CA: carbonate apatite, UA: uric acid, PTN: proteins.

B.2 K-means clustering of SEM-EDS data

In clustering the quantitative SEM-EDS data for each of these kidney stones, carbon and oxygen were first omitted, and the remaining elemental data were clustered with respect to the other quantifiable elements. The source of the chlorine present in each of the datasets is likely the epoxy in which they were embedded. The remaining elements that were used for k-means clustering are presented in the final column of Table B.1. The BS-SEM images of each of the kidney stones and the phase maps obtained by clustering the quantitative SEM-EDS data are presented in Fig. B-1.

Sample B04 (Fig. B-1A) is primarily composed of calcium oxalate monohydrate [COM: $C_2H_2CaO_5$] and calcium oxalate dihydrate [COD: $C_2H_4CaO_6$], which are difficult to distinguish using this technique, since the only element present in these two phases that may be reliably quantified using SEM-EDS is calcium. The difficulty in distinguishing COM and COD using this technique is once again seen in the phase map of sample B12 in Fig. B-1E. However, the IR data indicated that this stone contains 10% hydroxyapatite [HA: $Ca_5(PO_4)_3(OH)$], and this is shown in the phase map as the red phase at the core of the stone. Sample B12 also contains 3% carbonate apatite [CA: apatite (containing calcium and phosphorous) doped with carbonate], but the clustering procedure did not isolate that phase. This could be due to the mixing of CA with other phases within pixels, which is possible due to the low CA content and the large field of view (and therefore pixel size) of the image, or due to it being difficult to distinguish from HA.

Sample B13 is a kidney stone that is comprised of 70% uric acid [UA: $C_5H_4N_4O_3$] and 27% COM. Given the distribution of the phases identified in Fig. B-1F, it may

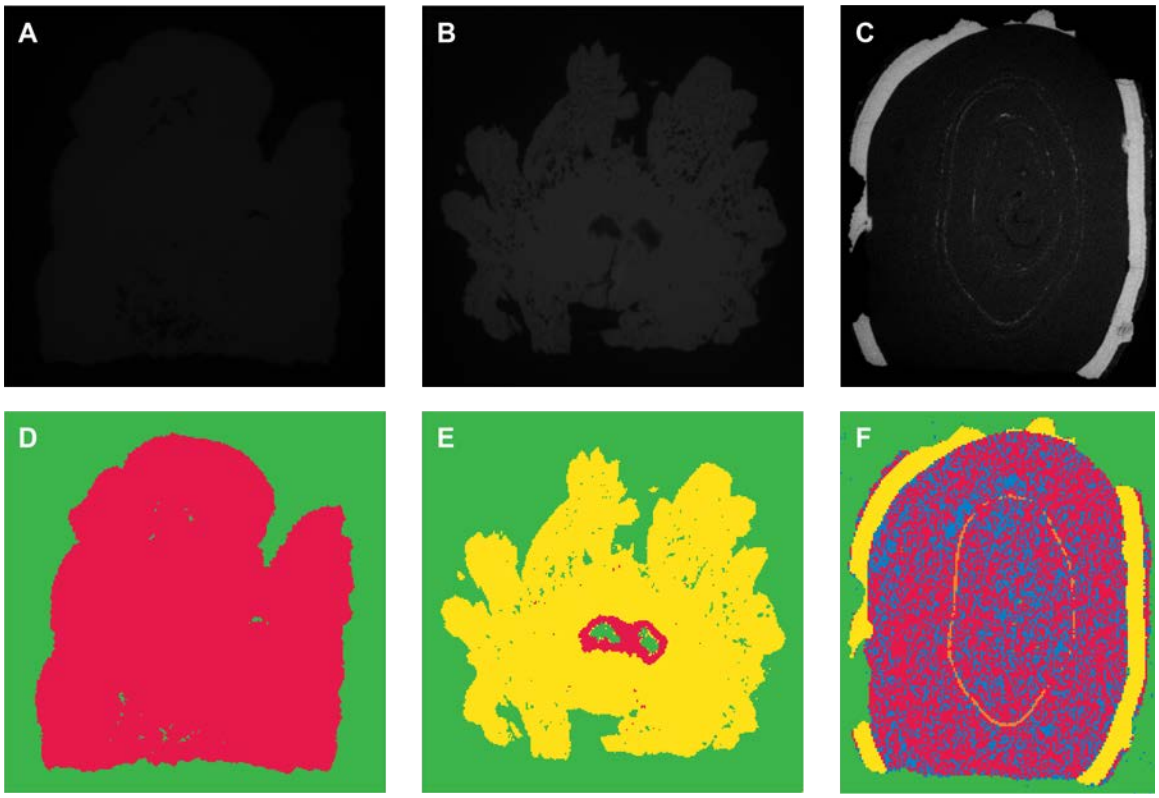

Figure B-1: **Phase maps of kidney stones as obtained through k-means clustering of quantitative SEM-EDS elemental data. A**: Sample B04. **B**: Sample B09. **C**: Sample B12. **D**: Sample B13.

be deduced that the red and blue phases are associated with UA and the yellow phase along the perimeter is associated with COM. This is further supported by the increased brightness of the pixels associated with the perimeter phase in the BS-SEM image, which is caused by COM (which contains calcium) having heavier elements than UA. The orange phase that is seen as a ring in the UA matrix is associated with increased amounts of sulfur, which could be due to changes in the diet or medication of the patient during the growth of the kidney stones. The separation of the UA phase into two phases could be a result of differences in porosity throughout the kidney stone, which would result in chlorine from the epoxy being included in varying amounts throughout the cross-section of the kidney stone.

Bibliography

[1] Y. Yadin, *The Temple Scroll: The Hidden Law of the Dead Sea Sect*. Random House Incorporated, 1985.

[2] "Digital Dead Sea Scrolls at the Israel Museum, Jerusalem - The Temple Scroll." http://dss.collections.imj.org.il/temple. Accessed: 2019-01-17.

[3] T. Martins and H. Varum, "Adobe's mechanical characterization in ancient constructions: the case of Aveiro's region," in *Materials science forum*, vol. 514, pp. 1571–1575, Trans Tech Publications Ltd, 2006.

[4] F. Fernandes and P. B. Lourenço, "Evaluation of the compressive strength of ancient clay bricks using microdrilling," *Journal of Materials in Civil Engineering*, vol. 19, pp. 791–800, Sept. 2007.

[5] J. Vorel, V. Šmilauer, and Z. Bittnar, "Multiscale simulations of concrete mechanical tests," *Journal of Computational and Applied Mathematics*, vol. 236, no. 18, pp. 4882–4892, 2012.

[6] J. Rosell, R. Blasco, G. Campeny Vall-llosera, J. C. Díez Fernández-Lomana, R. Alonso Alcalde, L. Menéndez Granda, J. L. Arsuaga, J. M. Bermúdez de Castro, and E. Carbonell, "Bone as a technological raw material at the Gran Dolina site (Sierra de Atapuerca, Burgos, Spain)," *Journal of Human Evolution*, vol. 61, no. 1, pp. 125–131, 2011.

[7] A. Masic, M. R. Chierotti, R. Gobetto, G. Martra, I. Rabin, and S. Coluccia, "Solid-state and unilateral NMR study of deterioration of a Dead Sea Scroll fragment," *Analytical and Bioanalytical Chemistry*, vol. 402, no. 4, pp. 1551–1557, 2012.

[8] I. Mantouvalou, T. Wolff, O. Hahn, I. Rabin, L. Lühl, M. Pagels, W. Malzer, and B. Kanngiesser, "3D Micro-XRF for Cultural Heritage Objects: New Analysis Strategies for the Investigation of the Dead Sea Scrolls," *Analytical Chemistry*, vol. 83, pp. 6308–6315, 2011.

[9] M. Jackson, D. Deocampo, F. Marra, and B. Scheetz, "Mid-Pleistocene pozzolanic volcanic ash in ancient Roman concretes," *Geoarchaeology: An International Journal*, vol. 25, pp. 36–74, Jan. 2010. Publisher: Wiley Online Library.

[10] M. V. Pollio and M. H. Morgan, *Vitruvius: the ten books on architecture*. Cambridge: Harvard University Press, 1914.

[11] S. D. Palkovic, D. B. Brommer, K. Kupwade-Patil, A. Masic, M. J. Buehler, and O. Büyüköztürk, "Roadmap across the mesoscale for durable and sustainable cement paste - A bioinspired approach," *Construction and Building Materials*, vol. 115, pp. 13–31, 2016. Publisher: Elsevier.

[12] M. D. Jackson, G. Vola, D. Všianskỳ, J. P. Oleson, B. E. Scheetz, C. Brandon, and R. L. Hohlfelder, "Cement microstructures and durability in ancient roman seawater concretes," in *Historic Mortars*, pp. 49–76, Springer, 2012.

[13] M. D. Jackson, E. N. Landis, P. F. Brune, M. Vitti, H. Chen, Q. Li, M. Kunz, H.-R. Wenk, P. J. M. Monteiro, and A. R. Ingraffea, "Mechanical resilience and cementitious processes in Imperial Roman architectural mortar," *Proceedings of the National Academy of Sciences of the United States of America*, vol. 111, pp. 18484–18489, Dec. 2014. Publisher: National Academy of Sciences.

[14] L. C. Lancaster, *Concrete vaulted construction in Imperial Rome: innovations in context*. New York: Cambridge University Press, 1 ed., 2005.

[15] G. P. Secundus and H. Rackham, *Pliny: Natural History: in Ten Volumes*. Harvard University Press, 1942.

[16] A. Samuelli Ferretti, "Proposte per lo studio teorico-sperimentale della statica dei monumenti in opus caementicium," *Materiali e strutture: problemi di conservazione*, vol. 7, no. 2-3, pp. 63–84, 1997.

[17] M. Boyle, D. A. Crocker, J. R. Prestera, S. G. Barton, L. W. Bell, G. R. U. Berg, J. E. Cook, R. Cook, W. J. Costa, K. W. Day, S. H. Lee, G. R. Mass, J. S. Pierce, H. C. Robinson, D. Crocker, J. Scherocman, M. Taylor, S. J. Virgalitte, J. W. Weber, and D. J. White, "Standard Practice for Selecting Proportions for Structural Lightweight Concrete (ACI 211.2-98)," tech. rep., 2004.

[18] M. Stefanidou and I. Papayianni, "The role of aggregates on the structure and properties of lime mortars," *Cement and Concrete Composites*, vol. 27, no. 9-10, pp. 914–919, 2005. ISBN: 0958-9465.

[19] H. F. W. Taylor, *Cement chemistry*. London: T. Telford, 2nd ed ed., 1997.

[20] D. Miriello, D. Barca, A. Bloise, A. Ciarallo, G. M. Crisci, T. De Rose, C. Gattuso, F. Gazineo, and M. F. L. Russa, "Characterisation of archaeological mortars from Pompeii (Campania, Italy) and identification of construction phases by compositional data analysis," *Journal of Archaeological Science*, vol. 37, no. 9, pp. 2207–2223, 2010.

[21] E. S. Hodgkinson and C. R. Hughes, "The mineralogy and geochemistry of cement/rock reactions: high-resolution studies of experimental and analogue

materials," *Geological Society, London, Special Publications*, vol. 157, no. 1, pp. 195–211, 1999. ISBN: 1862390401.

[22] M. D. Jackson, S. R. Mulcahy, H. Chen, Y. Li, Q. Li, P. Cappelletti, and H.-R. Wenk, "Phillipsite and Al-tobermorite mineral cements produced through low-temperature water-rock reactions in Roman marine concrete," *American Mineralogist*, vol. 102, pp. 1435–1450, 2017.

[23] "The Cement Sustainability Initiative: 10 Years of Progress - Moving on to the Next Decade," tech. rep., World Business Council For Sustainable Development, 2012.

[24] W. Kurdowski, *Cement and concrete chemistry*. Kraków, Poland: Springer Science & Business, 2014.

[25] P. F. Brune, A. R. Ingraffea, M. D. Jackson, and R. Perucchio, "The fracture toughness of an Imperial Roman mortar," *Engineering Fracture Mechanics*, vol. 102, pp. 65–76, 2013. Publisher: Elsevier.

[26] J. Higl, M. Köhler, and M. Lindén, "Confocal Raman microscopy as a non-destructive tool to study microstructure of hydrating cementitious materials," *Cement and Concrete Research*, vol. 88, pp. 136–143, 2016.

[27] G. Renaudin, J. Russias, F. Leroux, C. Cau-dit Coumes, and F. Frizon, "Structural characterization of C-S-H and C-A-S-H samples—Part II: Local environment investigated by spectroscopic analyses," *Journal of Solid State Chemistry*, vol. 182, pp. 3320–3329, Dec. 2009.

[28] J. Ibáñez, L. Artús, R. Cuscó, Á. López, E. Menéndez, and M. C. Andrade, "Hydration and carbonation of monoclinic C_2S and C_3S studied by Raman spectroscopy," *Journal of Raman Spectroscopy: An International Journal for Original Work in all Aspects of Raman Spectroscopy, Including Higher Order Processes, and also Brillouin and Rayleigh Scattering*, vol. 38, no. 1, pp. 61–67, 2007.

[29] K. Kupwade-Patil, A. F. Al-Aibani, M. F. Abdulsalam, C. Mao, A. Bumajdad, S. D. Palkovic, and O. Büyüköztürk, "Microstructure of cement paste with natural pozzolanic volcanic ash and Portland cement at different stages of curing," *Construction and Building Materials*, vol. 113, pp. 423–441, 2016. Publisher: Elsevier.

[30] J. E. Rossen and K. L. Scrivener, "Optimization of SEM-EDS to determine the C-A-S-H composition in matured cement paste samples," *Materials Characterization*, vol. 123, pp. 294–306, 2017. Publisher: Elsevier.

[31] R. J. Myers, S. A. Bernal, and J. L. Provis, "Phase diagrams for alkali-activated slag binders," *Cement and Concrete Research*, vol. 95, pp. 30–38, 2017. Publisher: Elsevier.

[32] P. T. Durdziński, C. F. Dunant, M. Ben Haha, and K. L. Scrivener, "A new quantification method based on SEM-EDS to assess flyash composition and study the reaction of its individual components in hydrating cement paste," *Cement and Concrete Research*, vol. 73, pp. 111–122, 2015.

[33] V. Kocaba, E. Gallucci, and K. L. Scrivener, "Methods for determination of degree of reaction of slag in blended cement pastes," *Cement and Concrete Research*, vol. 42, pp. 511–525, Mar. 2012.

[34] S.-i. Igarashi, M. Kawamura, and A. Watanabe, "Analysis of cement pastes and mortars by a combination of backscatter-based SEM image analysis and calculations based on the Powers model," *Cement and Concrete Composites*, vol. 26, no. 8, pp. 977–985, 2004. ISBN: 0958-9465.

[35] F. Massazza and M. Pezzuoli, "Some teachings of a Roman concrete," in *Mortars, cements and grouts used in the conservation of historic buildings. Symposium, Rome, 3-6 Nov. 1981*, (Rome), pp. 219–245, ICCROM, 1982.

[36] M. Jackson, P. Ciancio Rossetto, C. Kosso, M. Buonfiglio, and F. Marra, "Building materials of the theatre of Marcellus, Rome," *Archaeometry*, vol. 53, no. 4, pp. 728–742, 2011.

[37] M. D. Jackson, J. M. Logan, B. E. Scheetz, D. M. Deocampo, C. G. Cawood, F. Marra, M. Vitti, and L. Ungaro, "Assessment of material characteristics of ancient concretes, Grande Aula, Markets of Trajan, Rome," *Journal of Archaeological Science*, vol. 36, no. 11, pp. 2481–2492, 2009. Publisher: Elsevier ISBN: 0305-4403.

[38] S. Amini, A. Masic, L. Bertinetti, J. S. Teguh, J. S. Herrin, X. Zhu, H. Su, and A. Miserez, "Textured fluorapatite bonded to calcium sulphate strengthen stomatopod raptorial appendages," *Nature Communications*, vol. 5, p. 3187, 2014. Publisher: Nature Publishing Group ISBN: 2041-1723.

[39] J. V. D. Gucht, "A Physical Model of Nacre," *Composites Science and Technology*, vol. 36, no. 3, pp. 255–266, 1989.

[40] A. Masic and J. C. Weaver, "Large area sub-micron chemical imaging of magnesium in sea urchin teeth," *Journal of Structural Biology*, vol. 189, no. 3, pp. 269–275, 2015.

[41] P. Corke, *Robotics, Vision and Control: Fundamental Algorithms In MATLAB*. Springer-Verlag Berlin Heidelberg, 2011. Publication Title: Springer Tracts in Advanced Robotics.

[42] K. L. Scrivener, R. Snellings, and B. Lothenbach, *A practical guide to microstructural analysis of cementitious materials*. Crc Press, 2016.

[43] "The Concrete Portal: Mineral Admixtures." http://www.theconcreteportal.com/admix_min.html. Accessed: 2017-06-21.

[44] K. T. Butler, D. W. Davies, H. Cartwright, O. Isayev, and A. Walsh, "Machine learning for molecular and materials science," *Nature*, vol. 559, pp. 547–555, July 2018.

[45] D. H. de Boer and G. Crosby, "Evaluating the potential of SEM/EDS analysis for fingerprinting suspended sediment derived from two contrasting topsoils," *Catena*, vol. 24, no. 4, pp. 243–258, 1995.

[46] S. Pinet, B. Lartiges, J.-M. Martinez, and S. Ouillon, "A SEM-based method to determine the mineralogical composition and the particle size distribution of suspended sediment," *International Journal of Sediment Research*, vol. 34, pp. 85–94, Apr. 2019.

[47] K. Slezakova, J. Pires, F. Martins, M. Pereira, and M. Alvim-Ferraz, "Identification of tobacco smoke components in indoor breathable particles by SEM–EDS," *Atmospheric Environment*, vol. 45, pp. 863–872, Feb. 2011.

[48] A. Genga, F. Baglivi, M. Siciliano, T. Siciliano, M. Tepore, G. Micocci, C. Tortorella, and D. Aiello, "SEM-EDS investigation on PM10 data collected in Central Italy: Principal Component Analysis and Hierarchical Cluster Analysis," *Chemistry Central Journal*, vol. 6, p. S3, Dec. 2012.

[49] K. Slezakova, J. C. M. Pires, M. C. Pereira, F. G. Martins, and M. C. Alvim-Ferraz, "Influence of traffic emissions on the composition of atmospheric particles of different sizes–Part 2: SEM–EDS characterization," *Journal of Atmospheric Chemistry*, vol. 60, pp. 221–236, July 2008.

[50] J. Einsle, B. Martineau, I. Buisman, Z. Vukmanovic, D. Johnstone, A. Eggeman, P. A. Midgley, and R. J. Harrison, "All mixed up: Using machine learning to address heterogeneity in (natural) materials," *Microscopy and Microanalysis*, vol. 24, no. S1, pp. 562–563, 2018.

[51] C. L. Stork and M. R. Keenan, "Advantages of clustering in the phase classification of hyperspectral materials images," *Microscopy and Microanalysis*, vol. 16, pp. 810–820, 2010.

[52] C. L. Stork, "An extremely fast and efficient hierarchical clustering algorithm applicable to hyperspectral microscopy and microanalysis images," *Microscopy and Microanalysis*, vol. 16, no. S2, pp. 268–269, 2010.

[53] S. Vogt, J. Maser, and C. Jacobsen, "Data analysis for X-ray fluorescence imaging," *Journal de Physique IV (Proceedings)*, vol. 104, pp. 617–622, Mar. 2003.

[54] B. Vekemans, B. Vekemans, K. Janssens, L. Vincze, A. Aerts, F. Adams, and J. Hertogen, "Automated segmentation of µ-XRF image sets," *X-ray Spectrometry*, vol. 26, no. January, pp. 333 – 346, 1997.

[55] B. Vekemans, L. Vincze, F. E. Brenker, and F. Adams, "Processing of three-dimensional microscopic X-ray fluorescence data," *Journal of Analytical Atomic Spectrometry*, vol. 19, no. 10, pp. 1302–1308, 2004. ISBN: 0267-9477.

[56] Y. Tarabalka, M. Fauvel, J. Chanussot, and J. A. Benediktsson, "SVM-and MRF-based method for accurate classification of hyperspectral images," *IEEE Geoscience and Remote Sensing Letters*, vol. 7, no. 4, pp. 736–740, 2010.

[57] H. S. Djayaprabha, T.-P. Chang, and J.-Y. Shih, "Comparison study of dynamic elastic moduli of cement mortar and no-cement slag based cementitious mortar activated with calcined dolomite with impulse excitation technique," in *MATEC Web of Conferences*, vol. 186, p. 02004, EDP Sciences, 2018.

[58] T. Sugiyama, M. Promentilla, T. Hitomi, and N. Takeda, "Application of synchrotron microtomography for pore structure characterization of deteriorated cementitious materials due to leaching," *Cement and Concrete Research*, vol. 40, no. 8, pp. 1265–1270, 2010.

[59] S. Diamond and E. Landis, "Microstructural features of a mortar as seen by computed microtomography," *Materials and Structures*, vol. 40, no. 9, pp. 989–993, 2007.

[60] M. A. B. Promentilla, T. Sugiyama, T. Hitomi, and N. Takeda, "Characterizing the 3D pore structure of hardened cement paste with synchrotron microtomography," *Journal of Advanced Concrete Technology*, vol. 6, no. 2, pp. 273–286, 2008.

[61] J. Elsen, "Microscopy of historic mortars—a review," *Cement and Concrete Research*, vol. 36, no. 8, pp. 1416–1424, 2006. ISBN: 0008-8846.

[62] S. Bruni, F. Cariati, P. Fermo, P. Cairati, G. Alessandrini, and L. Toniolo, "White lumps in fifth-to seventeenth-century ad mortars from northern Italy," *Archaeometry*, vol. 39, no. 1, pp. 1–7, 1997.

[63] M. D. Jackson, G. Vola, E. Gotti, and B. Zanga, "Sea-water concretes and their material characteristics," in *Building for eternity: the history and technology of Roman concrete engineering in the sea* (J. P. Oleson, ed.), pp. 141–188, Havertown, PA: Oxbow Books, 2014.

[64] J. P. Oleson, L. Bottalico, C. Brandon, R. Cucitore, E. Gotti, and R. L. Hohlfelder, "Reproducing a roman maritime structure with vitruvian pozzolanic concrete," *Journal of Roman Archaeology*, vol. 19, no. 1, pp. 29–52, 2006.

[65] M. D. Jackson, J. Moon, E. Gotti, R. Taylor, S. R. Chae, M. Kunz, A. H. Emwas, C. Meral, P. Guttmann, P. Levitz, H. R. Wenk, and P. J. M. Monteiro, "Material and elastic properties of Al-tobermorite in ancient roman seawater concrete," *Journal of the American Ceramic Society*, vol. 96, no. 8, pp. 2598–2606, 2013. ISBN: 0002-7820.

[66] M. D. Jackson and G. Vola, "Appendix 4: Compositional analyses of concretes drilled from harbour structures by ROMACONS," in *Building for eternity: the history and technology of Roman concrete engineering in the sea* (J. P. Oleson, ed.), pp. 285–306, Havertown, PA: Oxbow Books, 2014.

[67] J. M. Maragh, J. C. Weaver, and A. Masic, "Large-scale micron-order 3D surface correlative chemical imaging of ancient roman concrete," *PLOS One*, vol. 14, no. 2, p. e0210710, 2019.

[68] R. Schuetz, J. M. Maragh, J. C. Weaver, I. Rabin, and A. Masic, "The Temple Scroll: Reconstructing an ancient manufacturing practice," *Science Advances*, vol. 5, p. eaaw7494, Sept. 2019.

[69] L. Bertrand, C. Gervais, A. Masic, and L. Robbiola, "Paleo-inspired Systems: Durability, Sustainability, and Remarkable Properties," *Angewandte Chemie International Edition*, vol. 57, pp. 7288–7295, June 2018.

[70] Z. de Groot, "Die Herstellung von Goldschlägerhaut, transparentem und gespaltenem Pergament," in *Pergament - Geschichte, Struktur, Restaurierung und Herstellung heute* (P. Rück, ed.), Sigmaringen: Jan Thorbecke Verlag, 1992.

[71] R. Reed and J. B. Poole, "A study of some Dead Sea Scroll and leather fragments from Cave 4 at Qumran Part I: Physical examination," *Proceedings of the Leeds Philosophical and Literary Society, Scientific section*, vol. 9, no. 1, pp. 1–13, 1962.

[72] A. Wallert, "Tannins on the parchment of the Dead Sea scrolls," in *ICOM committee for conservation, 11th triennial meeting in Edinburgh, Scotland, 1-6 September 1996: Preprints*, pp. 560–564, 1996.

[73] "Inden witten Hasewint." http://indenwittenhasewint.blogspot.com/2012/12/1-making-of-parchment.html. Accessed: 2019-01-18.

[74] R. Reed, *Ancient skins, parchments and leathers*. New York: Seminar Press, 1972.

[75] Y. Yadin, "Tefillin (Phylacteries) from Qumran," *Eretz-Israel*, vol. 9, pp. 60–85, 1969.

[76] I. Rabin and O. Hahn, "Characterization of the Dead Sea Scrolls by advanced analytical techniques," *Analytical Methods*, vol. 5, no. 18, pp. 4648–4654, 2013.

[77] I. Rabin, "Building a bridge from the Dead Sea Scrolls," in *Jewish Manuscript Cultures: New Perspectives*, vol. 13, Walter de Gruyter GmbH & Co KG, 2017.

[78] Y. Yadin, "The Temple Scroll," *The Biblical Archaeologist*, vol. 30, no. 4, pp. 135–139, 1967.

[79] I. Rabin, "Material Analysis of the Dead Sea Scrolls Fragments," in *Gleanings from the Caves. Dead Sea Scrolls and Artefacts of The Schøyen Collection* (T. Elgyin, K. Davis, and M. Langlois, eds.), pp. 327–338, Bloomsbury T&T Clark, 2016.

[80] H. J. Plenderleith, "Technical note on unwrapping of Dead Sea Scroll fragments," in *Discoveries in the Judean Desert I, Qumran Cave I*, pp. 39–40, 1955.

[81] S. Weiner, Z. Kustanovich, E. Gil-Av, and W. Traub, "Dead Sea Scroll parchments: unfolding of the collagen molecules and racemization of aspartic acid," *Nature*, vol. 287, no. 5785, pp. 820–823, 1980.

[82] M. Derrick, "Evaluation of the state of degradation of Dead Sea Scroll samples using FT-IR spectroscopy," *The Book and Paper Annual*, vol. 10, pp. 49–65, 1991.

[83] R. Schütz, L. Bertinetti, I. Rabin, P. Fratzl, and A. Masic, "Quantifying degradation of collagen in ancient manuscripts: The case of the Dead Sea Temple Scroll," *Analyst*, vol. 138, no. 19, pp. 5594–5599, 2013.

[84] M. Bicchieri, A. Sodo, I. Rabin, A. Kohl, and G. Piantanida, "New results in Dead Sea Scrolls non-destructive characterisation. Evidence of different parchment manufacture in the fragments from Reed collection," *Journal of Cultural Heritage*, vol. 32, pp. 22–29, 2018.

[85] A. J. B. Poole and R. Reed, "The preparation of leather and parchment by the Dead Sea Scrolls community," *Technology and Culture*, vol. 3, no. 1, pp. 1–26, 1962.

[86] R. A. Nyquist and R. O. Kagel, *Handbook of infrared and Raman spectra of inorganic compounds and organic salts: Infrared spectra of inorganic compounds*. Academic Press, 2012.

[87] "Glauberite." https://rruff.info/doclib/hom/glauberite.pdf. Accessed: 2019-01-21.

[88] T. Wolff, I. Rabin, I. Mantouvalou, B. Kanngießer, W. Malzer, E. Kindzorra, and O. Hahn, "Provenance studies on Dead Sea scrolls parchment by means of quantitative micro-XRF," *Analytical and Bioanalytical Chemistry*, vol. 402, pp. 1493–1503, Feb. 2012.

[89] S. Boggs Jr., *Principles of Sedimentology and Stratigraphy*. Pearson Education, 2014.

[90] R. A. Garber, Y. Levy, and G. M. Friedman, "The sedimentology of the Dead Sea," *Carbonates and Evaporites*, vol. 2, no. 1, p. 43, 1987.

[91] S. Boghosian, "Structural damage of parchment at the molecular level assessed by Raman spectroscopy," *Improved Assessment of Parchment*, pp. 105–109, 2007.

[92] R. Larsen, D. V. Poulsen, F. Juchauld, H. Jerosch, M. Odlyha, J. de Groot, T. Wess, J. Hiller, G. Della Gatta, E. Badea, *et al.*, "Damage assessment of parchment: complexity and relations at different structural levels," *14th ICOM-CC Preprints*, vol. 1, pp. 199–208, 2005.

[93] C. J. Kennedy and T. J. Wess, "The structure of collagen within parchment - a review," *Restaurator*, vol. 24, no. 2, pp. 61–80, 2003.

[94] M. Beran, "Application of statistical theories for the determination of thermal, electrical, and magnetic properties of heterogeneous materials (for composite materials design)," *Mechanics of Composite Materials*, pp. 209–249, 1974.

[95] M. J. Beran, "Statistical continuum theories," *American Journal of Physics*, vol. 36, no. 10, pp. 923–923, 1968.

[96] J. G. Berryman, "Long–wavelength propagation in composite elastic media I. Spherical inclusions," *The Journal of the Acoustical Society of America*, vol. 68, pp. 1809–1819, Dec. 1980.

[97] J. G. Berryman, "Long–wavelength propagation in composite elastic media II. Ellipsoidal inclusions," *The Journal of the Acoustical Society of America*, vol. 68, pp. 1820–1831, Dec. 1980.

[98] J. P. Watt, G. F. Davies, and R. J. O'Connell, "The elastic properties of composite materials," *Reviews of Geophysics*, vol. 14, no. 4, p. 541, 1976.

[99] W. Voigt, "Über die Beziehung zwischen den beiden Elasticitätsconstanten isotroper Körper," *Annalen der Physik*, vol. 274, no. 12, pp. 573–587, 1889.

[100] A. Reuss, "Berechnung der Fließgrenze von Mischkristallen auf Grund der Plastizitätsbedingung für Einkristalle," *ZAMM - Zeitschrift für Angewandte Mathematik und Mechanik*, vol. 9, no. 1, pp. 49–58, 1929.

[101] N. X. Randall, M. Vandamme, and F.-J. Ulm, "Nanoindentation analysis as a two-dimensional tool for mapping the mechanical properties of complex surfaces," *Journal of Materials Research*, vol. 24, pp. 679–690, Mar. 2009.

[102] M. Ostoja-Starzewski, *Microstructural randomness and scaling in mechanics of materials*. CRC Press, 2007.

[103] G. I. Taylor, "Plastic strain in metals," *Journal of the Institute of Metals*, vol. 62, pp. 307–324, 1938.

[104] Sachs, "Zur Ableitung einer Fließbedingung," *Z. Ver. Dtsch. Ing*, vol. 72, pp. 734–736, 1928.

[105] Z. Hashin and S. Shtrikman, "A variational approach to the theory of the elastic behaviour of multiphase materials," *Journal of the Mechanics and Physics of Solids*, vol. 11, pp. 127–140, Mar. 1963.

[106] L. P. Liu, "Hashin–Shtrikman bounds and their attainability for multi-phase composites," *Proceedings of the Royal Society A: Mathematical, Physical and Engineering Sciences*, vol. 466, pp. 3693–3713, Dec. 2010.

[107] R. Hill, "The Elastic Behaviour of a Crystalline Aggregate," *Proceedings of the Physical Society. Section A*, vol. 65, pp. 349–354, May 1952.

[108] R. Hill, "A self-consistent mechanics of composite materials," *Journal of the Mechanics and Physics of Solids*, vol. 13, pp. 213–222, Aug. 1965.

[109] T. Mori and K. Tanaka, "Average stress in matrix and average elastic energy of materials with misfitting inclusions," *Acta Metallurgica*, vol. 21, pp. 571–574, May 1973.

[110] J. D. Eshelby, "The determination of the elastic field of an ellipsoidal inclusion, and related problems," *Proceedings of the royal society of London. Series A. Mathematical and physical sciences*, vol. 241, no. 1226, pp. 376–396, 1957.

[111] R. Ogden, "On the overall moduli of non-linear elastic composite materials," *Journal of the Mechanics and Physics of Solids*, vol. 22, no. 6, pp. 541–553, 1974.

[112] M. Geers, V. Kouznetsova, and W. Brekelmans, "Multi-scale computational homogenization: Trends and challenges," *Journal of Computational and Applied Mathematics*, vol. 234, pp. 2175–2182, Aug. 2010.

[113] G. Kang, X. Shao, and S. Guo, "Effect of interfacial bonding on uniaxial ratchetting of SiCP/6061Al composites: Finite element analysis with 2-D and 3-D unit cells," *Materials Science and Engineering: A*, vol. 487, pp. 431–444, July 2008.

[114] V. M. Rao, P. Mahajan, and R. Mittal, "Effect of interfacial debonding and matrix cracking on mechanical properties of multidirectional composites," *Composite Interfaces*, vol. 15, no. 4, pp. 379–409, 2008.

[115] A. Bolshakov, W. C. Oliver, and G. M. Pharr, "Influences of stress on the measurement of mechanical properties using nanoindentation: Part II. Finite element simulations," *Journal of Materials Research*, vol. 11, pp. 760–768, Mar. 1996.

[116] A. C. Reddy, "Effect of porosity formation during synthesis of cast AA4015/titanium nitride particle-metal matrix composites," in *5th National Conference on Materials and Manufacturing Processes, Hyderabad*, pp. 9–10, 2006.

[117] H. Shen and C. Lissenden, "3D finite element analysis of particle-reinforced aluminum," *Materials Science and Engineering: A*, vol. 338, pp. 271–281, Dec. 2002.

[118] H. E. Pettermann and S. Suresh, "A comprehensive unit cell model: a study of coupled effects in piezoelectric 1–3 composites," *International Journal of Solids and Structures*, p. 18, 2000.

[119] B. V. Sankar and R. V. Marrey, "A unit-cell model of textile composite beams for predicting stiffness properties," *Composites Science and Technology*, vol. 49, pp. 61–69, Jan. 1993.

[120] H.-L. Lee, S.-W. Wang, Y.-C. Yang, and W.-J. Chang, "Effect of porosity on the mechanical properties of a nanoporous graphene membrane using the atomic-scale finite element method," *Acta Mechanica*, vol. 228, pp. 2623–2629, July 2017.

[121] W. Sun, F. Lin, and X. Hu, "Computer-aided design and modeling of composite unit cells," *Composites Science and Technology*, vol. 61, pp. 289–299, Feb. 2001.

[122] P. Spanos and A. Kontsos, "A multiscale Monte Carlo finite element method for determining mechanical properties of polymer nanocomposites," *Probabilistic Engineering Mechanics*, vol. 23, pp. 456–470, Oct. 2008.

[123] R. Sharma, P. Mahajan, and R. K. Mittal, "Image-based finite element analysis of 3D-orthogonal carbon-carbon composite," in *Proceedings of the World Congress on Engineering*, vol. 2, pp. 1597–1601, 2010.

[124] E. Padilla, V. Jakkali, L. Jiang, and N. Chawla, "Quantifying the effect of porosity on the evolution of deformation and damage in Sn-based solder joints by X-ray microtomography and microstructure-based finite element modeling," *Acta Materialia*, vol. 60, pp. 4017–4026, May 2012.

[125] G. L. Vignoles, "Image segmentation for phase-contrast hard X-ray CMT of C/C composites," *Carbon*, vol. 39, no. 2, pp. 167–173, 2001.

[126] J. Ali, J. K. Farooqi, D. Buckthorpe, A. Cheyne, and P. Mummery, "Comparative study of predictive FE methods for mechanical properties of nuclear composites," *Journal of Nuclear Materials*, vol. 383, no. 3, pp. 247–253, 2009.

[127] R. Guldberg, S. Hollister, and G. Charras, "The accuracy of digital image-based finite element models," 1998.

[128] G. T. Charras and R. E. Guldberg, "Improving the local solution accuracy of large-scale digital image-based finite element analyses," *Journal of Biomechanics*, vol. 33, no. 2, pp. 255–259, 2000.

[129] S. J. Hollister and B. A. Riemer, "Digital-image-based finite element analysis for bone microstructure using conjugate gradient and Gaussian filter techniques," in *Mathematical Methods in Medical Imaging II*, vol. 2035, pp. 95–106, International Society for Optics and Photonics, 1993.

[130] P. Magne, "Efficient 3D finite element analysis of dental restorative procedures using micro-CT data," *Dental Materials*, vol. 23, no. 5, pp. 539–548, 2007.

[131] D. E. Anderson and J. R. Cotton, "Mechanical analysis of percutaneous sacroplasty using CT image based finite element models," *Medical Engineering & Physics*, vol. 29, no. 3, pp. 316–325, 2007.

[132] S. A. Langer, E. R. Fuller, and W. C. Carter, "OOF: an image-based finite-element analysis of material microstructures," *Computing in Science & Engineering*, vol. 3, no. 3, pp. 15–23, 2001.

[133] A. C. Reid, S. A. Langer, R. C. Lua, V. R. Coffman, S.-I. Haan, and R. E. García, "Image-based finite element mesh construction for material microstructures," *Computational Materials Science*, vol. 43, no. 4, pp. 989–999, 2008.

[134] O. Coindreau, G. Vignoles, and P. Cloetens, "Direct 3D microscale imaging of carbon–carbon composites with computed holotomography," *Nuclear Instruments and Methods in Physics Research Section B: Beam Interactions with Materials and Atoms*, vol. 200, pp. 308–314, 2003.

[135] J. Martin-Herrero and C. Germain, "Microstructure reconstruction of fibrous C/C composites from X-ray microtomography," *Carbon*, vol. 45, no. 6, pp. 1242–1253, 2007.

[136] N. More, B. Basse-Cathalinat, C. Baquey, F. Lacroix, and D. Ducassou, "Application of novel techniques of medical imaging to the non-destructive analysis of carbon-carbon composite materials," *Nuclear Instruments and Methods in Physics Research*, vol. 214, no. 2-3, pp. 531–536, 1983.

[137] G. Spanos, D. Rowenhorst, A. Lewis, and A. Geltmacher, "Combining serial sectioning, EBSD analysis, and image-based finite element modeling," *MRS Bulletin*, vol. 33, no. 6, pp. 597–602, 2008.

[138] O. Bernard, F.-J. Ulm, and E. Lemarchand, "A multiscale micromechanics-hydration model for the early-age elastic properties of cement-based materials," *Cement and Concrete Research*, vol. 33, no. 9, pp. 1293–1309, 2003.

[139] G. Constantinides and F. J. Ulm, "The effect of two types of C-S-H on the elasticity of cement-based materials: Results from nanoindentation and micromechanical modeling," *Cement and Concrete Research*, vol. 34, no. 1, pp. 67–80, 2004. ISBN: 0008-8846.

[140] P. Acker, "Micromechanical analysis of creep and shrinkage mechanisms," *Creep, Shrinkage and Durability Mechanics of Concrete and other quasi-brittle Materials, Cambridge, MA*, pp. 15–25, 2001.

[141] P. D. Tennis and H. M. Jennings, "A model for two types of calcium silicate hydrate in the microstructure of portland cement pastes," *Cement and Concrete Research*, vol. 30, no. 6, pp. 855–863, 2000.

[142] V. Šmilauer and Z. Bittnar, "Microstructure-based micromechanical prediction of elastic properties in hydrating cement paste," *Cement and Concrete Research*, vol. 36, no. 9, pp. 1708–1718, 2006.

[143] S. D. Palkovic, K. Kupwade-Patil, S. Yip, and O. Büyüköztürk, "Random field finite element models with cohesive-frictional interactions of a hardened cement paste microstructure," *Journal of the Mechanics and Physics of Solids*, vol. 119, pp. 349–368, 2018.

[144] W. Oliver and G. Pharr, "An improved technique for determining hardness and elastic modulus using load and displacement sensing indentation experiments," *Journal of Materials Research*, vol. 7, pp. 1564–1583, June 1992.

[145] W. Oliver and G. Pharr, "Measurement of hardness and elastic modulus by instrumented indentation: Advances in understanding and refinements to methodology," *Journal of Materials Research*, vol. 19, no. 01, pp. 3–20, 2004. ISBN: 0884-2914.

[146] M. Vandamme and F.-J. Ulm, "Nanoindentation investigation of creep properties of calcium silicate hydrates," *Cement and Concrete Research*, vol. 52, pp. 38–52, Oct. 2013.

[147] "ISO 14577-1:2015 Metallic materials–instrumented indentation test for hardness and materials parameters - Part 1: Test method," Jul 2020.

[148] X. Chen and J. J. Vlassak, "Numerical study on the measurement of thin film mechanical properties by means of nanoindentation," *Journal of Materials Research*, vol. 16, pp. 2974–2982, Oct. 2001.

[149] D. Stollberg, J. Hampikian, L. Riester, and W. Carter, "Nanoindentation measurements of combustion CVD Al2O3 and YSZ films," *Materials Science and Engineering: A*, vol. 359, pp. 112–118, Oct. 2003.

[150] P. Delobelle, E. Fribourg-Blanc, and D. Remiens, "Mechanical properties determined by nanoindentation tests of [Pb(Zr,Ti)O_3] and

[$Pb(Mg_{1/3}Nb_{2/3})_{1-x}Ti_xO_3$] sputtered thin films," *Thin Solid Films*, vol. 515, no. 4, pp. 1385–1393, 2006.

[151] A. A. Volinsky, J. B. Vella, and W. W. Gerberich, "Fracture toughness, adhesion and mechanical properties of low-K dielectric thin films measured by nanoindentation," *Thin Solid Films*, vol. 429, pp. 201–210, Apr. 2003.

[152] R. Navamathavan, K.-K. Kim, D.-K. Hwang, S.-J. Park, J.-H. Hahn, T. G. Lee, and G.-S. Kim, "A nanoindentation study of the mechanical properties of ZnO thin films on (0 0 0 1) sapphire," *Applied Surface Science*, vol. 253, pp. 464–467, Nov. 2006.

[153] G. Constantinides, F.-J. Ulm, and K. Van Vliet, "On the use of nanoindentation for cementitious materials," *Materials and Structures*, vol. 36, no. 3, pp. 191–196, 2003.

[154] W. Zhu, J. J. Hughes, N. Bicanic, and C. J. Pearce, "Nanoindentation mapping of mechanical properties of cement paste and natural rocks," *Materials Characterization*, vol. 58, pp. 1189–1198, Nov. 2007.

[155] J. J. Hughes and P. Trtik, "Micro-mechanical properties of cement paste measured by depth-sensing nanoindentation: a preliminary correlation of physical properties with phase type," *Materials Characterization*, vol. 53, pp. 223–231, Nov. 2004.

[156] J. J. Chen, L. Sorelli, M. Vandamme, F.-J. Ulm, and G. Chanvillard, "A coupled nanoindentation/SEM-EDS study on low water/cement ratio Portland cement paste: evidence for C–S–H/$Ca(OH)_2$ nanocomposites," *Journal of the American Ceramic Society*, vol. 93, no. 5, pp. 1484–1493, 2010.

[157] V. Nežerka, J. Němeček, Z. Slížková, and P. Tesárek, "Investigation of crushed brick-matrix interface in lime-based ancient mortar by microscopy and nanoindentation," *Cement and Concrete Composites*, vol. 55, pp. 122–128, Jan. 2015.

[158] W. Zhu and P. Bartos, "Assessment of interfacial microstructure and bond properties in aged GRC using a novel microindentation method," *Cement and Concrete Research*, vol. 27, pp. 1701–1711, Nov. 1997.

[159] W. Zhu and P. J. Bartos, "Application of depth-sensing microindentation testing to study of interfacial transition zone in reinforced concrete," *Cement and Concrete Research*, vol. 30, pp. 1299–1304, Aug. 2000.

[160] K. Velez, S. Maximilien, D. Damidot, G. Fantozzi, and F. Sorrentino, "Determination by nanoindentation of elastic modulus and hardness of pure constituents of Portland cement clinker," *Cement and Concrete Research*, vol. 31, pp. 555–561, Apr. 2001.

[161] E. J. Garboczi, "Finite element and finite difference programs for computing the linear electric and elastic properties of digital images of random materials," tech. rep., 1998.

[162] C.-J. Haecker, E. Garboczi, J. Bullard, R. Bohn, Z. Sun, S. Shah, and T. Voigt, "Modeling the linear elastic properties of portland cement paste," *Cement and Concrete Research*, vol. 35, no. 10, pp. 1948–1960, 2005.

[163] S. Kamali, M. Moranville, E. Garboczi, S. Prené, and B. Gérard, "Hydrate dissolution influence on the Young's modulus of cement pastes," *Proceedings of Fracture Mechanics of Concrete Structures (FraMCoS-V), Routledge, Vail*, pp. 631–638, 2004.

[164] P. Kumar and N. Bhandari, "Non-linear finite element analysis of masonry arches for prediction of collapse load," *Structural Engineering International*, vol. 15, no. 3, pp. 166–175, 2005.

[165] H. Kim and W. G. Buttlar, "Finite element cohesive fracture modeling of airport pavements at low temperatures," *Cold Regions Science and Technology*, vol. 57, no. 2-3, pp. 123–130, 2009.

[166] G. Thiagarajan, A. V. Kadambi, S. Robert, and C. F. Johnson, "Experimental and finite element analysis of doubly reinforced concrete slabs subjected to blast loads," *International Journal of Impact Engineering*, vol. 75, pp. 162–173, 2015.

[167] F. J. Vecchio, M. P. Collins, and J. Aspiotis, "High-strength concrete elements subjected to shear," *ACI Structural Journal-American Concrete Institute*, vol. 91, no. 4, pp. 423–433, 1994.

[168] A. Gotlif, J. Mallela, and L. Khazanovich, "Finite element study of partial-depth cracks in restrained PCC slabs," *International Journal of Pavement Engineering*, vol. 7, no. 4, pp. 323–329, 2006.

[169] W. Goh, N. Mohamad, R. Abdullah, and A. Samad, "Compression test and finite element analysis of foamed concrete cube," *Journal of Engineering and Technology*, vol. 5, no. 1, pp. 1–9, 2014.

[170] M. Hain and P. Wriggers, "Numerical homogenization of hardened cement paste," *Computational Mechanics*, vol. 42, no. 2, pp. 197–212, 2008.

[171] *Properties: Silica - Fused Silica (Silicon Dioxide)*, 2020.

[172] *Material: Quartz Crystalline (SiO2) - Korth Kristalle GmbH*, 2020.

[173] Y. Agustian and S. Goto, "Strength and deformation characteristics of scoria in triaxial compression at low confining stress," *Soils and foundations*, vol. 48, no. 1, pp. 27–39, 2008.

[174] W. Liu, L. Zhang, and N. Luo, "Elastic modulus evolution of rocks under heating–cooling cycles," *Scientific Reports*, vol. 10, no. 1, pp. 1–9, 2020.

[175] D. Chicot, J. Mendoza, A. Zaoui, G. Louis, V. Lepingle, F. Roudet, and J. Lesage, "Mechanical properties of magnetite (Fe3O4), hematite (α-Fe2O3) and goethite (α-feo· OH) by instrumented indentation and molecular dynamics analysis," *Materials Chemistry and Physics*, vol. 129, no. 3, pp. 862–870, 2011.

[176] T. Noguchi, F. Tomosawa, K. M. Nemati, B. M. Chiaia, and A. P. Fantilli, "A practical equation for elastic modulus of concrete," *ACI Structural Journal*, vol. 106, no. 5, p. 690, 2009.

[177] C. Kuhn and R. Müller, "A continuum phase field model for fracture," *Engineering Fracture Mechanics*, vol. 77, no. 18, pp. 3625–3634, 2010.

[178] J. Chessa, P. Smolinski, and T. Belytschko, "The extended finite element method (XFEM) for solidification problems," *International Journal for Numerical Methods in Engineering*, vol. 53, no. 8, pp. 1959–1977, 2002.

[179] G. Lilliu and J. G. van Mier, "3D lattice type fracture model for concrete," *Engineering Fracture Mechanics*, vol. 70, no. 7-8, pp. 927–941, 2003.

[180] H. Laubie, F. Radjai, R. Pellenq, and F.-J. Ulm, "A potential-of-mean-force approach for fracture mechanics of heterogeneous materials using the lattice element method," *Journal of the Mechanics and Physics of Solids*, vol. 105, pp. 116–130, 2017.

[181] "Pompeii." http://www.history.com/topics/ancient-history/pompeii, 2010. Accessed: 2017-07-05.

[182] A. Butterworth and R. Laurence, *Pompeii: The Living City*. New York: St. Martin's Press, 2005.

[183] P. Popham, "Ashes to ashes: the latter-day ruin of Pompeii," *Prospect Magazine*, May 2010.

[184] "Damaged Pompeii to receive Italy rescue fund - BBC News." https://www.bbc.com/news/world-europe-26443808, 2014. Accessed: 2018-11-04.

[185] J. Heyman, *The Stone Skeleton: Structural Engineering of Masonry Architecture*. Cambridge University Press, 1 ed., 1995.

[186] S. Huerta, "Mechanics of masonry vaults: the equilibrium approach," *3rd International Seminar in Historical Constructions, Guimarães, Portugal*, no. February, pp. 47–70, 2001.

[187] P. Clemente, Antonio Occhiuzzi, and A. Raithel, "Limit behavior of stone arch bridges," *Journal of Structural Engineering*, vol. 121, no. 7, pp. 1045–1050, 1995.

[188] S. H. Cocking, S. Price, and M. J. DeJong, "The effects of wind on the loading and vibration of stone pinnacles," *Masonry International*, vol. 29, no. 2, pp. 53–60, 2017.

[189] J. Heyman, "The safety of masonry arches," *International Journal of Mechanical Sciences*, vol. 11, no. November 1968, pp. 363–385, 1969.

[190] M. J. DeJong, "Seismic response of stone masonry spires: Analytical modeling," *Engineering Structures*, vol. 40, pp. 556–565, July 2012.

[191] M. J. DeJong and C. Vibert, "Seismic response of stone masonry spires: Computational and experimental modeling," *Engineering Structures*, vol. 40, pp. 566–574, July 2012.

[192] G. W. Housner, "The behavior of inverted pendulum structures during earthquakes," *Bulletin of the Seismological Society of America*, vol. 53, no. 2, pp. 403–417, 1963. arXiv: 1011.1669v3 ISBN: 0037-1106.

[193] M. Aslam, D. Scalise, and W. G. Godden, "Earthquake rocking response of rigid bodies," *Journal of the Structural Division*, vol. 106, no. 2, pp. 377–392, 1980.

[194] A. Pompei, A. Scalia, and M. A. Sumbatyan, "Dynamics of rigid block due to horizontal ground motion," *Journal of Engineering Mechanics*, vol. 124, pp. 713–717, July 1998.

[195] S. J. Hogan, "The many steady state responses of a rigid block under harmonic forcing," *Earthquake Engineering & Structural Dynamics*, vol. 19, pp. 1057–1071, Oct. 1990.

[196] P. D. Spanos and A. Koh, "Rocking of rigid blocks due to harmonic shaking," *Journal of Engineering Mechanics*, vol. 110, pp. 1627–1642, Nov. 1984.

[197] W. K. Tso and C. M. Wong, "Steady state rocking response of rigid blocks part 1: Analysis," *Earthquake Engineering & Structural Dynamics*, vol. 18, pp. 89–106, Jan. 1989.

[198] R. Giannini and R. Masiani, "Random Vibration of the Rigid Block," in *Computational Stochastic Mechanics* (P. D. Spanos and C. A. Brebbia, eds.), pp. 741–752, Dordrecht: Springer Netherlands, 1991.

[199] R. H. Allen, I. J. Oppenheim, A. R. Parker, and J. Bielak, "On the dynamic response of rigid body assemblies," *Earthquake Engineering & Structural Dynamics*, vol. 14, no. 6, pp. 861–876, 1986.

[200] I. J. Oppenheim, "The masonry arch as a four-link mechanism under base motion," *Earthquake Engineering & Structural Dynamics*, vol. 21, no. 11, pp. 1005–1017, 1992.

[201] I. N. Psycharis, "Dynamic behaviour of rocking two-block assemblies," *Earthquake Engineering & Structural Dynamics*, vol. 19, pp. 555–575, May 1990.

[202] P. D. Spanos, P. C. Roussis, and N. P. Politis, "Dynamic analysis of stacked rigid blocks," *Soil Dynamics and Earthquake Engineering*, vol. 21, pp. 559–578, Oct. 2001.

[203] P. Clemente, "Introduction to dynamics of stone arches," *Earthquake Engineering and Structural Dynamics*, vol. 27, no. 5, pp. 513–522, 1998.

[204] J. Azevedo, G. Sincraian, and J. Lemos, "Seismic behavior of blocky masonry structures," *Earthquake Spectra*, vol. 16, no. 2, pp. 337–365, 2000.

[205] L. De Lorenzis, M. DeJong, and J. Ochsendorf, "Failure of masonry arches under impulse base motion," *Earthquake Engineering & Structural Dynamics*, vol. 36, no. 14, pp. 2119–2136, 2007.

[206] M. J. Dejong, *Seismic Assessment Strategies for Masonry Structures*. PhD thesis, Massachusetts Institute of Technology, 2009. Issue: 2001.

[207] R. Dimitri, L. De Lorenzis, and G. Zavarise, "Numerical study on the dynamic behavior of masonry columns and arches on buttresses with the discrete element method," *Engineering Structures*, vol. 33, no. 12, pp. 3172–3188, 2011. Publisher: Elsevier Ltd.

[208] L. Papaloizou and P. Komodromos, "Planar investigation of the seismic response of ancient columns and colonnades with epistyles using a custom-made software," *Soil Dynamics and Earthquake Engineering*, vol. 29, no. 11-12, pp. 1437–1454, 2009. Publisher: Elsevier.

[209] C. Papantonopoulos, I. N. Psycharis, D. Y. Papastamatiou, J. V. Lemos, and H. P. Mouzakis, "Numerical prediction of the earthquake response of classical columns using the distinct element method," *Earthquake Engineering and Structural Dynamics*, vol. 31, no. 9, pp. 1699–1717, 2002.

[210] I. N. Psycharis, J. V. Lemos, D. Y. Papastamatiou, C. Zambas, and C. Papantonopoulos, "Numerical study of the seismic behaviour of a part of the Parthenon Pronaos," *Earthquake Engineering & Structural Dynamics*, vol. 32, pp. 2063–2084, Nov. 2003.

[211] L. Scandolo and S. Podestà, "Numerical seismic response analysis of multidrum ancient columns," in *SAHC2014—9th International Conference on Structural Analysis of Historical Constructions*, (Mexico City, Mexico), p. 12, Oct. 2014.

[212] E. Boschi, A. Rovelli, R. Funicello, V. Mihailov, L. Krstevska, L. Taskov, and M. Garevski, "In situ experimental testing of two historical columns in Rome," in *European Seismic Design and Practice*, (Chester), 1995.

[213] L. Krstevska, V. Mihailov, E. Boschi, and A. Rovelli, "Experimental dynamic testing of prototype and model of the Antonina column in Roma," in *Proceedings of the Eleventh World Conference on Earthquake Engineering, Paper No. 546*, Elsevier, 1996.

[214] A. Rovelli, "Shaking table test of 1/6 scale model of the Column of Marcus Aurelius in Rome," in *European Seismic Design and Practice*, 1995.

[215] N. Makris and Y. S. Roussos, "Rocking response of rigid blocks under near-source ground motions," *Géotechnique*, vol. 50, pp. 243–262, June 2000.

[216] J. A. Ochsendorf, *Collapse of Masonry Structures*. PhD thesis, University of Cambridge, 2002. Issue: June.

[217] J. W. Plunkett, *The Roman Pantheon: Scale-Model Collapse Analyses*. PhD thesis, Massachusetts Institute of Technology, 2016.

[218] J. A. Ochsendorf, J. I. Hernando, and S. Huerta, "Collapse of masonry buttresses," *Journal of Architectural Engineering*, vol. 10, no. 3, pp. 88–97, 2004.

[219] J. F. Zessin, *Collapse Analysis of Unreinforced Masonry Domes and Curving Walls*. PhD thesis, Massachusetts Institute of Technology, 2012.

[220] A. Quinonez, J. Zessin, A. Nutzel, and J. Ochsendorf, "Small-scale models for testing masonry structures," vol. 133, pp. 497–502, 2010.

[221] D. Sulsky, Z. Chen, and H. L. Schreyer, "A particle method for history-dependent materials," *Computer Methods in Applied Mechanics and Engineering*, vol. 118, no. 1-2, pp. 179–196, 1994.

[222] A. Stomakhin, C. Schroeder, L. Chai, J. Teran, and A. Selle, "A material point method for snow simulation," *ACM Transactions on Graphics (TOG)*, vol. 32, no. 4, pp. 1–10, 2013.

[223] S. Raymond, Y. Aimene, J. Nairn, A. Ouenes, *et al.*, "Coupled fluid-solid geomechanical modeling of multiple hydraulic fractures interacting with natural fractures and the resulting proppant distribution," in *SPE/CSUR Unconventional Resources Conference*, Society of Petroleum Engineers, 2015.

[224] P. Huang, S.-l. Li, H. Guo, and Z.-m. Hao, "Large deformation failure analysis of the soil slope based on the material point method," *Computational Geosciences*, vol. 19, pp. 951–963, Aug. 2015.

[225] S. Wieghold, Z. Liu, S. J. Raymond, L. T. Meyer, J. R. Williams, T. Buonassisi, and E. M. Sachs, "Detection of sub-500-µm cracks in multicrystalline silicon wafer using edge-illuminated dark-field imaging to enable thin solar cell manufacturing," *Solar Energy Materials and Solar Cells*, vol. 196, pp. 70–77, 2019.

[226] S. J. Raymond, B. D. Jones, and J. R. Williams, "Modeling damage and plasticity in aggregates with the material point method (MPM)," *Computational Particle Mechanics*, Dec. 2018.

[227] W. J. M. Rankine, *A manual of applied mechanics*. Charles Griffin and Company, 1872.

[228] J. J. Monaghan, "Smoothed Particle Hydrodynamics," *Annual Review of Astronomy and Astrophysics*, vol. 30, no. 1, pp. 543–574, 1992.

[229] P. A. Cundall and O. D. L. Strack, "A discrete numerical model for granular assemblies," *Géotechnique*, vol. 29, pp. 47–65, Mar. 1979.

[230] D. Giardini, J. Woessner, L. Danciu, H. Crowley, F. Cotton, G. Grünthal, R. Pinho, and G. Valensise, "SHARE European seismic hazard map for peak ground acceleration, 10% exceedance probabilities in 50 years," *SHARE European seismic harmonization project*, 2013.

[213] L. Krstevska, V. Mihailov, E. Boschi, and A. Rovelli, "Experimental dynamic testing of prototype and model of the Antonina column in Roma," in *Proceedings of the Eleventh World Conference on Earthquake Engineering, Paper No. 546*, Elsevier, 1996.

[214] A. Rovelli, "Shaking table test of 1/6 scale model of the Column of Marcus Aurelius in Rome," in *European Seismic Design and Practice*, 1995.

[215] N. Makris and Y. S. Roussos, "Rocking response of rigid blocks under near-source ground motions," *Géotechnique*, vol. 50, pp. 243–262, June 2000.

[216] J. A. Ochsendorf, *Collapse of Masonry Structures*. PhD thesis, University of Cambridge, 2002. Issue: June.

[217] J. W. Plunkett, *The Roman Pantheon: Scale-Model Collapse Analyses*. PhD thesis, Massachusetts Institute of Technology, 2016.

[218] J. A. Ochsendorf, J. I. Hernando, and S. Huerta, "Collapse of masonry buttresses," *Journal of Architectural Engineering*, vol. 10, no. 3, pp. 88–97, 2004.

[219] J. F. Zessin, *Collapse Analysis of Unreinforced Masonry Domes and Curving Walls*. PhD thesis, Massachusetts Institute of Technology, 2012.

[220] A. Quinonez, J. Zessin, A. Nutzel, and J. Ochsendorf, "Small-scale models for testing masonry structures," vol. 133, pp. 497–502, 2010.

[221] D. Sulsky, Z. Chen, and H. L. Schreyer, "A particle method for history-dependent materials," *Computer Methods in Applied Mechanics and Engineering*, vol. 118, no. 1-2, pp. 179–196, 1994.

[222] A. Stomakhin, C. Schroeder, L. Chai, J. Teran, and A. Selle, "A material point method for snow simulation," *ACM Transactions on Graphics (TOG)*, vol. 32, no. 4, pp. 1–10, 2013.

[223] S. Raymond, Y. Aimene, J. Nairn, A. Ouenes, *et al.*, "Coupled fluid-solid geomechanical modeling of multiple hydraulic fractures interacting with natural fractures and the resulting proppant distribution," in *SPE/CSUR Unconventional Resources Conference*, Society of Petroleum Engineers, 2015.

[224] P. Huang, S.-l. Li, H. Guo, and Z.-m. Hao, "Large deformation failure analysis of the soil slope based on the material point method," *Computational Geosciences*, vol. 19, pp. 951–963, Aug. 2015.

[225] S. Wieghold, Z. Liu, S. J. Raymond, L. T. Meyer, J. R. Williams, T. Buonassisi, and E. M. Sachs, "Detection of sub-500-µm cracks in multicrystalline silicon wafer using edge-illuminated dark-field imaging to enable thin solar cell manufacturing," *Solar Energy Materials and Solar Cells*, vol. 196, pp. 70–77, 2019.

[226] S. J. Raymond, B. D. Jones, and J. R. Williams, "Modeling damage and plasticity in aggregates with the material point method (MPM)," *Computational Particle Mechanics*, Dec. 2018.

[227] W. J. M. Rankine, *A manual of applied mechanics*. Charles Griffin and Company, 1872.

[228] J. J. Monaghan, "Smoothed Particle Hydrodynamics," *Annual Review of Astronomy and Astrophysics*, vol. 30, no. 1, pp. 543–574, 1992.

[229] P. A. Cundall and O. D. L. Strack, "A discrete numerical model for granular assemblies," *Géotechnique*, vol. 29, pp. 47–65, Mar. 1979.

[230] D. Giardini, J. Woessner, L. Danciu, H. Crowley, F. Cotton, G. Grünthal, R. Pinho, and G. Valensise, "SHARE European seismic hazard map for peak ground acceleration, 10% exceedance probabilities in 50 years," *SHARE European seismic harmonization project*, 2013.